SAND2008-3860P

Jason W. Shelton
Candidate

Electrical and Computer Engineering
Department

This thesis is approved, and it is acceptable in quality and form for publication on microfilm:

Approved by the Thesis Committee:

_____, Chairperson

_____

_____

_____

_____

_____

_____

Accepted:

_____
Dean, Graduate School

_____
Date

The Effects of Non-Uniform Illumination on the Performance of Series Connected Photovoltaic Arrays

By

Jason W. Shelton

Bachelor of Science, Electronics Engineering Technology
DeVry University, 2002

THESIS

Submitted in Partial Fulfillment of the
Requirements for the Degree of

Master of Science
Electrical Engineering

The University of New Mexico
Albuquerque, New Mexico

May, 2008

DEDICATION

To my wife and children who are the inspiration for everything I do.

ACKNOWLEDGEMENTS

I would like to gratefully acknowledge the endless encouragement and support of my advisors Dr. Fred Dickey of Sandia National Laboratories and Dr. Sanjay Krishna of the Center for High Technology Materials, UNM. Without them none of this would have been possible.

I would also like to thank Joe Thomes, David Stein, Bob Nasby, and Oliver Jeromin for their help during various parts of this thesis.

This work was done in support of ongoing programs at Sandia National Laboratories.

Sandia is a multiprogram laboratory operated by Sandia Corporation, a Lockheed Martin Company, for the United States Department of Energy's National Nuclear Security Administration under Contract DE-AC04-94AL85000.

The Effects of Non-Uniform Illumination on the Performance of Series Connected Photovoltaic Arrays

By

Jason W. Shelton

ABSTRACT OF THESIS

Submitted in Partial Fulfillment of the
Requirements for the Degree of

Master of Science
Electrical Engineering

The University of New Mexico
Albuquerque, New Mexico

June, 2008

The Effects of Non-Uniform Illumination on the Performance of Series Connected Photovoltaic Arrays

By

Jason W. Shelton

Bachelor of Science, Electronics Engineering Technology,
DeVry University, 2002

Master of Science, Electrical Engineering, University of New Mexico, 2008

Abstract

Optical power transfer has several advantages that make this technology useful in many applications. Optical power transfer is immune to the noise generating effects of RF and EMI. Transferring power optically also has the benefit of generating electricity in regions where electrical isolation is required. Using series connected photovoltaic arrays (SCPA) for voltage conversion has the advantage in that high voltage can be directly generated in a small volume. These advantages have led to applications in which the optical power is transferred over a fiber optic and converted to electrical power by using an SCPA. Fiber optic illumination is non-uniform and the current generated by an SCPA is limited by the cell with the least amount of illumination. This thesis addresses the effects of single and multi-mode illumination on the performance of SCPAs. PSpice models are developed and system design criteria in which to achieve optimum SCPA performance are given.

Table of Contents

1 Introduction: Objective of Proposed Work

The objective of this work is two-fold. First, a PSpice model that accurately describes the performance of an SCPA (Series Connected Photovoltaic Array) is developed. This model is based on curve-fitting to the data and determining the value of the variables in the device characteristic equation. Second, theory is developed which describes the effects of using Gaussian and multi-mode illumination on the illumination efficiency of an SCPA. In the case of Gaussian illumination, the theory developed will allow an engineer to determine the effects of the beam radius on the illumination efficiency. In the case of multi-mode illumination, theory is developed that shows the illumination efficiency of an SCPA is a function of the ratio of the photocell area to the mean speckle correlation area where the mean speckle correlation area is determined by the fiber core diameter, SCPA distance from the fiber, and wavelength.

The results of this thesis were presented at the SPIE Optics and Photonics conference: Arming, Safing, Fuzing and Firing in San Diego, Ca. and published in the conference proceedings [1] - [2].

1.1 Background and Motivation

Optical power transfer has several advantages that make this technology useful in many applications. Optical power transfer is immune to the noise generating effects of RF (Radio Frequency) and EMI (Electromagnetic Interference). Transferring power optically also has the benefit of generating electricity in regions where electrical isolation is required. Using SCPAs for voltage conversion has the advantage in that high voltage

can be generated in a small volume. Direct high voltage generation in a small volume is accomplished by eliminating the need for a DC-DC converter that consists of several components which includes a bulky transformer. The benefits mentioned above have led to applications including safe and isolated power generation in a small volume for Sandia applications [2], powering MEMS devices [3], remote sensing, aerospace, communications, and electric power [4].

1.2 History

B. H. Rose of Sandia National Laboratories proposed the use of optical power transfer systems using SCPAs in 1992 [5]. The report discussed 3 mm diameter GaAs devices consisting of 2, 6, and 12 series connected cells connected in a pie shaped configuration that produced approximately 2, 7, and 13 volts respectively. JDS Uniphase now produces similar devices that are available commercially. These devices are available pre-mounted in various receptacles that are compatible with popular fiber optic cables and connectors [4]. Figure 1 depicts these devices both with and without the receptacle.

Figures 1a (left) and 1b (right). The figure on the left is a picture of a JDSU SCPA mounted in a ST and FC receptacle [www.jdsu.com]. The figure on the right shows the JDSU SCPA mounted on a T0 header.

In 2002 Jun Ohsawa, at the Toyota Technological Institute reported the manufacture of a 120 cell GaAs SCPA arranged in a rectangular geometry [6]. The overall device dimensions were 2.5 mm x 1.6 mm and the individual cells were 150 μm x 160 μm each (Fig. 2). This SCPA was reported to have the capability of generating over 100 V.

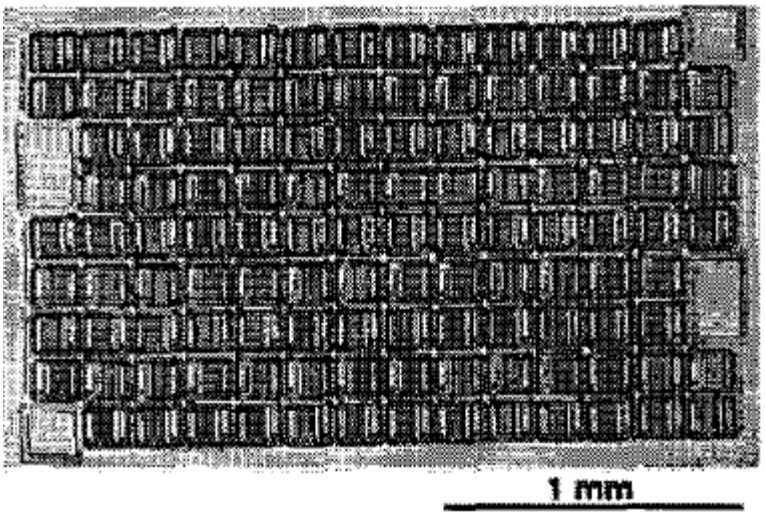

Figure 2. Photo of the rectangular 100 V 120 cell SCPA manufactured by the Toyota Technological Institute [6].

Recent progress in increasing the output voltage of SCPAs has been made at Sandia National Laboratories' Microelectronics Development Laboratory (MDL). In 2005 Rupal K. Patel, [2] reported the successful manufacture of an SCPA that generated over 1 kV. Since then MDL has manufactured SCPAs that consist of 3680 individual cells that are 100 μm x 40 μm in size to form a circular array 4.4 mm in diameter and produce over 2200V [7]. Figure 3a shows the I-V curve for a 2200 V SCPA illuminated using a fiber optic microscope light. Although, the devices are capable of generating 2200 V, there are some reliability issues that are in the process of being solved. Currently 1700 V SCPAs have been reliably produced and are in use as part of a research effort at Sandia. Figure 3b is a picture of various SCPAs that are manufactured at Sandia's MDL. In this masters

thesis project the effects of non-uniform illumination on the performance of an SCPA are investigated.

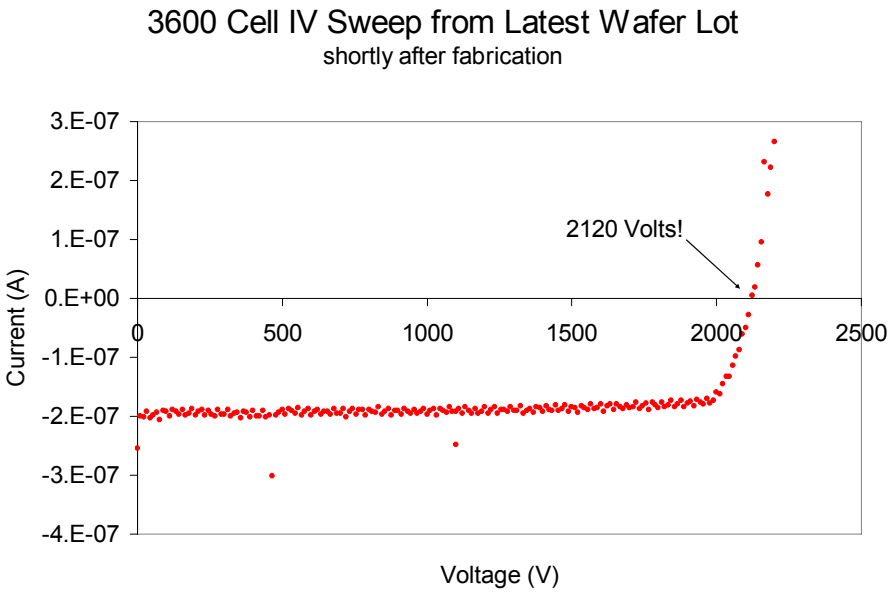

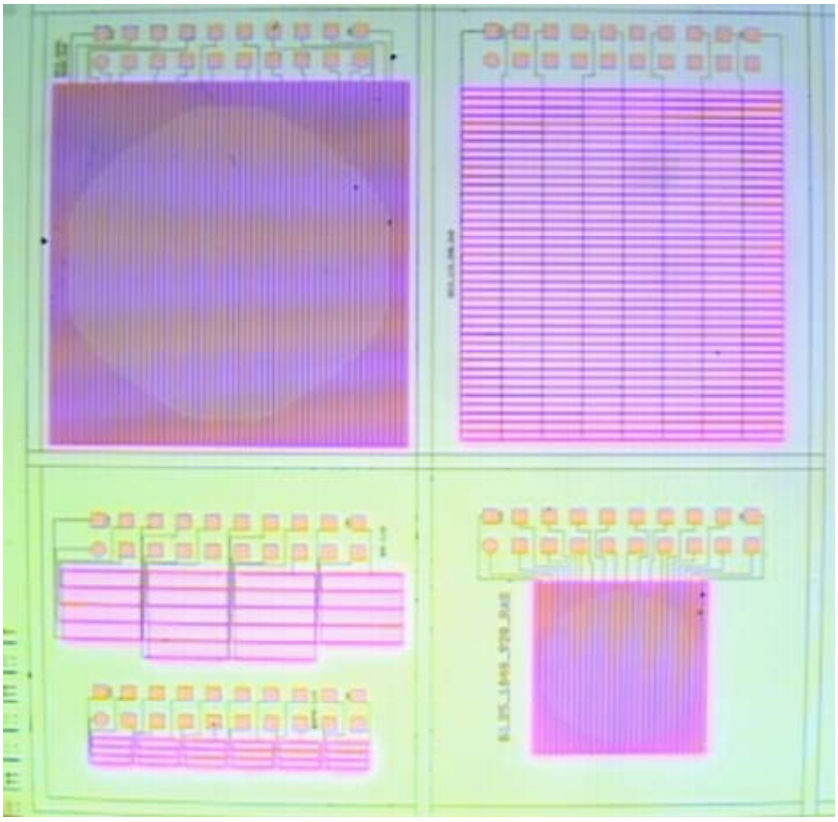

Figures 3a (top) and 3b (bottom). The figure on the top is data showing the direct generation of over 2 kV using a 4.4 mm diameter SCPA. The bottom figure depicts some of the different SCPAs manufactured by Sandia's MDL.

1.3 Problem Statement

SCPAs are sensitive to non-uniform illumination. Research has been done regarding the effects of partial shadowing on uniformly illuminated arrays [8]. The conclusion is that the cell with the least amount of illumination limits the output current of an SCPA thereby making illumination a critical parameter. This is the point where the previous research ends. What is missing in previous research are the effects of direct Gaussian and multi-mode optical fiber illumination.

Fiber illumination is important because some of today's optical power transfer applications do not have line of sight between the optical source and SCPA. In addition to this, the applications usually require an extremely small geometry in which to implement the system. This means that the power must be delivered via optical fiber to a region that has insufficient volume to afford beam-shaping optics with which to uniformly illuminate the SCPA.

The focus of this research is to develop a theory, model, and experimentally investigate SCPA performance under Gaussian and speckled illumination. Aspects researched in this thesis include effects of direct and optical fiber coupled laser illumination.

2 Photovoltaic Device Fundamentals

Photovoltaic cells are essentially diodes that have been optimized for photon absorption and diffusion of the photo-generated carriers. The electric field present within the depletion region provides energy to the photo-generated carriers that is necessary to generate voltage to power a load. Knowledge of photovoltaic device fundamentals is critical in order to develop an equivalent circuit model. This knowledge is vital for understanding device behavior and the limitations that occur when the devices are placed in series. This chapter presents a closed form solutions that describes the behavior of both a single photocell and an SCPA to the first order. The discussion is based off of [5], [8], and the book by Neamen [9].

2.1 Semiconductor Materials

Semiconductor materials are unique in that their conductivities bridge the gap between insulators and conductors. The material generally forms one of three types of crystals, which are amorphous, polycrystalline and single crystal. The size of the ordered region defines which of the crystal types that describe the semiconductor material. Amorphous materials are such that the atoms have a small degree of order that does not extend beyond that of a few atoms. Polycrystalline materials have regions in which a high degree of order exists that extends over the distance of many atoms. These regions of order form pockets of single crystal material that vary in orientation, shape, and size with respect to one another. Single crystal materials have a high degree of atomic order throughout the entire material. Single crystal material is generally preferred due to the

electrically degrading effects of the grain boundaries that are present within polycrystalline materials (Figure 4).

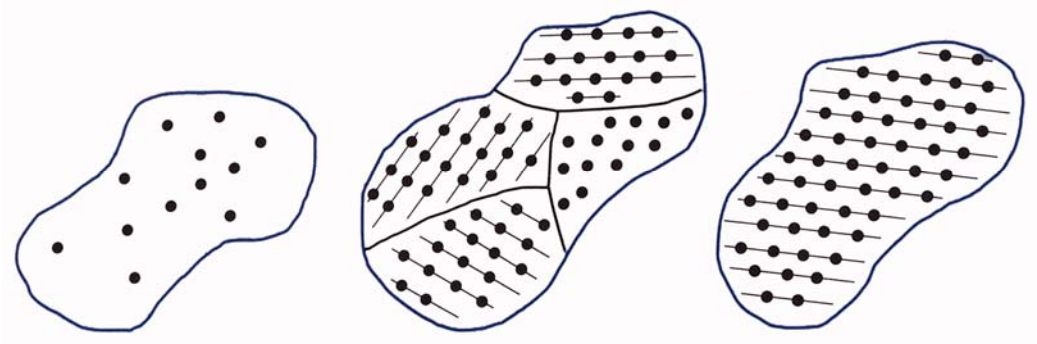

Figure 4. This figure schematically shows the three crystal types: amorphous (left), polycrystalline (middle), and single crystal (right) [9]

2.1.1 Energy Bands

The Pauli exclusion principle states that no two electrons can occupy the same quantum state. This principal also states that joining atoms to form a crystal has no effect on the total number of quantum states. This is true regardless of how large the crystal is. As atoms are brought together to form a crystal, their inter-atomic spacing decreases and their electrons begin to interact with one another to form bands of allowed and forbidden energy levels. The two allowed bands of energy are called the conduction and valence band. The band of forbidden energy levels is referred to as the bandgap, E_g. Electrons completely fill the valence band and are excited into the conduction band through the absorption of energy in an amount equal to or greater than the energy of the bandgap. This energy can be either a phonon from the thermal energy present in the lattice or from a photon. The photon must have a wavelength such that its energy is greater than the bandgap energy. Photon energy is wavelength dependent and is determined by $E=h\nu$, where h is Plank's constant and ν is the photon frequency.

Exciting an electron to the conduction band leaves a vacancy in the valence band that can be described by a positive charge carrier called a hole. It is this creation of a charge carrier in each band that is referred to as an electron-hole pair. Figure 5 is a schematic of the process in which an electron is excited from the valence band (leaving behind a hole) across the bandgap and into the conduction band through the absorption of a photon.

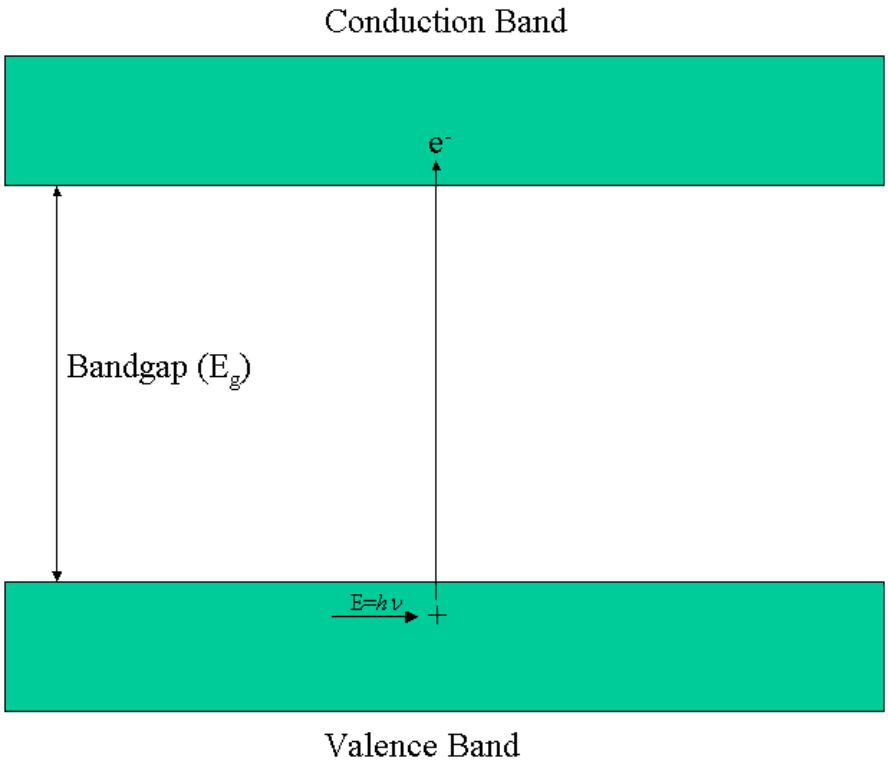

Figure 5. This figure shows the process in which an electron-hole pair is created by the excitation of an electron into the conduction band through the absorption of a photon possessing energy greater than the bandgap.

2.1.2 Extrinsic Semiconductor

Current flow in a semiconductor is mainly related to the number of holes in the valence band and the number of electrons in the conduction band. Adding dopant atoms to the semiconductor material increases these numbers. When dopant atoms are added the

semiconductor changes from what is called an intrinsic material to an extrinsic material, which is the topic of discussion for this section.

There are two types of extrinsic material, n-type and p-type. N-type materials are created by adding dopant atoms that have one more electron than is necessary to complete the covalent bonds with the neighboring intrinsic atoms (donor). The effect is the creation of a discrete energy level within the bandgap that is close to the bottom of the conduction band. As an example, consider silicon that has been doped with phosphorous. Silicon has four electrons in its outer shell and phosphorous has five. Since only four electrons are needed for the phosphorous atom to complete the covalent bonds with its silicon neighbors there is a loosely bound fifth electron that creates an energy level within the bandgap that is 0.044 eV below the bottom of the conduction band. Figure 6 schematically shows the energy levels that are created just below the conduction band. At ambient temperatures and above the free phosphorous electron is thermally excited into the conduction band creating a free carrier. The semiconductor is still electrically neutral due to the fact that the phosphorous atom becomes a positive ion when its electron is excited into the conduction band.

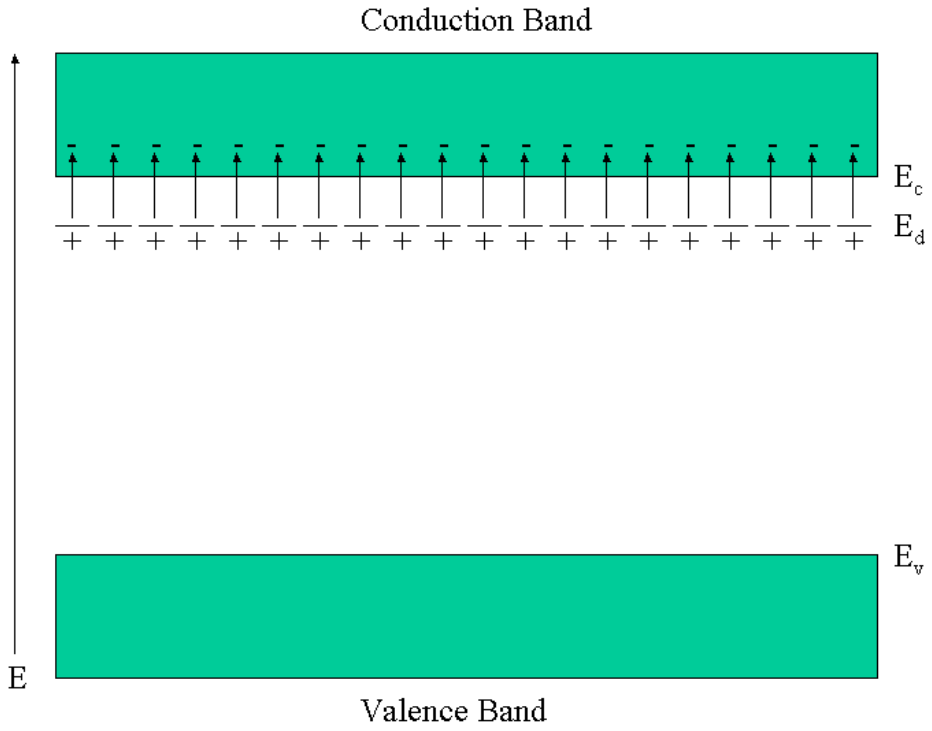

Figure 6. This figure shows the energy band diagram with discrete energy levels just below the conduction band edge due to the presence of donor atoms. The free electrons from the donors are thermally excited into the conduction band.

Similarly, doping silicon with a boron atom creates a discrete energy level 0.045 ev above the valence band due to the boron atom having only three electrons in its outer shell (acceptor). Again, thermal energy present at ambient temperatures is enough to excite an electron from the valence band into the energy level created by the boron atom. This creates a hole in the valence band that is free to participate in the conduction process and is schematically shown in Figure 7.

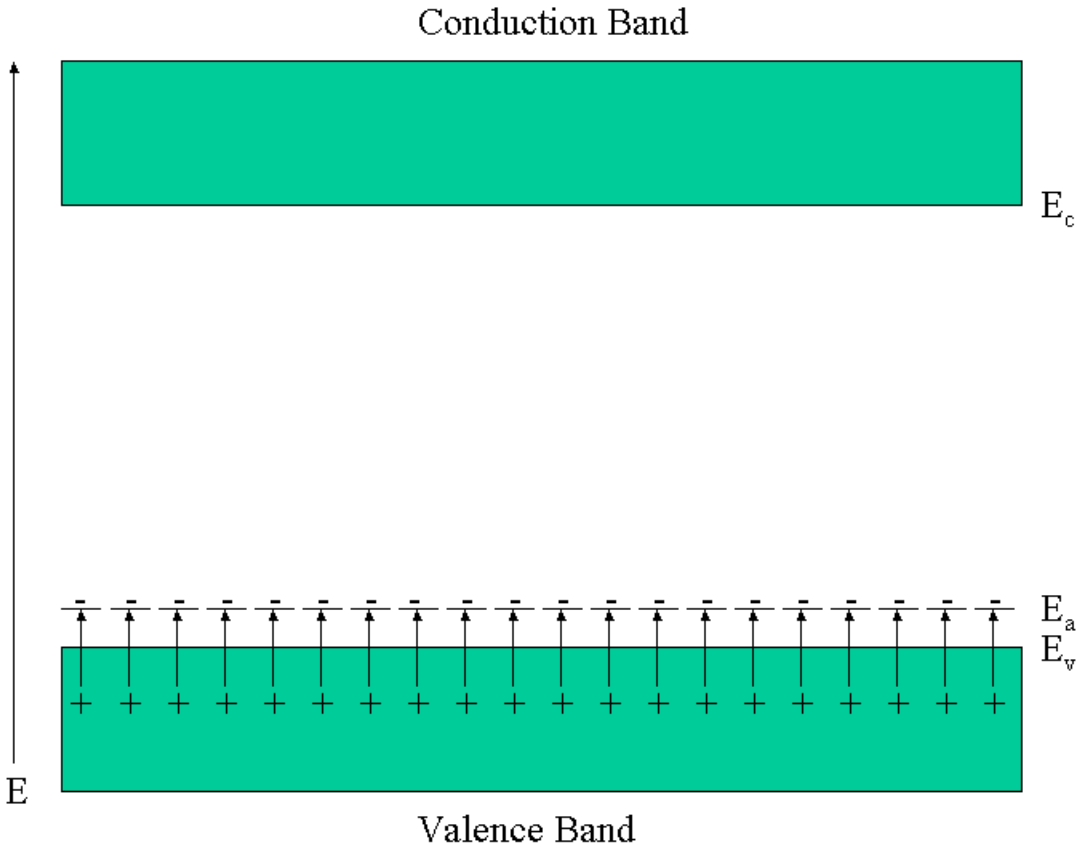

Figure 7. This figure shows the energy band diagram with discrete energy levels just above the valence band edge due to the presence of acceptor atoms. The free electrons are thermally excited into the acceptor sites.

2.2 P/N Junction

P/N junctions are formed by bringing p-type and n-type material into metallurgical contact. This is usually accomplished, in the case of photovoltaic cells, by starting with a p-type substrate and diffusing n-type dopant atoms into the material until a layer of n-type material is formed. The result of this is carrier diffusion in which the high concentration of holes on the p side diffuse into the n side and similarly high concentration electrons diffuse from the n side into the p side. As the carrier diffusion takes place, positively charged atoms are formed on the n side and negatively charged atoms are formed on the p side. These atoms are fixed and create an electric field directed from the n side to the p side. This region is free of carriers and is called the

space charge region or the depletion region. Figure 8 shows these different regions. The magnitude of the electric field is such that equilibrium is formed where the drift of electrons into the n side, due to the electric field, is exactly equal to the diffusion, due to concentration gradients, of electrons into the p side.

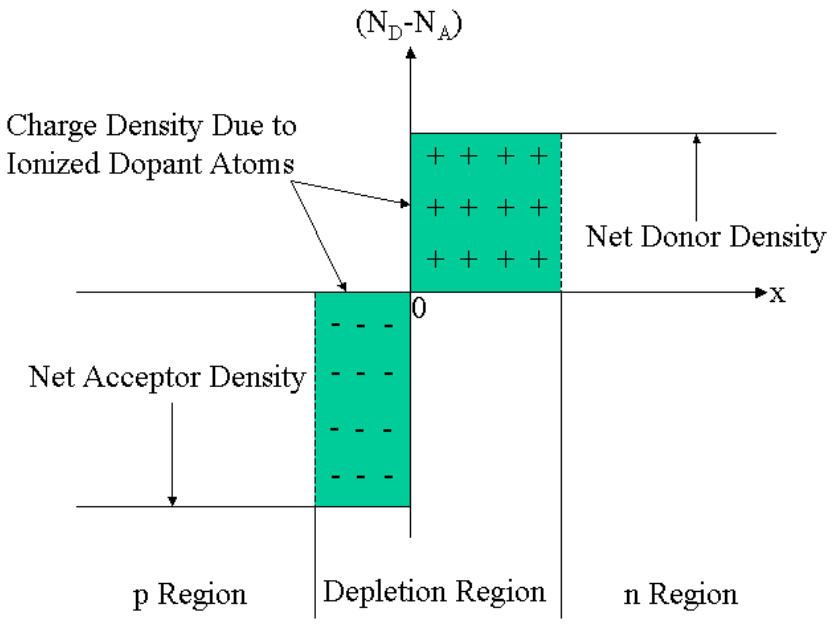

Figure 8. This figure shows the creation of an ionized depletion region at the P/N junction due to carrier diffusion.

2.2.1 Built-in Potential Barrier

Diffusion of carriers due to concentration gradients present within a p/n junction creates charged atoms and in turn forms an electric field. Integrating the electric field provides the solution to the built-in potential barrier (V_{bi}). The amount of voltage that a photocell will produce approaches the value of V_{bi} and therefore is an important parameter.

There are two ways to derive the first order equation for calculating the magnitude of V_{bi}. One way is to take into account the fact that when no external voltage is applied to the

junction (thermal equilibrium) the Fermi energy level (the energy at which the probability of a state being occupied by an electron is exactly one-half) is held constant throughout the junction. This results in the bending of the conduction and valence bands. The magnitude of V_{bi} is then determined by taking the difference of the intrinsic Fermi levels in the n and p sides.

The other method of deriving the equation for V_{bi} is achieved by calculating the total band bending using the equations for electron drift and electron diffusion while taking into account that the two are equal and result in a net electron current flow of zero.

$$J_n = en(x)\mu_n E(x) - eD_n \frac{dn(x)}{dx} = 0 \tag{1}$$

The first term accounts for current due electron drift and the second term accounts for the diffusion current. Eq. (1) describes the current due to electron flow at thermal equilibrium where e is the charge of an electron, *n(x)* is the electron concentration, μ_n is the electron mobility, *E(x)* is the electric field present within the depletion region, and D_n is the electron diffusion coefficient. Using Poisson's equation to relate E(x) to an electric potential, *E(x) = -dV/dx*, and the Einstein equation for relating D_n to μ_n, $D_n=(kT/e)\mu_n$ we now have

$$\frac{dV(x)}{dx} = -\frac{e}{kT}\frac{1}{n(x)}\frac{dn(x)}{dx}. \tag{2}$$

Writing Eq. (2) in an integral form gives

$$\int_{V_p}^{V_n} dV = -\frac{kT}{e}\int_{n_n}^{n_p}\frac{dn}{n} \tag{3}$$

where n_n and n_p are the majority and minority carrier densities, respectively, on the *n* side. The variables *k* and *T* are Boltzmann's constant and the temperature in degrees Kelvin, respectively. The equation for V_{bi} can now be written as

$$V_{bi} = V_n - V_p = V_t \ln\left(\frac{N_A N_D}{n_i^2}\right). \tag{4}$$

This result was derived by using the facts that under complete ionization n_n is equal to the donor density, N_D, and $n_p = n_i^2/N_A$, where n_i^2 and N_A are the intrinsic carrier concentration and acceptor density respectively. V_t is referred to as the thermal voltage and is equal to kT/e. It is appropriate to mention that n_i is the carrier density due to the thermal generation of electron-hole pairs at a given temperature. Figure 9 shows the band bending that occurs to keep the Fermi level constant.

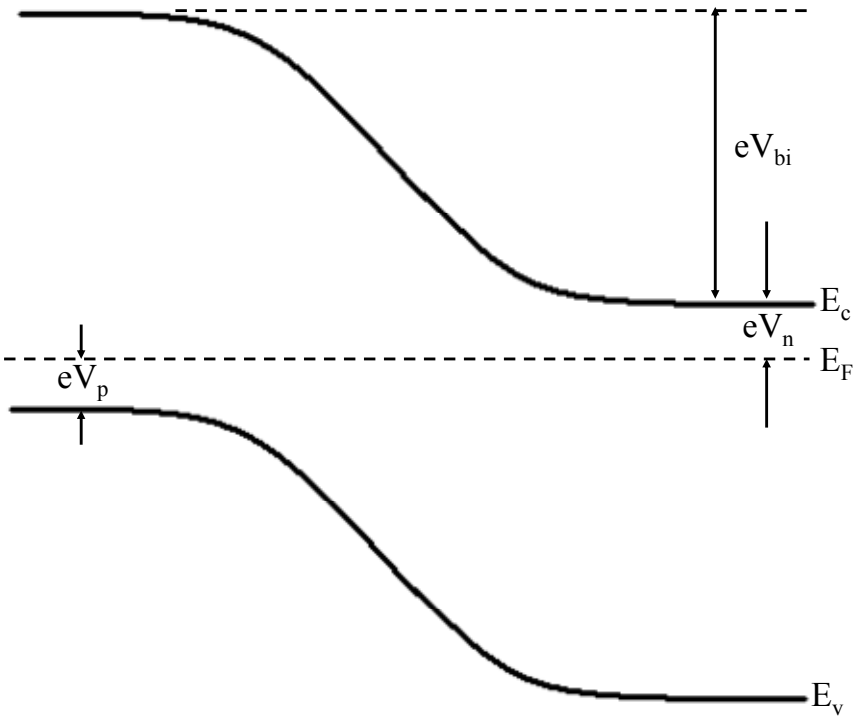

Figure 9. Bending of the conduction and valence bands occur in order to keep the Fermi level constant.

2.2.2 Electric Field

The separation of negative and positive space charge densities within the depletion region creates an electric field. Refer to Figure 10 for a depiction of the volume charge density distribution. In this discussion we assume uniform doping and an abrupt junction approximation. In this assumption the space charge region ends abruptly at x_n on the *n* side and $-x_p$ on the *p* side. From Poisson's equation we know that

$$\frac{d^2V(x)}{dx^2} = -\frac{\rho(x)}{\varepsilon_s} = -\frac{dE(x)}{dx} \tag{5}$$

where $V(x)$ is the electric potential, $\rho(x)$ is the space charge density, and ε_s is the semiconductor permittivity. Referring to Figure 10 we see that the space charge density on the *n* side is eN_D and $-eN_A$ on the p side. We take the origin of the coordinate system, $x = 0$, to be the metallurgical junction. Since the space charge regions end at x_n and $-x_p$ on the n side and p side, respectively, they shall be the locations of the boundary conditions.

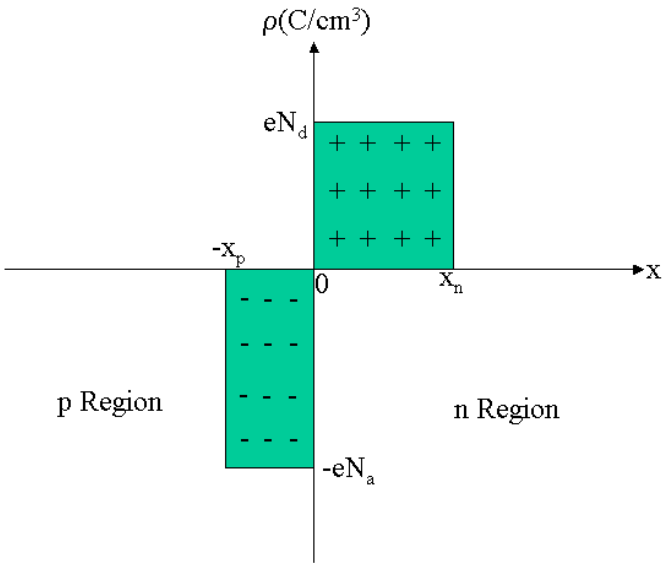

Figure 10. This figure shows the space charge density of a uniformly doped P/N junction.

The electric field on the n side is found by integrating Eq. (5). We now have

$$E(x) = \int \frac{eN_D}{\varepsilon_s} dx = \frac{eN_D}{\varepsilon_s} x + C_1 \tag{6}$$

where C_1 is a constant of integration. Determination of C_1 is done by using the boundary condition of E(x) = 0 at $x = x_n$ and the result is $C_1 = -(eN_D x_n)/\varepsilon_s$. The electric field on the n side is now given by

$$E(x) = -\frac{eN_D}{\varepsilon_s}(x_n - x) \qquad (0 \le x \le x_n). \tag{7}$$

On the p side the electric field is calculated from

$$E(x) = -\int \frac{eN_A}{\varepsilon_s} dx = -\frac{eN_A}{\varepsilon_s} x + C_2 \tag{8}$$

where C_2 is the constant of integration for the p side. The constant is again determined by setting $E(x) = 0$ at $x = -x_p$ and the solution is $C_2 = -(eN_A x_p)/\varepsilon_s$. Plugging the solution for C_2 into Eq. (8) results in

$$E(x) = -\frac{eN_A}{\varepsilon_s}(x_p + x) \qquad (-x_p \le x \le 0). \tag{9}$$

The electric field is continuous since there are no surface charge densities. This continuity also applies to the metallurgical junction at $x = 0$ and by setting Eqs. (7) and (9) equal at $x = 0$ we have,

$$N_A x_p = N_D x_n \ , \tag{10}$$

which states that the number of charges per unit area is the same for the n and p sides of the depletion region. Figure 11 is a plot of the electric field that is present within a uniformly doped depletion region. The electric field is a linear function going from the n

to the p side and its maximum occurs at the metallurgical junction. This field exists even when there is no applied voltage.

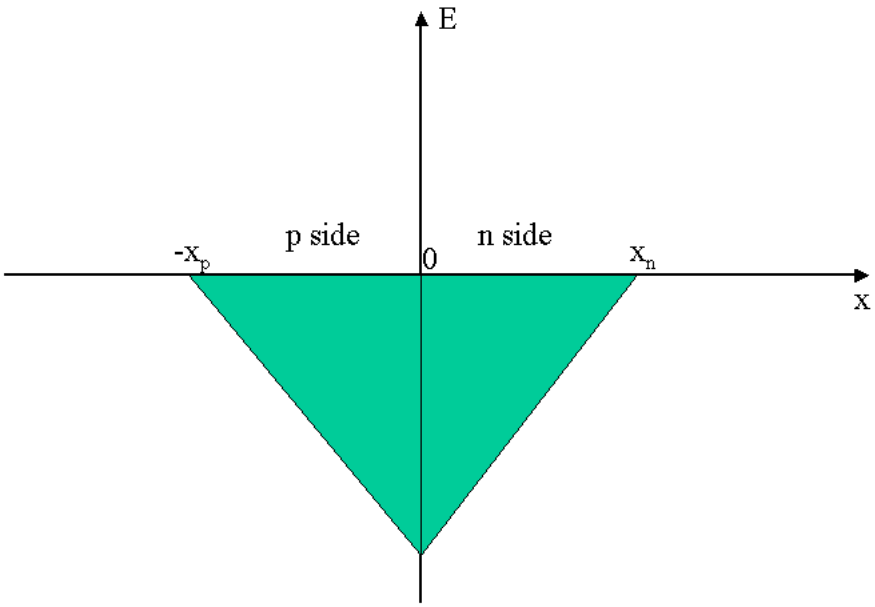

Figure 11. Plot of the electric field within the depletion region.

Integrating the electric field gives the solution for the junction potential. Starting on the p side

$$\phi(x) = -\int E(x)dx = \int \frac{eN_A}{\varepsilon_s}\left(x_p - x\right) = \frac{eN_A}{\varepsilon_s}\left(\frac{x^2}{2} + x \cdot x_p\right) + C_3 \qquad (11)$$

where C_3 is also a constant of integration. Potential is relative and choosing to set the potential equal to zero at $x = -x_p$ allows the constant of integration to be solved and is

$$C_3 = \frac{eN_A}{2\varepsilon_s} x_p^2 . \qquad (12)$$

This gives

$$\phi(x) = \frac{eN_A}{2\varepsilon_s}\left(x + x_p\right)^2 \qquad \left(-x_p \le x \le 0\right). \qquad (13)$$

Finding an expression for the junction potential on the n side is done in a similar manner where the constant of integration for the n side is solved by equating the expressions for the potentials on both sides at $x = 0$. This yields the equation

$$\phi(x) = \frac{eN_D}{\varepsilon_s}\left(x_n \cdot x - \frac{x^2}{2}\right) + \frac{eN_A}{2\varepsilon_s}x_p^2 \qquad \left(0 \le x \le x_n\right). \tag{14}$$

By looking at a plot of Eqs. (13) and (14) (Figure 12) we see that V_{bi} is the magnitude of $\phi(x)$ at $x = x_n$. Solving Eq. (14) at $x = x_n$ gives

$$V_{bi} = \frac{e}{2\varepsilon_s}\left(N_A x_p^2 + N_D x_n^2\right) \tag{15}$$

and explicitly shows that the built-in junction potential is a quadratic function of distance.

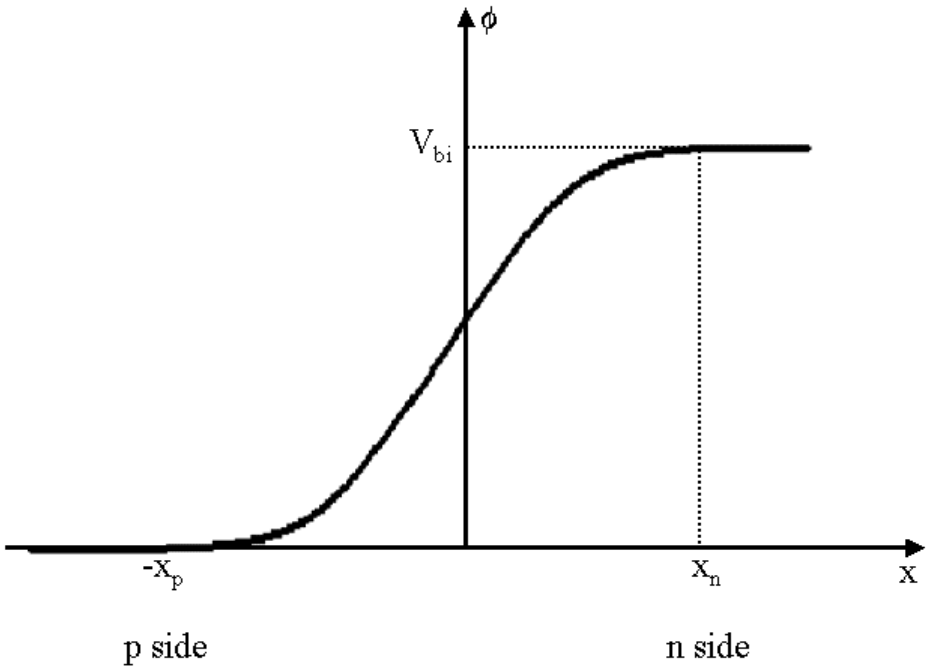

Figure 12. Plot of the electric potential within the depletion region.

2.3 Photovoltaic Current

This Section covers the process that lead to the generation of current in a photocell. First photons of sufficient energy are absorbed and excite electrons into the conduction band thereby creating electron hole pairs. Photovoltaic current is then generated by the diffusion of minority carriers across the depletion region. The result of the following mathematical description for the above two processes gives the ideal equation for a single photocell.

Let's start with the equation for the carrier generation rate within a semiconductor when illuminated by a monochromatic beam of photons,

$$g(x) = \phi\alpha e^{-\alpha x}, \tag{16}$$

where ϕ is the photon flux density ($cm^{-2}s^{-1}$) and α is the absorption coefficient (cm^{-1}) of the semiconductor material.

The one-dimensional continuity equation that describes the diffusion of minority carrier holes in an n-type photocell region is

$$\frac{dp_n(x,t)}{dt} = D_p \frac{dp_n^2(x,t)}{dx^2} - \frac{p_n(x,t)}{\tau} + g(x). \tag{17}$$

This equation states that the rate of change of carrier density is equal to the rate of carrier diffusion minus the recombination rate (dependent on the minority carrier lifetime, (τ) plus minority carrier generation rate due to the incident flux of photons. Under steady state conditions the time dependence of Eq. (17) is eliminated and the carrier density rate of change is zero. Using steady state conditions and inserting Eq. (16) we now have,

$$D_p \frac{dp_n^2(x)}{dx^2} - \frac{p_n(x)}{\tau} = -\varphi\alpha e^{-\alpha x}. \tag{18}$$

Eq. (18) has a general solution consisting of the sum the particular and the complementary solution.

The complimentary solution is found by starting with,

$$\frac{dp_n^2(x)}{dx^2} - \frac{p_n(x)}{L_p^2} = 0, \tag{19}$$

where L_p is the diffusion length and related to the minority carrier lifetime and diffusion coefficient by $L_p = (D_p \tau)^{1/2}$. The solution of (19) is

$$p_n^c(x) = A\cosh(\frac{x}{L_p}) + B\sinh(\frac{x}{L_p}) \tag{20}$$

and the coefficients A and B are determined by the boundary conditions at each side of the active region. Boundary conditions A and B are at the depletion region boundary ($x = x_n$) and the metallic contact ($x = W_n$). At the depletion region boundary, x_n, the carrier density is dependent on the voltage as given by the Shockley equation,

$$p_n(x_n) = p_{n0} e^{\frac{eV}{kT}}, \tag{21}$$

where p_{n0} is the thermal equilibrium minority hole concentration and V is the voltage at the junction. At the other end of the n-type region, W_n, we assume an interface with either a heterojunction or an n^+ material that hinders recombination such that we have an extremely low surface recombination velocity (S). The equation that describes this boundary condition is

$$D_p \frac{dp_n(W_n)}{dx} = -Sp_n(W_n) \tag{22}$$

and for this case we take $S = 0$, and now have

$$\frac{dp_n(W)}{dx} = 0 . \tag{23}$$

Constants A and B are now found by using Eq. (20) along with the boundary conditions in Eqs. (21) and (23) resulting in

$$A = \phi_0 + p_{n0}(e^{\frac{eV}{kT}} - 1) \tag{24}$$

where ϕ_0 has been used to symbolize the often reoccurring quantity, $\frac{\phi\alpha\tau}{\alpha^2 L_p^2 - 1}$, and

$$B = -\frac{A\sinh(\frac{W}{L_p}) + \alpha L_p \phi_0 e^{-\alpha W}}{\cosh(\frac{W}{L_p})} . \tag{25}$$

For the particular solution we use

$$p_n^p(x) = Ce^{-\alpha x} \tag{26}$$

and the constant C is found by taking the derivatives and substituting into Eq. (18) resulting in $C = -\phi_0$. The particular solution becomes

$$p_n^p(x) = -\phi_0 e^{-\alpha x} . \tag{27}$$

We now have a general solution for the minority carrier density in the n-type region by taking the sum of the complimentary solution of Eq. (20) and the particular solution of Eq. (27),

$$p_n(x) = A\cosh(\frac{x}{L_p}) + B\sinh(\frac{x}{L_p}) - \phi_0 e^{-\alpha x} . \tag{28}$$

Minority carrier diffusion current in the n-type region is defined as,

$$I_{DIFF} = -eD_p \frac{dp_n(0)}{dx} , \tag{29}$$

resulting in,

$$I_{DIFF} = \frac{eD_p p_{n0}}{L_p}\tanh(\frac{W}{L_p})(e^{\frac{eV}{kT}} - 1) + eD_p p_{n0}\phi_0\left[\frac{1}{L_p}\tanh(\frac{W}{L_p}) + \frac{\alpha e^{-\alpha W}}{\cosh(\frac{W}{L_p})} - \alpha\right]. \quad (30)$$

This solution consists of a first term that is independent of incident photons and dependent on the junction voltage while the second term is independent of the junction voltage to a first order and proportionally dependent on the incident photon flux.

The first term of Eq. (30) is defined as the dark diode current and is now expressed as,

$$I_D = I_0(e^{\frac{eV}{kT}} - 1), \quad (31)$$

where,

$$I_0 = \frac{eD_p p_{n0}}{L_p}\tanh(\frac{W}{L_p}). \quad (32)$$

The second term is the illumination generated diffusion current,

$$I_{L1} = eD_p p_{n0}\phi_0\left[\frac{1}{L_p}\tanh(\frac{W}{L_p}) + \frac{\alpha e^{-\alpha W}}{\cosh(\frac{W}{L_p})} - \alpha\right], \quad (33)$$

and is directly proportional to the photon flux density (ϕ). We also must take into account the drift current created by carriers that are excited in the depletion region by photons. The electric field in the depletion region is large enough such that most of the photo-generated carriers are swept out before they can recombine. Therefore, the photo-generated current in the depletion region is equal to the product of the number of photons that are absorbed in the depletion and e [10],

$$I_{L2} = eA_{Depl}\phi(1-R)e^{-\alpha x_n}\left(1-e^{-\alpha W}\right), \tag{34}$$

where A_{Depl} is the area of the depletion region. The total illumination generated current, I_L, is the sum of Eqs. (33) – (34).

Photocell current can now be written as,

$$I = I_0(e^{\frac{eV}{kT}} - 1) - I_L = I_D - I_L. \tag{35}$$

The two currents in Eq. (35) can be added and by using superposition an equivalent circuit is drawn by placing the two in parallel as shown in Figure 13. Examining Eqs. (31) - (35) shows that the photovoltaic characteristic I-V curve is the same as the I-V curve for a diode but shifted down by an amount equal to I_L. This is shown in Figure 14.

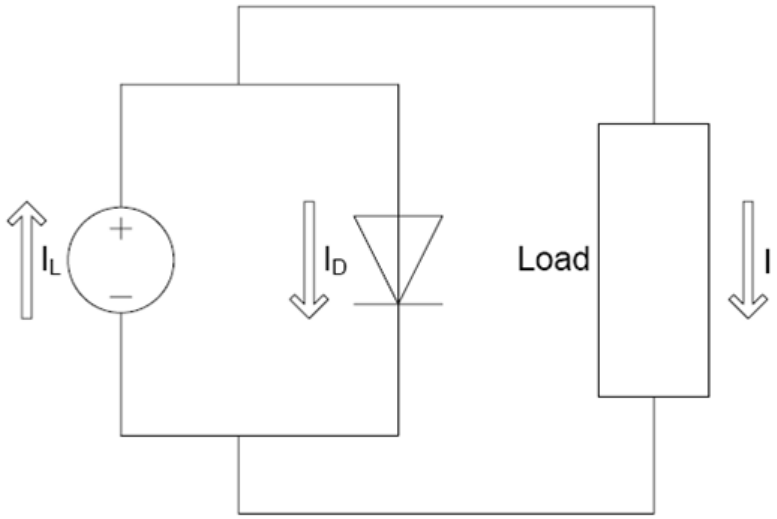

Figure 13. This figure shows the equivalent circuit for a photocell connected to a load. The circuit consists of a photo-generated current source (I_L) in parallel with a forward biased diode that represents the dark current (I_D).

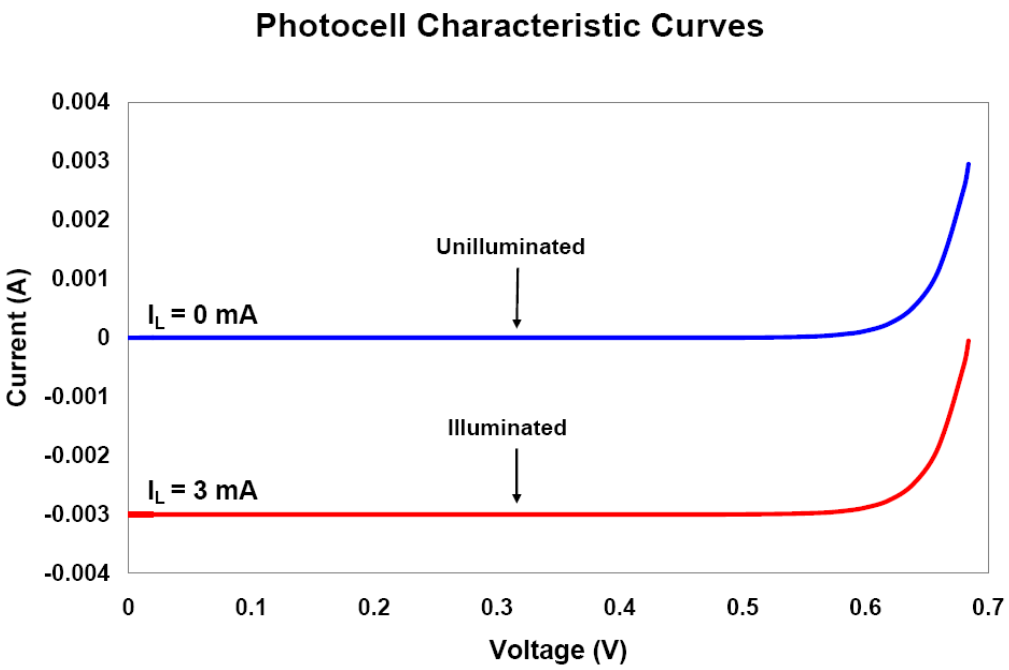

Figure 14. Both the unilluminated and illuminated photocell curve is shown in this figure. When a photocell is illuminated the I-V curve is shifted down by an amount equal to I_L.

2.4 Photocell Performance Parameters

In this section the parameters that are used to describe photovoltaic performance are discussed. These parameters are short circuit current (I_{SC}), open circuit voltage (V_{OC}), peak electric output power (P_{max}), voltage and current at the peak electric output power point (V_{max} and I_{max}, respectively), fill factor (FF), and efficiency (η). Refer to Figure 15 for a graphical depiction of these parameters throughout this discussion.

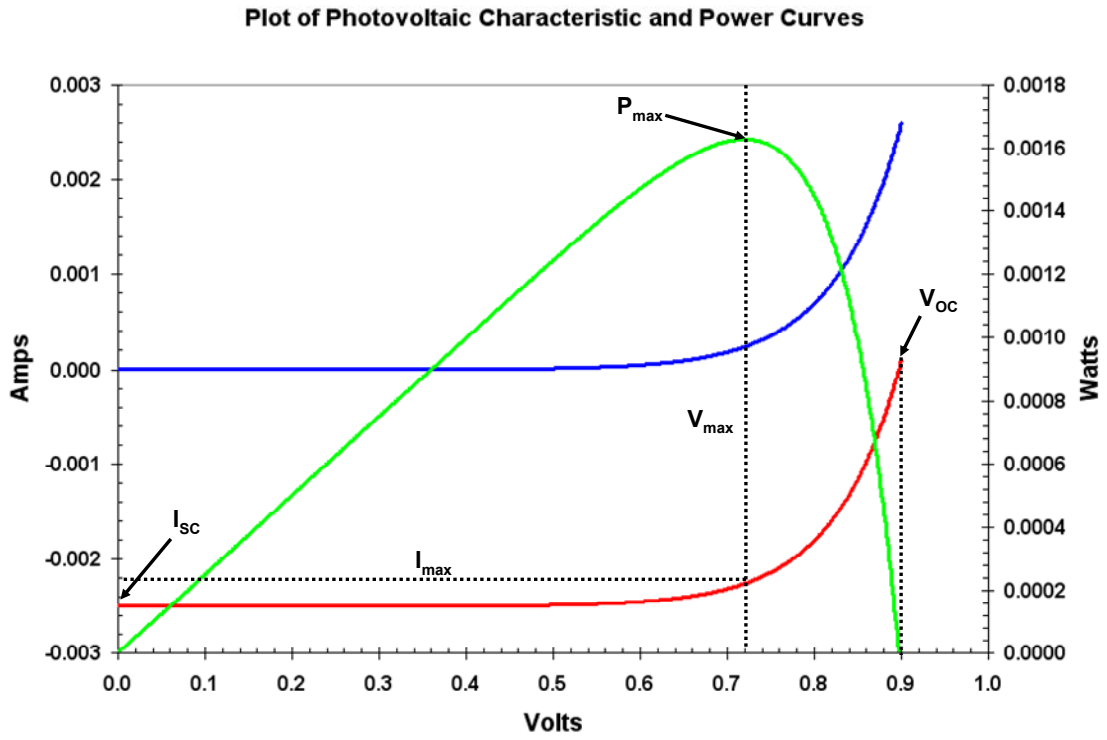

Figure 15. Plot of the photovoltaic characteristic and power curves including parameter notations.

2.4.1 Short Circuit Current

When a photocell is illuminated the I-V curve is shifted into the fourth quadrant by an amount equal to I_L. The illumination generated current is directly proportional to ϕ. The short circuit current, I_{SC}, is defined as the current supplied by the photocell to a shorted load. Note that under short circuit conditions the voltage across the photocell is zero resulting in the first term in Eq. (35) being also equal to zero resulting in $I_{SC} = I_L$.

2.4.2 Open Circuit Voltage

The impedance of the load and I_L determines the photocell output voltage. The larger the load impedance is the larger the photocell output voltage will be, up to the value of the open circuit voltage (V_{OC}). Once V_{OC} is reached the photocell voltage saturates and increasing the load impedance will no longer result in an increase in the photocell output

voltage. Also, V_{OC} is logarithmically related to I_{SC}. This means that a large increase in I_{SC} will result in small increase in V_{OC} and is shown mathematically in Section 2.5 (Eq. (38)). The maximum voltage delivered to a load can also be increased by placing photocells in series.

2.4.3 Output Power

Output power from a photocell is dependent upon the load that is being powered. Figure 15 shows the output power plotted as a function of voltage. There is a point on the power curve at which the there is a maximum. This point is referred to as the peak electric output power, P_{max}. The voltage and current at the peak electric output power point are labeled V_{max} and I_{max}, respectively.

2.4.4 Fill Factor

The parameter fill factor, *FF*, is one metric that is used to describe the photocell performance. Fill factor is used to quantify the "squareness" of the I-V curve and is defined as,

$$FF = \frac{I_{\max} V_{\max}}{I_{SC} V_{OC}} . \tag{36}$$

The primary causes for low values of *FF* are high temperatures and a large series resistance.

Photocell efficiency is probably the most common measure of photocell performance and is defined as

$$\eta = \frac{P_{out}}{P_{in}} = \frac{I_{\max} V_{\max}}{P_{in}} = \frac{I_{SC} V_{OC} FF}{P_{in}} . \tag{37}$$

In the next section an equation for a single photocell is used to develop the mathematical expression that describes the behavior of an SCPA.

2.5 SCPA Voltage and Current

This section derives the ideal equation for an SCPA. An SCPA is simply an array of photocells connected in series in order to achieve a higher V_{OC}. To begin we start by solving the photocell equation, Eq. (35), in terms of the voltage, which gives,

$$V(I) = \frac{nkT}{e} \ln\left(1 + \frac{I_{Li} + I}{I_0}\right). \tag{38}$$

Notice that an additional variable has been added. This variable is commonly referred to as the diode ideality factor, *n*, and is used to account for carrier recombination that occurs within the depletion region. The diode ideality factor has a range between one and two. For a large forward bias where diffusion dominates $n \approx 1$, and for a small forward bias where recombination dominates $n \approx 2$.

When photocells are placed in series the voltage produced by each photocell is summed and the total voltage across the series array is (assuming identical photocells),

$$V(I) = \frac{nkT}{e} \sum_{i=1}^{N} \ln\left(1 + \frac{I_{Li} + I}{I_0}\right). \tag{39}$$

The SCPA current, *I*, is limited by the least illuminated photocell, I_{Li} due to the devices being connected in series.

Current-limiting by the least illuminated cell is discussed in [1] and [8] and demonstrated by performing an experiment in which an SCPA is illuminated with a Gaussian beam and

partially shadowed. The SCPA was manufactured by Sandia's MDL. This particular SCPA consisted of 230 rectangular cells 120 μm x 550 μm in dimension that are arranged to form a circular pattern 4.4 mm in diameter.

Shadowing of the SCPA was achieved by incrementally sliding a razor blade via a translation stage across the protective window covering the SCPA. An entire row consisting of eighteen series connected cells was shadowed and the short circuit current was recorded using a curve tracer. As seen in Figure 16 the current is greatly reduced when the entire row is shadowed, which is the expected result. Diffraction around the razor blade edge and reflections between the razor blade and SCPA account for the less than 100% decrease in output current when the entire row is completely shadowed.

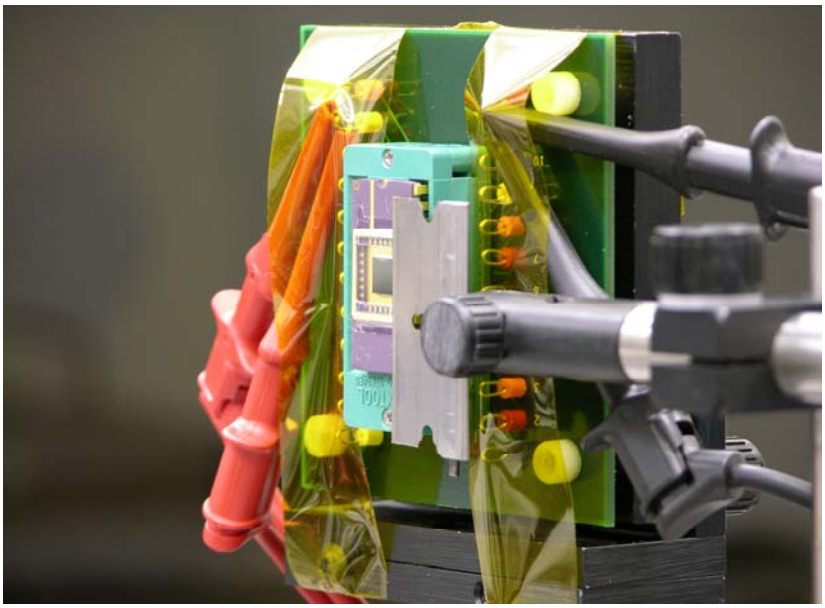

Shadow Test

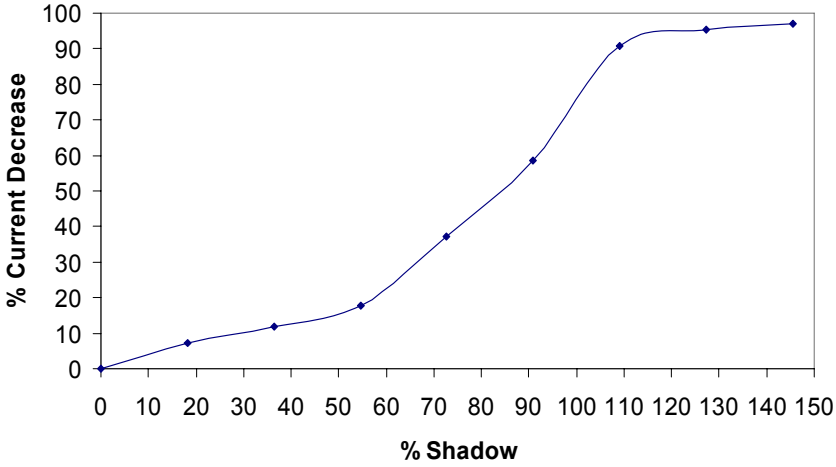

Figures 16a (top) and 16b (bottom). Figure 16a is a picture of the test setup for the shadowing experiment and figure 16b are the results from the experiment illustrating current limiting effect of the least illuminated cell. The non-linear relationship between the percent row shadow and percent decrease in output current is due to the Gaussian illumination.

3 SCPA Modeling

Before discussing the results of the SCPA, we would like to discuss the modeling of the SCPA. Modeling is an important engineering tool. Through modeling we can simulate the performance of circuits that use SCPAs as its power source as well as the behavior of SCPAs under non-uniform illumination. In this chapter two types of models are presented. The first type of model is in the form of a PSpice analog behavioral model. This model functions as an entire array but is lumped into a single element thereby decreasing the simulation runtime and improving convergence. The other model type consists of N ideal photocell circuits connected in series and is useful in investigating the effects of non-uniform illumination.

3.1 PSpice Analog Behavioral Device Model

Circuit simulation is a critical part of the overall design process. Through circuit simulation different designs can be evaluated without the cost of procuring parts and spending large amounts of time assembling and characterizing circuits. Creating a component level PSpice model increases the usefulness of an SCPA by allowing the simulation of circuits that are to be powered by such devices.

Creating a component level model that behaves as an entire array also has the advantage of decreasing simulation times. Current devices manufactured at Sandia consist of over 3600 series connected photocells. Having to simulate each cell individually would be a very time consuming task not only from a stand point of simulation times but also that of drawing the schematic. In addition to decreased simulation and schematic drawing times

there is also the benefit of reducing convergence issues sometimes encountered in PSpice modeling. Convergence issues are more likely in circuits that have large numbers of components. Convergence issues are basically the inability for PSpice to converge to a solution for all of the circuit nodes. One way around this is to decrease the accuracy of the simulation results. Another, more effective, way of reducing convergence issues in SCPA modeling is to derive an equation that describes the behavior of the entire array as if it were a single element.

SCPAs can be modeled by deriving a single equation that approximates the performance of the entire series connected array. Once this equation is derived a curve fit is used to obtain the values for the unknown device parameters. The equation with the appropriate parameter values is then entered into a PSpice analog behavioral model, which then serves as the SCPA component model.

To begin lets start by modifying Eq. (38) for the case of a uniformly illuminated SCPA. In this case the *N* summation terms become identical assuming the series connected photocells are identical. The summation can now be replaced by a factor of *N*, which we will call the array factor and is equal to the number of photocells that are in series. The resulting equation is,

$$V(I) = \frac{nkT}{e} N \ln\left(1 + \frac{I_L + I}{I_0}\right). \tag{40}$$

Solving Eq. (38) for the current gives,

$$I(V) = I_0\left(e^{\frac{eV}{NnkT}} - 1\right) - I_L. \tag{41}$$

Eq. (41) is the equation that is used in the PSpice analog behavioral model. All of the variables except I_0 and n are known. Performing a least squares fit to the SCPA I-V curve is a method that can be used to determine the value of these two unknowns. MathCAD is a math software package that is chosen to do this analysis.

MathCAD requires three pieces of information; the equation that is being fitted to the data, the partial derivative with respect to the unknown variables, and an initial guess for the unknown variables in order to perform the least squares fit. Taking the partial derivative of Eq. (41) with respect to I_0 gives,

$$\frac{\partial I}{\partial I_0} = e^{\frac{eV}{NnkT}} - 1, \tag{42}$$

and the partial derivative with respect to n is,

$$\frac{\partial I}{\partial n} = -\frac{eV}{Nn^2kT} I_0 e^{\frac{eV}{NnkT}}. \tag{43}$$

With these three equations (Eqs. (41) - (43)) and the use of MathCAD, we can now extract the values of I_0 and n. The MathCAD worksheet is shown below in the next two pages (Figure 17).

SCPA MathCAD Curve Fitting Worksheet

Enter SCPA test data into table below

Data :=

	Voltage (V)	Current (A)
0	0.05	$-3\cdot10^{-5}$
1	0.1	$-3\cdot10^{-5}$
2	0.15	$-3\cdot10^{-5}$
3	0.2	$-3\cdot10^{-5}$
4	0.25	$-3\cdot10^{-5}$

Define constants and known device parameters

$q := 1.6\cdot10^{-19}$

$T := 300$

$k := 1.38\cdot10^{-23}$

$I_L := 30\cdot10^{-6}$

$N := 24$

Define column 0 and column 1 in the Data table as the SCPA voltage and current, respectively.

$voltage := Data^{\langle 0 \rangle}$ $current := Data^{\langle 1 \rangle}$

SCPA characteristic equation and partial derivatives. I_0 and n are defined here as B_0 and B_1, respectively, for MathCAD formatting purposes.

$$I_1(v,B) := \begin{bmatrix} B_0\cdot\left(e^{\frac{q\cdot v}{N\cdot B_1\cdot k\cdot T}} - 1\right) - I_L \\ e^{\frac{q\cdot v}{N\cdot B_1\cdot k\cdot T}} - 1 \\ B_0\cdot -\frac{q\cdot v}{\left(B_1\right)^2\cdot N\cdot k\cdot T}\cdot e^{\frac{q\cdot v}{N\cdot B_1\cdot k\cdot T}} \end{bmatrix}$$

Ideal SCPA Characteristic Equation

Partial Derivative with Respect to I_0 (B_0)

Partial Derivative with Respect to n (B_1)

Figure 17a. Page one of the MathCAD curve fitting worksheet.

Enter a guess for I_0 and n into the array below. I_0 is in row 1 and n is row 2.

$$\text{guess} := \begin{pmatrix} 7.62 \cdot 10^{-16} \\ 1 \end{pmatrix} \begin{matrix} I_0 \\ n \end{matrix}$$

Curvefitting function

$$I_{fit} := \text{genfit}(\text{voltage}, \text{current}, \text{guess}, I_1)$$

Values for I_0 and n as determined by the curve fi t.

$$I_{fit} = \begin{pmatrix} 7.651 \times 10^{-14} \\ 1.35 \end{pmatrix} \begin{matrix} I_0 \\ n \end{matrix}$$

The function below is the SCPA characteristic equation using the values of I_0 and n from the curve fit.

$$I_{result}(v) := I_1(v, I_{fit})_0$$

Plot of Data and Curve Fit

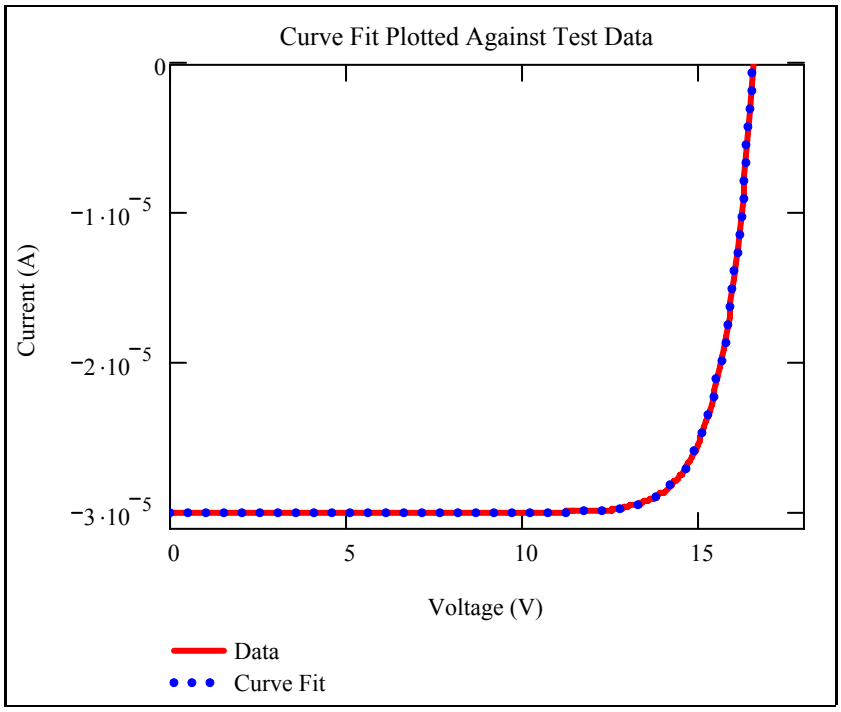

Figure 17b. Page two of the MathCAD curve fitting worksheet.

The accuracy of the worksheet is tested by entering an I-V curve that was generated in Excel using arbitrarily chosen values of $I_0 = 7.62*10^{-14}$ and $n = 1.35$. Once the generated I-V curve is entered into the SCPA data table, guess values for I_0 and n are chosen. The accuracy of the guess values is not critical. Guess values that differ by orders of magnitude have little effect on the results of the curve fit. If this worksheet is accurate it will determine values of I_0 and n that matches those used to generate the test I-V curve. Referring to Figure 17 we see that the MathCAD curve fitting worksheet produces values of I_0 and n that match closely with that of the values used to generate the data in Excel. The RMS error for the curve fit is a mere $1.868*10^{-6}$ %.

Now that the accuracy of the curve fitting worksheet has been verified, it can be used to extract the values I_0 and n from an SCPA I-V curve for use in a PSpice model. A device that is of current interest at Sandia is a 12 V SCPA. The SCPA consists of 12 series connected GaAs photocells and is manufactured by JDSU (See Figure 1a). A model for this SCPA is created by first acquiring the I-V curve using a curve tracer. The illumination source in this case is a 3 W laser diode that emits 810 nm light from a 0.22 NA fiber optic pigtail. The core diameter of the fiber optic pigtail is 100 μm. Since this is the illumination source required for the application, the SCPA will be modeled under such illumination. A Tektronix 370B curve tracer is used to acquire the I-V curve for the illuminated SCPA. Once the I-V curve is acquired it is entered into the curve fitting worksheet and the values of I_0 and n are extrapolated. The results are displayed below in Figure 18.

MathCAD Curve Fit Results

Values for I_0 and n as determined by the curve fit.

$$I_{fit} = \begin{pmatrix} 8.479 \times 10^{-6} \\ 4.536 \end{pmatrix} \begin{matrix} I_0 \\ n \end{matrix}$$

Plot Comparing the Test Data, and Curve Fit.

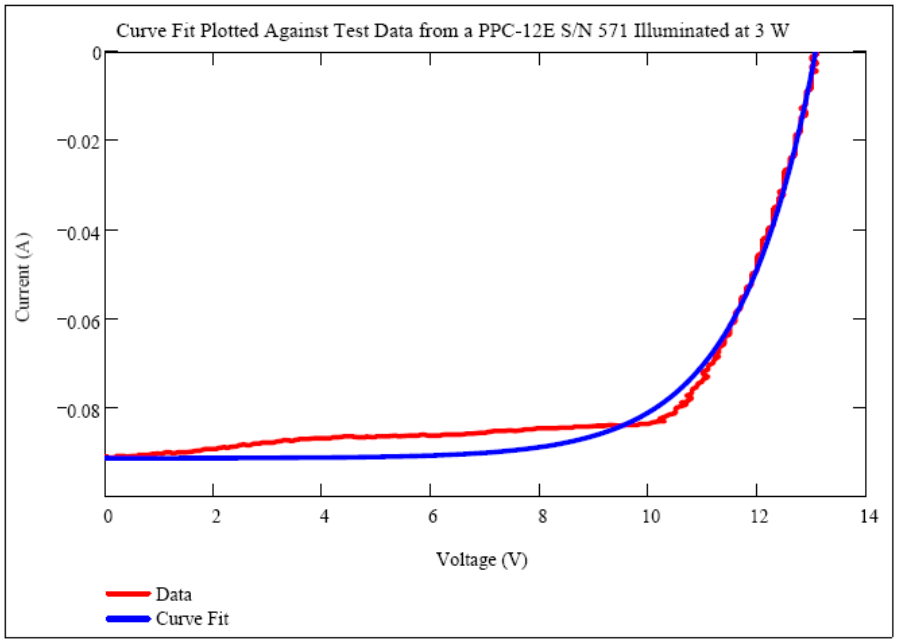

Figure 18. Results from the MathCAD curve fit.

Values for I_0 and n as determined by the curve fit are $8.479*10^{-6}$ and 4.365, respectively. A plot of the SCPA characteristic equation using these values for I_0 and n is in good agreement with the test data and the RMS error is only 3.83%. The deviation between the curve fit and the test data is caused by series resistance and the non-uniform illumination of the SCPA. Series resistance lowers the voltage that is across the p/n junction and reduces the accuracy of the model at the "knee" of the I-V curve. Light propagating from a multi-mode fiber has a non-uniform intensity profile and the SCPA

characteristic equation does not take this into account. These two factors easily explain the high value of *n*.

As this model stands, it would slightly outperform the device it is based on. A good engineering practice is to a introduce margin. Reducing the value used for I_L in the curve fitting worksheet will produce a model which understates the actual device performance. To demonstrate this, the value for I_L used in the curve fitting worksheet is reduced from the actual value of 91.3 mA to 86.8 mA. The results of this are displayed in Figure 19.

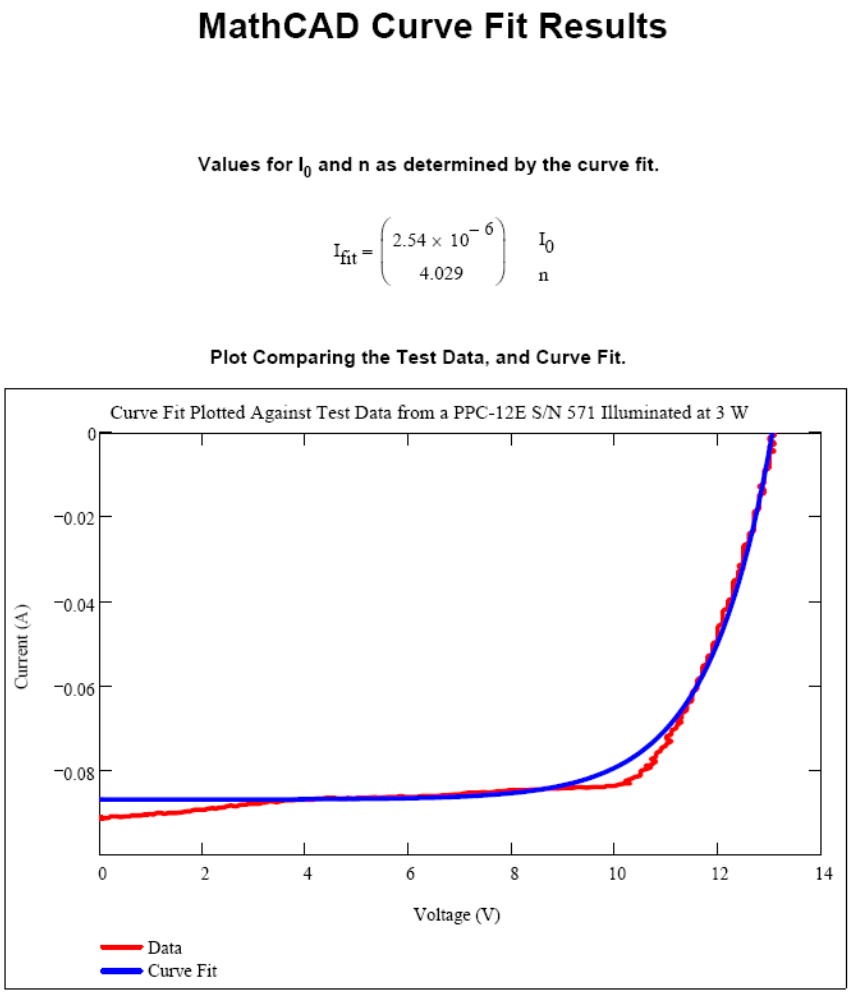

Figure 19. Curve fit results using a conservative value of I_L.

Notice the changed values of I_0 and n. They are now $2.54*10^{-6}$ and 4.029, respectively. Again, the high value of n is attributed to series resistance and non-uniform illumination. Using this technique, we can generate values that will produce a model with performance margin. In other words the model generated using these values will not overstate the actual device performance. The RMS error for this curve fit is 3.02%. A PSpice model can now be created by using Eq. (39) with above values of I_L, I_0, and n into an analog behavioral model.

There are several types of analog behavioral models in PSpice. An electrical component that most closely matches the behavior of an SCPA is a voltage controlled current source and as such an analog behavioral model with these features is chosen. The PSpice part reference for the model used is ABMII1. The argument in the exponential of Eq. (39), $\frac{eV}{NnkT}$, is simplified before it is imputed into the PSpice Model. Using the value of n = 4.029, as determined by the curve fit, gives the result of V * 0.7994. Figure 20 shows the PSpice part schematic for the analog behavioral model.

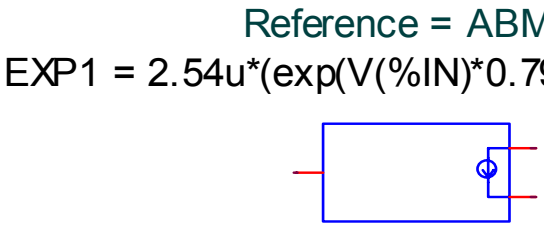

Figure 20. This figure shows the schematic for a PSpice analog behavioral model.

The two pins on the right are connected to the current source and the pin on the left is the control pin with infinite input impedance. The voltage present at the control pin dictates

the output from the current source as indicated by the term V(%IN) in the characteristic equation of the device model. Connecting the control pin on the left to the top left pin on the right (+ current) creates a non-linear voltage controlled current source that behaves identically to a SCPA.

Performance of the PSpice model can be verified by generating an I-V curve and comparing it to the I-V curve of the actual device. Placing a voltage source in parallel with the current source and connecting the control pin to monitor the voltage present at the + node will accomplish this. The amplitude of voltage source is incrementally increased up to the V_{OC} of the SCPA while measuring the loop current. Figure 20 shows the schematic used to verify the model performance.

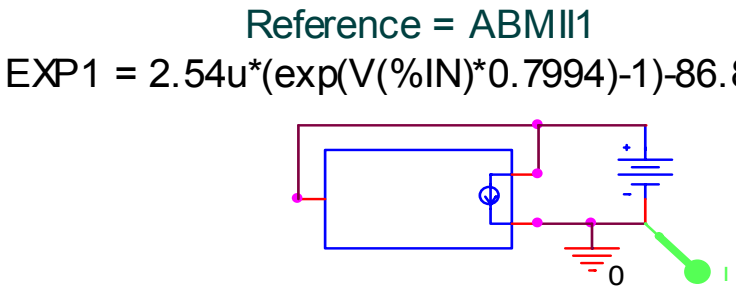

Figure 21. Schematic of the PSpice model test circuit.

The voltage source amplitude can be incrementally increased by selecting the DC Sweep option in the PSpice simulation settings window and choosing the appropriate start value, end value, and voltage increment which, in this case, was 0 V, 13.5 V and 0.05 V respectively. Figure 21 is a screen print of the simulation settings used to generate the I-V curve.

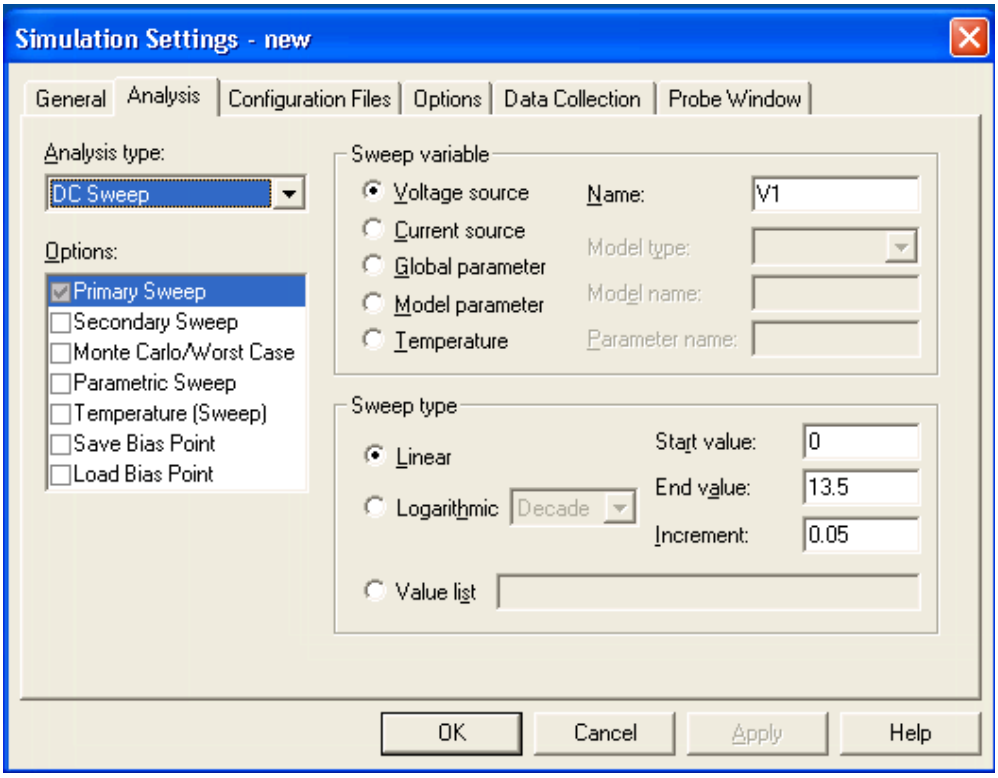

Figure 22. PSpice simulation settings.

The resulting I-V curve from the PSpice model simulation is shown in Figure 23. At a first look the model appears to be accurate. The V_{OC} of 13 V and I_{SC} of 86.8 mA are consistent with the values seen from the curve fit. To be sure, the results from the PSpice simulation are plotted against the actual device and the fitted I-V curve from the curve fitting worksheet. This is shown in Figure 24.

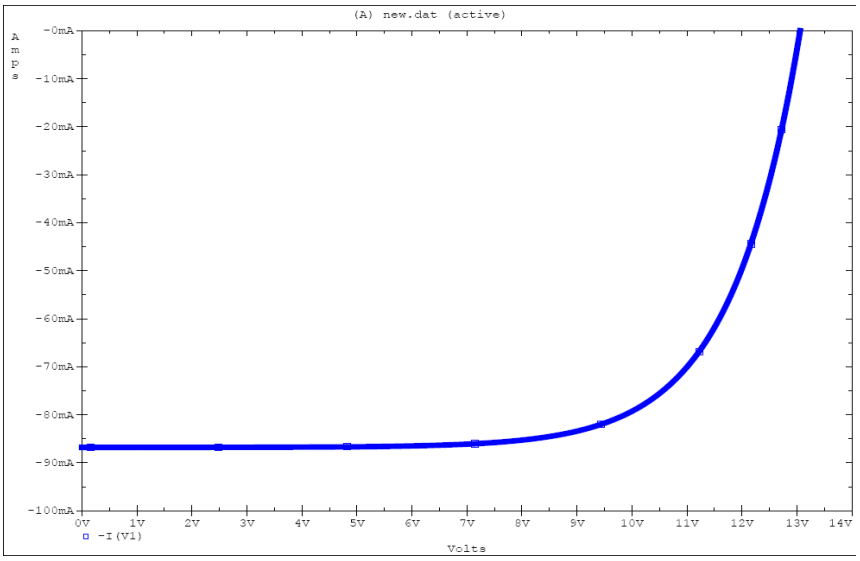

Figure 23. Resulting I-V curve from the PSpice model simulation.

As can be seen in Figure 24 the plots of the I-V curves for the curve fit and PSpice models are identical and perform slightly worse than the actual device. Table 1 compares the values of the main performance parameters of the actual device to the PSpice model. These results conclude that SCPAs can be modeled by first extracting the values for I_o and n through curve fitting to the device I-V curve and then using Eq. (39) (with the fitted values) in an analog behavioral PSpice model.

Table 1. Comparison of the main performance parameters for the actual device and PSpice model.

	Test Data	Pspice Model	Difference	% Difference
V_{oc} (V)	13.1	13	0.1	0.76
I_{sc} (mA)	91.3	86.8	4.5	4.93
P_{max} (mW)	847	796	51	6.02

MathCAD Curve Fit Results

Values for I_0 and n as determined by the curve fi t.

$$I_{fit} = \begin{pmatrix} 2.54 \times 10^{-6} \\ 4.029 \end{pmatrix} \quad \begin{matrix} I_0 \\ n \end{matrix}$$

Enter PSpice simulation data into table below to verify model performance.

PSpice :=

	0	1
0	0	-0.087
1	0.05	-0.087
2	0.1	-0.087
3	0.15	-0.087
4	0.2	-0.087
5	0.25	-0.087

Plot Comparing the Test Data, Curve Fit, and PSpice model.

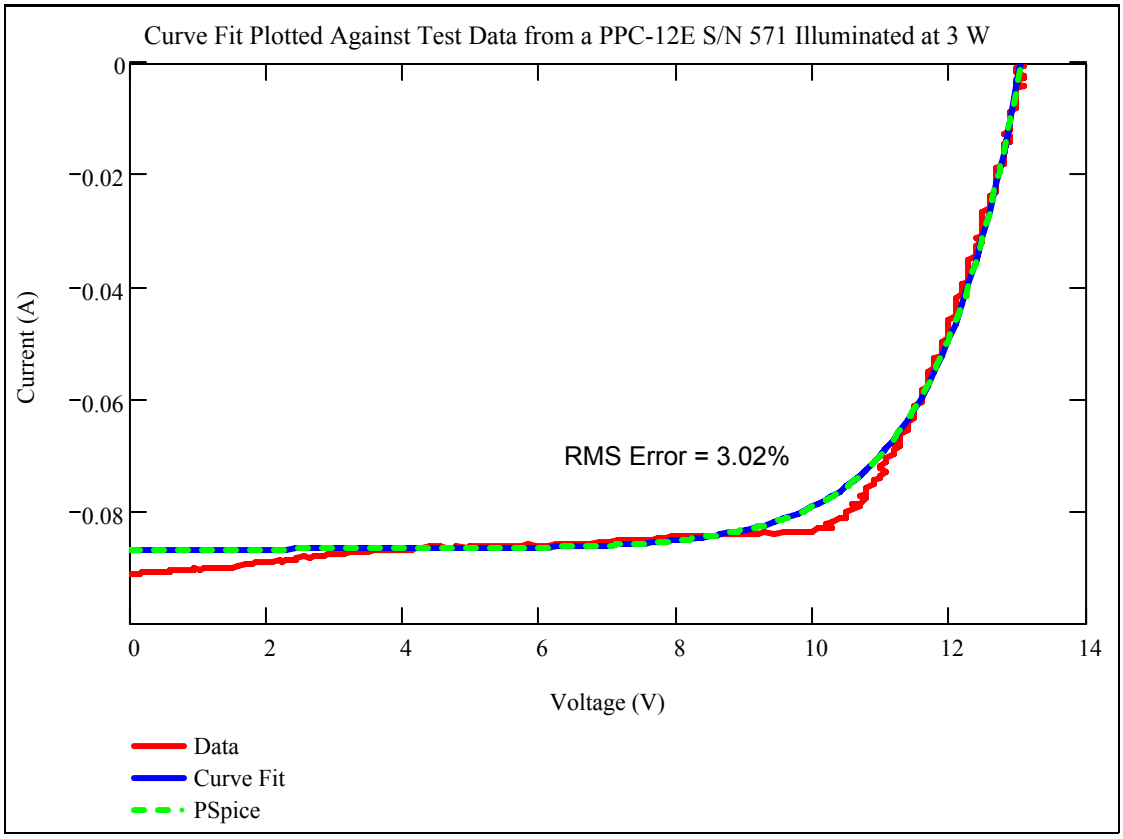

Figure 24. Comparison plot of the device, curve fit, and PSpice I-V curves.

3.2 PSpice Modeling of Non-Uniform SCPA Illumination

In this section modeling of non-uniform SCPA illumination is discussed. This type of modeling simulates the performance of the array when some of the cells are illuminated at different intensities than others. The equivalent circuit for a photocell consists of a current source in parallel with a forward biased diode (Figure 13). The PSpice model consists of N equivalent photocell circuits placed in series. Non-uniform illumination is simulated by changing the amplitudes of current sources that are in parallel with the diodes. Amplitudes for the current sources can be determined by,

$$I_L = RI_P A_P , \tag{44}$$

where R is the wavelength dependent responsitivity (A/W), I_p is the illumination intensity incident upon the photocell (W/cm^2), and A_p is the area of the photocell (cm^2) [11].

From the discussion in Section 2.5 it is expected that the PSpice simulation of non-uniform illumination will result in the electrical current through the entire array being limited by and equal to the lowest amplitude current source. The voltage should also be slightly lower than that of a uniformly illuminated array. Non-uniform illumination should not affect the voltage near as much as it does the current since the voltage is related to the natural log of the current (Eq. (39)). In other words large variations in the current result in small variations in the voltage.

Modeling of non-uniformly illuminated SCPAs also begins by fitting to the curve of the device that is to be modeled to determine the values of I_o and n. Once these values are determined, they are inserted into a PSpice diode model. To begin, two single junction Si

photovoltaic cells manufactured at Sandia's MDL are individually characterized by taking the I-V curves for each of the devices under dark and illuminated conditions. Each device was characterized under two levels of illumination. The two levels of illumination were such that the photocells each generated 500 μA and 750 μA. Once both of the photocells were characterized individually they were characterized in series under dark conditions as well as equal and unequal levels of illumination. See Figure 25 for the schematic of the test setup.

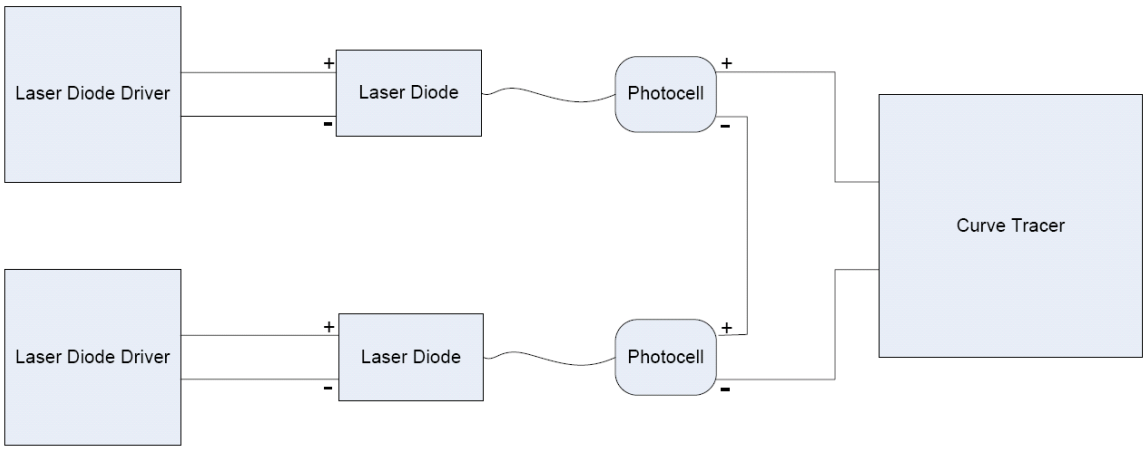

Figure 25. Schematic of the setup used to perform the non-uniform illumination experiment.

Comparing the I-V curves of the two devices at each level of illumination shows that their performance is almost identical (Figure 26). As such, the same PSpice diode model will be used for both photocells while separate models will be used to represent the photocells at each level of illumination. The need for separate models at each level of illumination arises from the high series resistance present within the photocells and the internal resistance of the curve tracer used to collect the data.

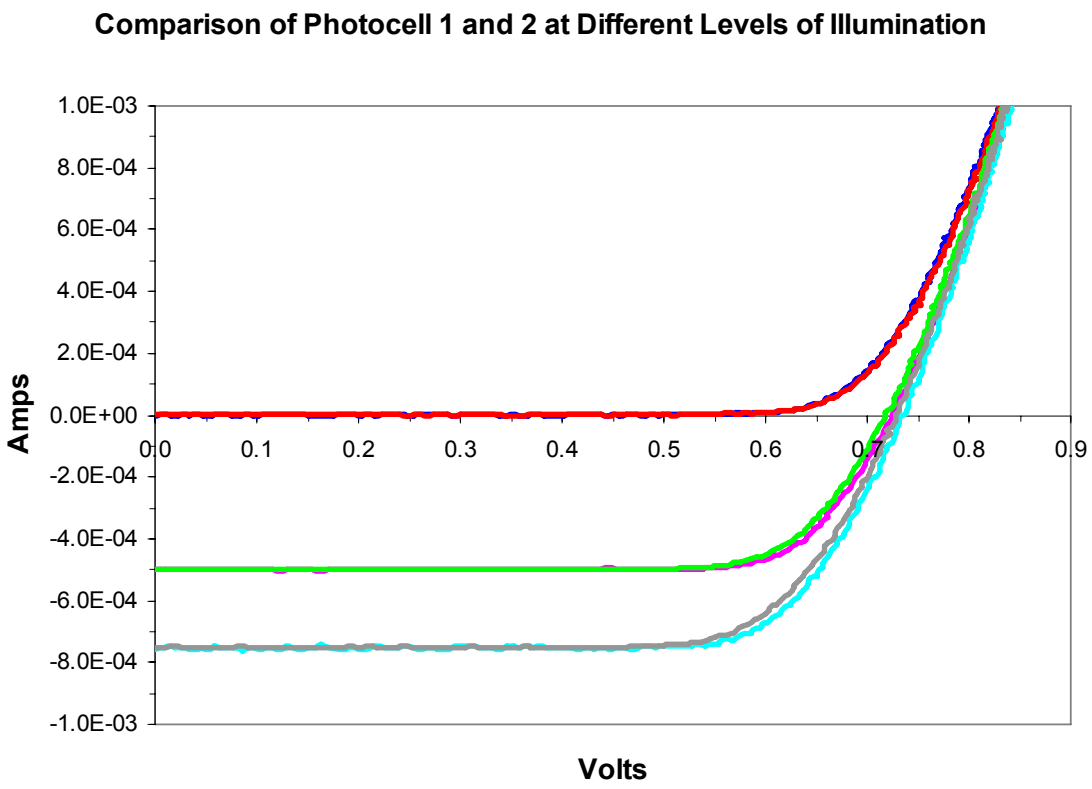

Figure 26. Comparison plot of photocell 1 and 2 at different levels of illumination.

The curve fitted values of I_o and n for the photocells under dark and illuminated conditions are shown in Figures 27-29. These values are then used in the three PSpice diode models representing dark, 500 µA, and 750 µA illumination conditions.

MathCAD Curve Fit Results

Values for I_0 and n as determined by the curve fit.

$$I_{fit} = \begin{pmatrix} 1.695 \times 10^{-8} \\ 2.915 \end{pmatrix} \begin{matrix} I_0 \\ n \end{matrix}$$

Plot Comparing the Test Data, and Curve Fit.

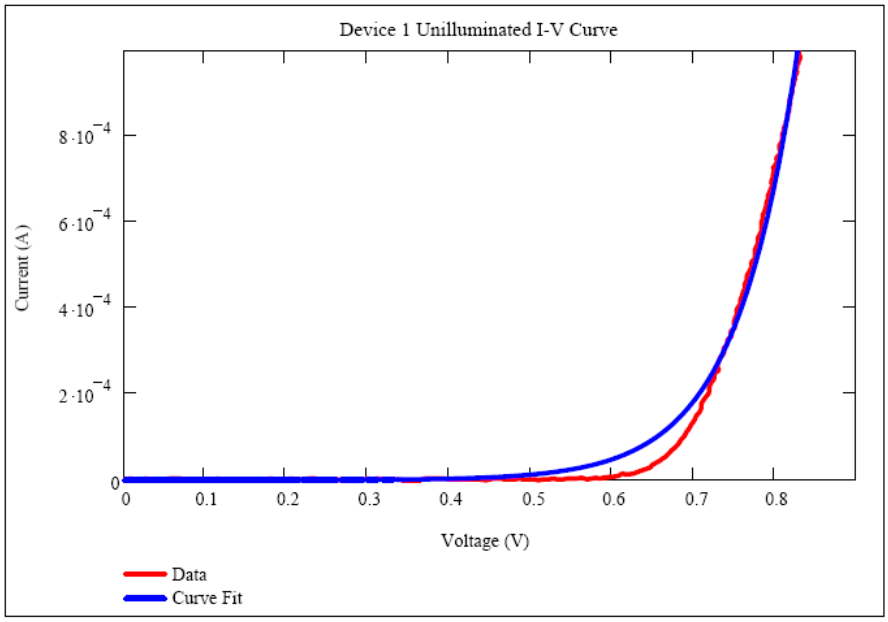

Figure 27. Curve fitting results from photocell 1 under dark conditions.

MathCAD Curve Fit Results

Values for I_0 and n as determined by the curve fit.

$$I_{fit} = \begin{pmatrix} 1.165 \times 10^{-9} \\ 2.15 \end{pmatrix} \begin{matrix} I_0 \\ n \end{matrix}$$

Plot Comparing the Test Data, and Curve Fit.

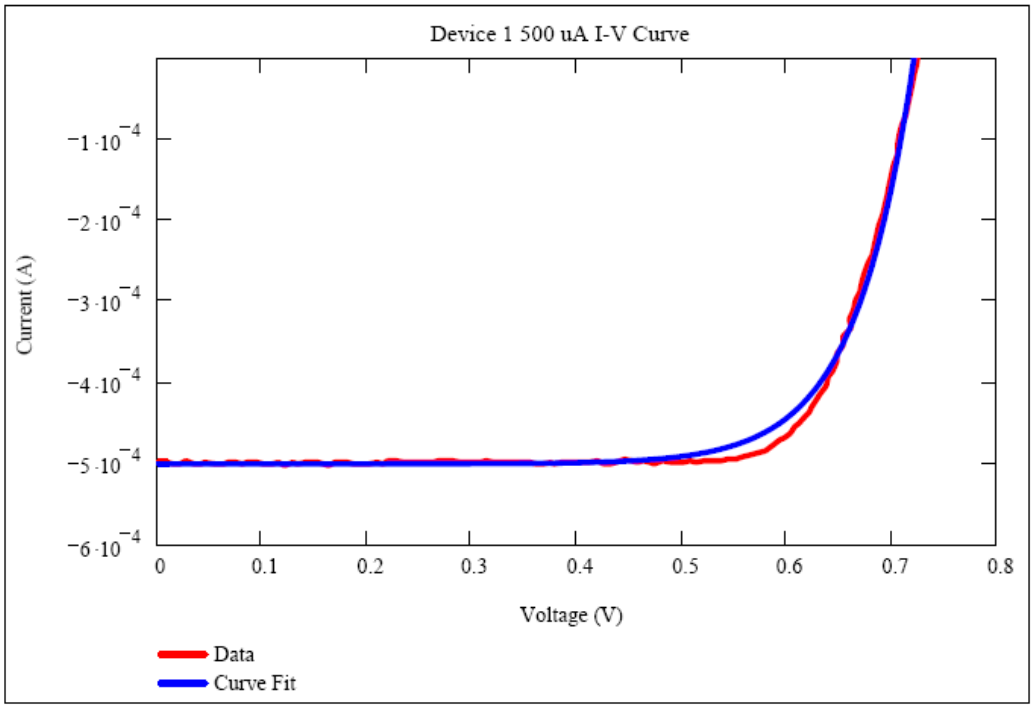

Figure 28. Curve fitting results from photocell 1 under 500 µA conditions.

MathCAD Curve Fit Results

Values for I_0 and n as determined by the curve fit.

$$I_{fit} = \begin{pmatrix} 1.612 \times 10^{-8} \\ 2.626 \end{pmatrix} \begin{matrix} I_0 \\ n \end{matrix}$$

Plot Comparing the Test Data, and Curve Fit.

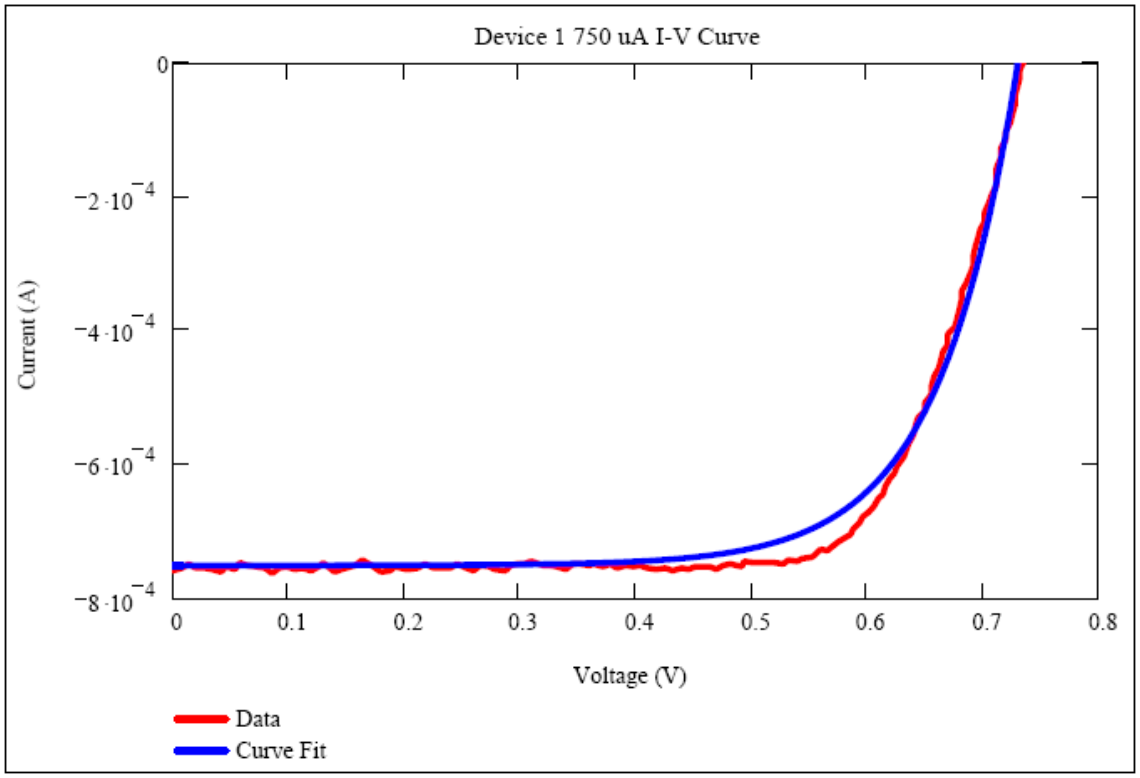

Figure 29. Curve fitting results from photocell 1 under 750 µA conditions.

The simulation results from the PSpice models are then compared to the I-V curves to confirm model accuracy. Figure 30 is the PSpice schematic and Figures 31-33 shows the comparison plots of the simulation results and the test data. Once the individual photocell models are determined to be accurate, they are placed in series to simulate a

non-uniformly illuminated array consisting of two series connected photocells. The series non-uniform illumination simulation results are then compared to the test data from the two photocells in series.

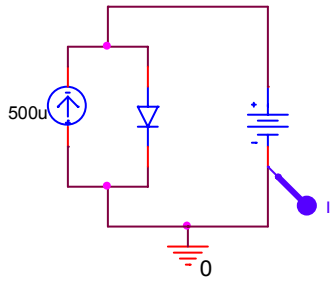

Figure 30. PSpice schematic of photocell test circuit.

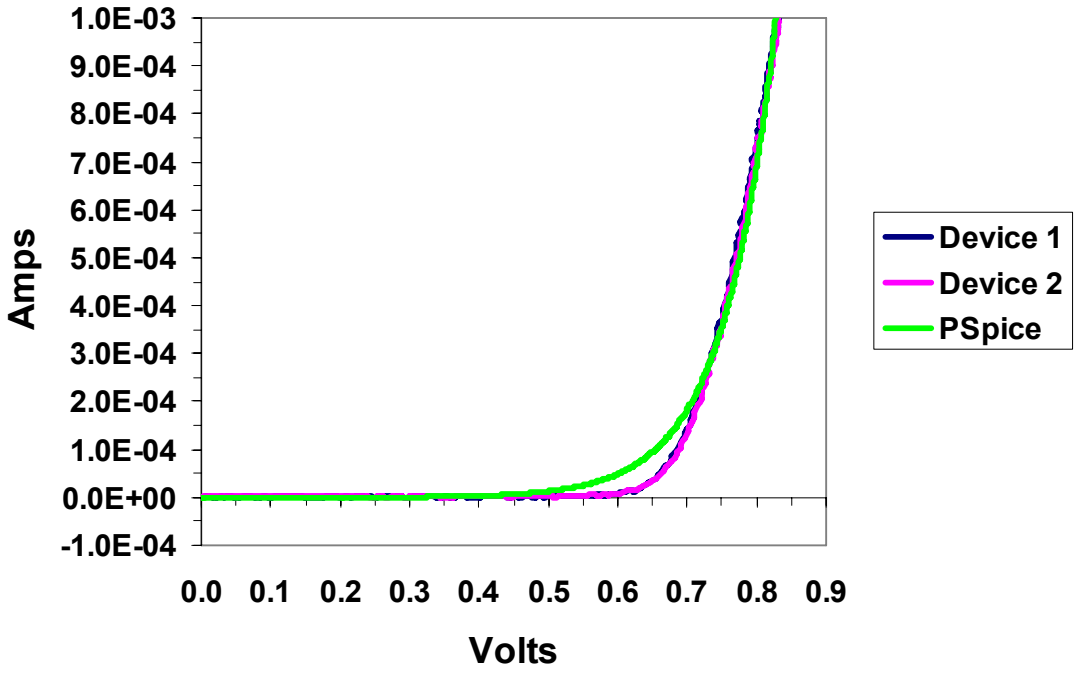

Figure 31. Plot comparing the dark I-V curves of the test data and the PSpice model.

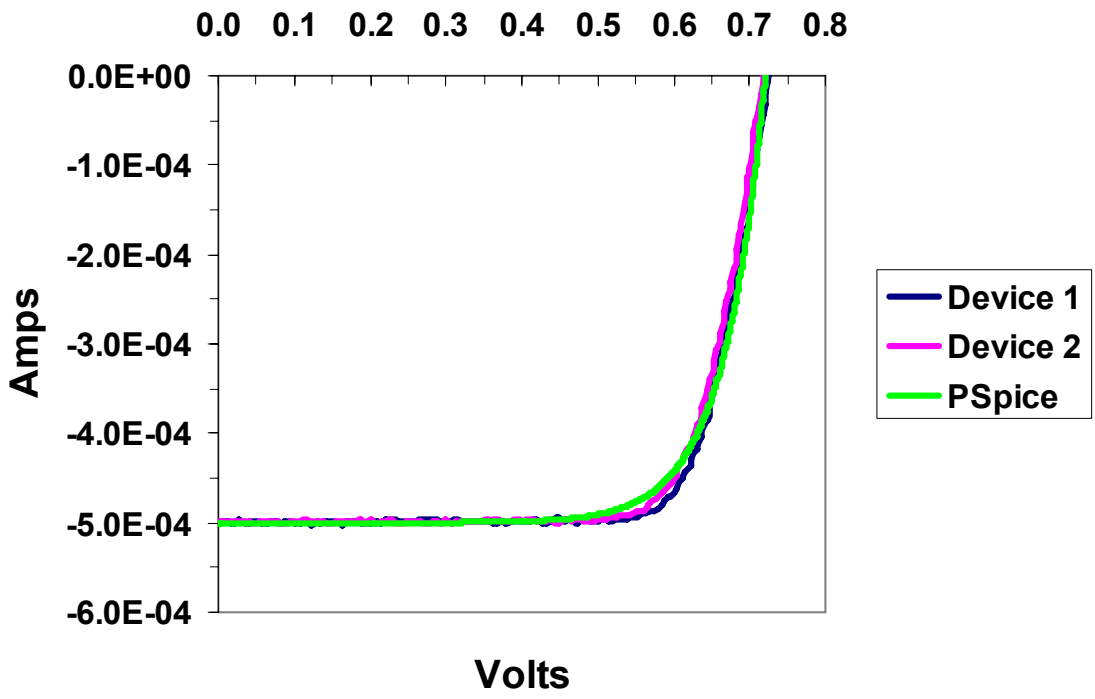

Figure 32. Plot comparing the 500 µA illuminated I-V curves of the test data and the PSpice model.

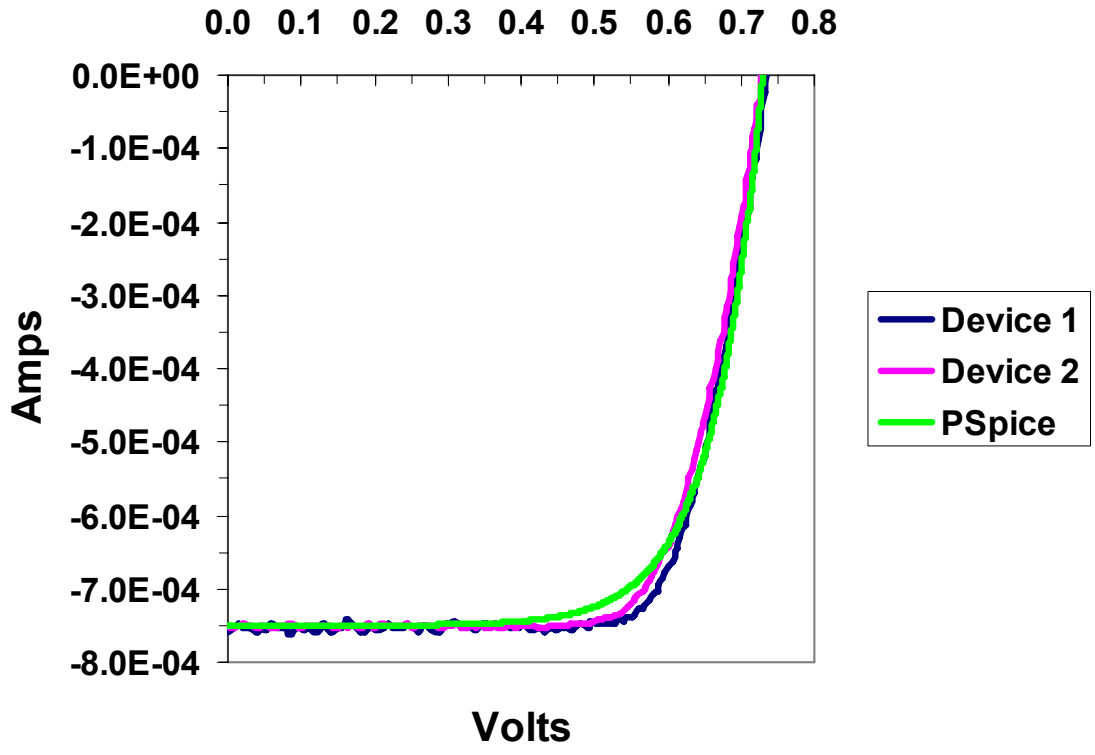

Figure 33. Plot comparing the 750 µA illuminated I-V curves of the test data and the PSpice model.

Three different scenarios are simulated. Illumination is held constant for one of the photocells such that 750 µA is generated while the illumination on the other photocell is varied such that 750 µA, 500 µA and 0 A are generated. These simulations are then compared against the test data. As expected, test results and modeling show I_{SC} is limited by the cell that is generating the least amount of current. The PSpice schematic is shown in Figure 34 and the test and simulation results are shown in Figures 35-37.

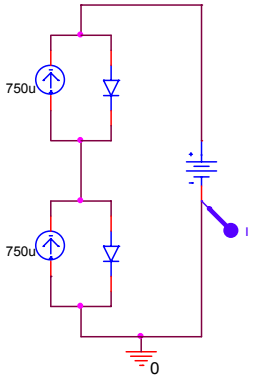

Figure 34. PSpice schematic of series connected photocells.

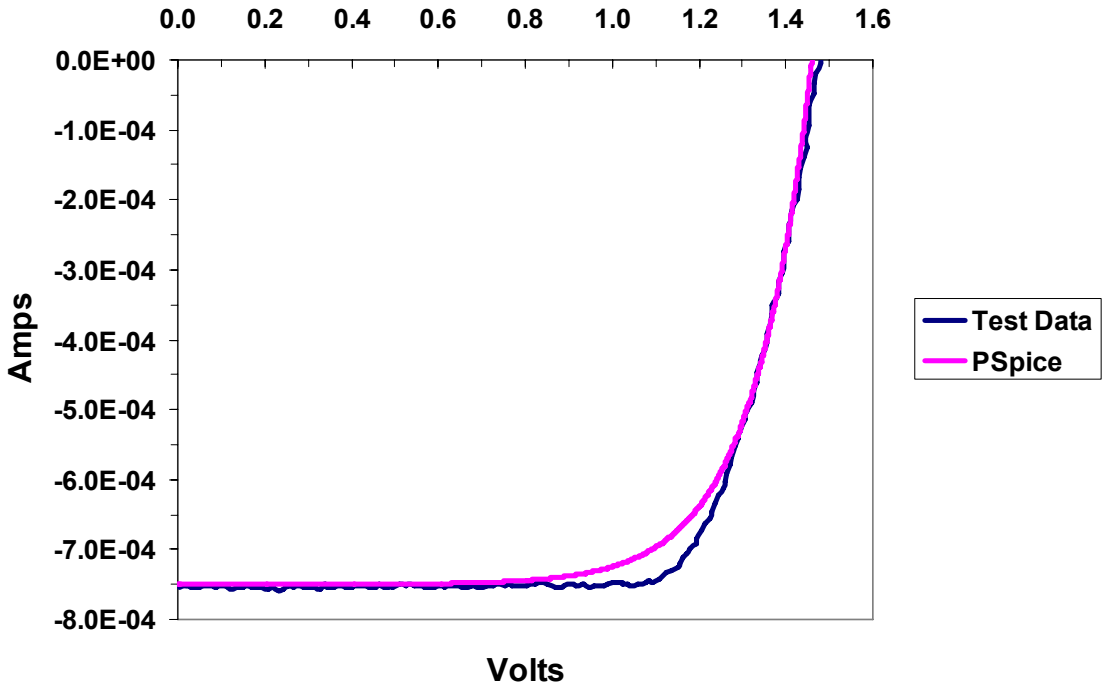

Figure 35. Plot comparing the test data and PSpice model for the case where both photocells are illuminated such that each device is generating 750 µA.I_{SC}.

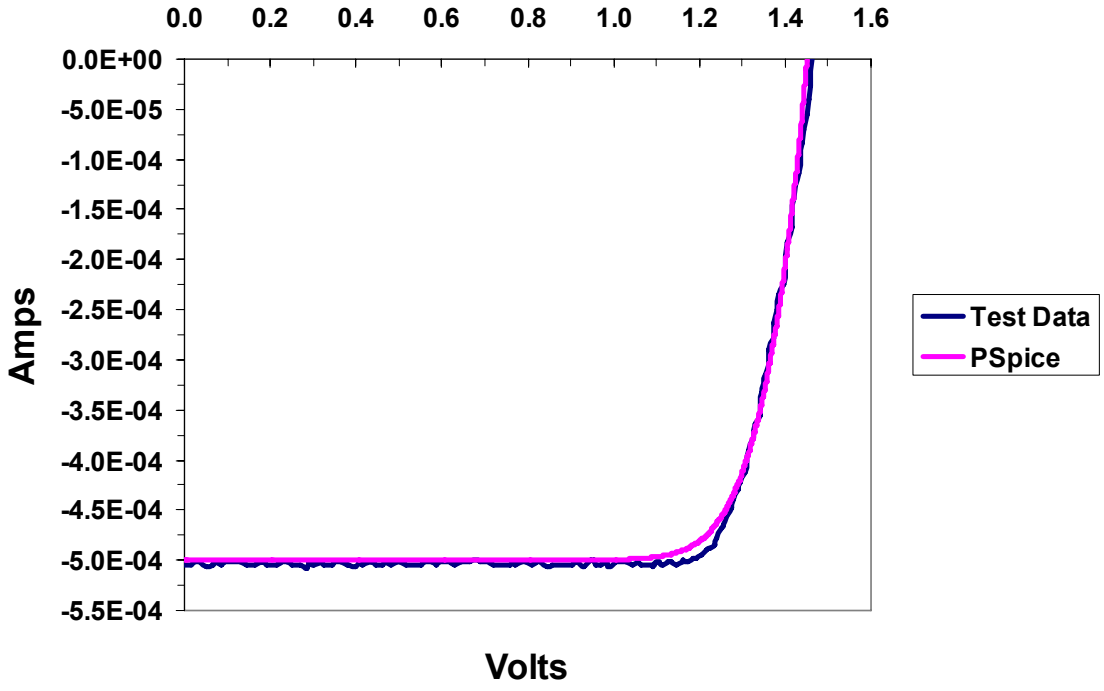

Figure 36. Plot comparing the test data and PSpice model for the case where the two photocells are illuminated such that one is generating 750 µA I_{SC} and the other is generating 500 µA.I_{SC}.

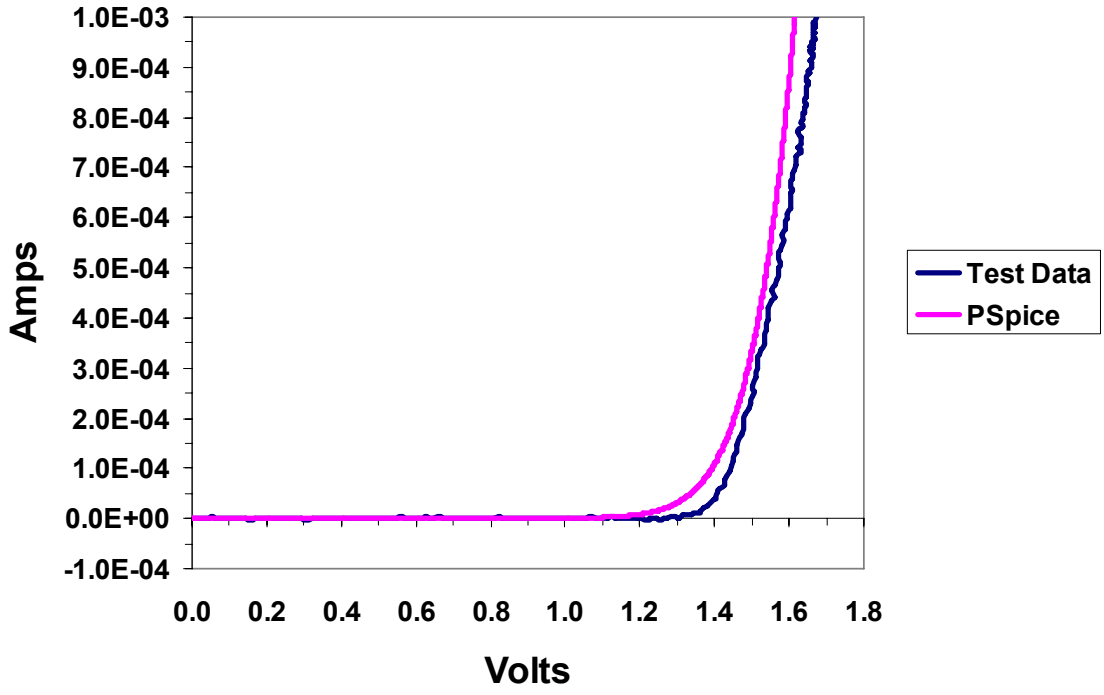

Figure 37. Plot comparing the test data and PSpice model for the case where one photocell is illuminated such that one is generating 750 µA I_{SC} and the other photocell is unilluminated.

Referring to Tables 2 – 4 we see that the values of V_{OC}, I_{SC}, and P_{max} from the test data and the PSpice simulation results are within a few percent of each other. These results show that PSpice can be used to model the effects of non-uniform illumination on the performance of series connected photovoltaic arrays.

Table 2. This table compares the performance parameters of the actual device and the PSpice model under the conditions where both devices were generating 750 μA I_{SC}.

	Test Data	Pspice Model	Difference	% Difference
V_{oc} (V)	1.48	1.46	0.02	1.35
I_{sc} (μA)	754	750	4	0.53
P_{max} (μW)	835	774	61	7.31

Table 3. This table compares the performance parameters of the actual device and the PSpice model under the conditions where one device was generating 750 μA I_{SC} and the other 500 μA.

	Test Data	Pspice Model	Difference	% Difference
V_{oc} (V)	1.47	1.45	0.02	1.36
I_{sc} (μA)	504	500	4	0.79
P_{max} (μW)	598	580	18	3.01

Table 4. This table compares the performance parameters of the actual device and the PSpice model under the conditions where one device was generating 750 μA I_{SC} and the other 0A.

	Test Data	Pspice Model	Difference	% Difference
V_{oc} (V)	1.68	1.62	0.06	3.57
I_{sc} (μA)	0	0	0	0.00
P_{max} (μW)	0	0	0	0.00

3.3 Summary

Two modeling techniques were presented in this Chapter. For the first technique it was shown that an SCPA can be modeled as a lumped element using a PSpice analog behavioral model. The lumped element model is useful in decreasing simulation times

and improving convergence. This model was based on a curve fit to device performance data using Eq. (33), which describes the SCPA performance to first order. Slight discrepancies between the test data and the model are attributed to series resistance and slightly non-uniform illumination. Nevertheless, the model is quite accurate with an RMS error of only a few percent.

The second technique involves individually modeling the series connected photocells and is useful for simulating the effects of non-uniform illumination. Data based models of two photocells were developed for various levels of illumination. The individual photocell models were placed in series and PSpice simulations were performed under various levels of uniform and non-uniform illumination showing the current limiting effect of the least illuminated photocell. Simulation results compared well to the test data with the error being only a few percent.

4 Illumination of SCPAs by a Gaussian Beam

In this Chapter the effects of Gaussian illumination on the I_{SC} of an SCPA are addressed. We consider an SCPA that consists of individual rectangular photocells connected in series and arranged in a circular fashion. The beam radius of the Gaussian intensity profile profile with respect to the SCPA radius determines the loss in I_{SC} due to non-uniform illumination. Illumination efficiency, η_I, is defined as loss in I_{SC} due non-uniform illumination with $\eta_I = 1$ being the case of uniform illumination. Theory is derived giving the optimum Gaussian beam radius for a given SCPA radius and the theory is then illustrated experimentally [1].

4.1 Theory

When a Gaussian beam is used to illuminate an SCPA, the I_{SC} is determined by the optical intensity incident upon the cells along the circumference of the array. A Gaussian beam radius ($1/e^2$) that is smaller than the SCPA radius (under filled) results in cells along the circumference being weakly illuminated thereby limiting I_{SC} (Figure 38a). A beam radius that is larger than the radius of the SCPA (over filled) provides a more uniform illumination profile across the SCPA (Figure 38b). Although the profile is more uniform, there is loss due to light being incident outside of the radius of the SCPA. In this section an optimum Gaussian beam radius for a given SCPA radius is derived.

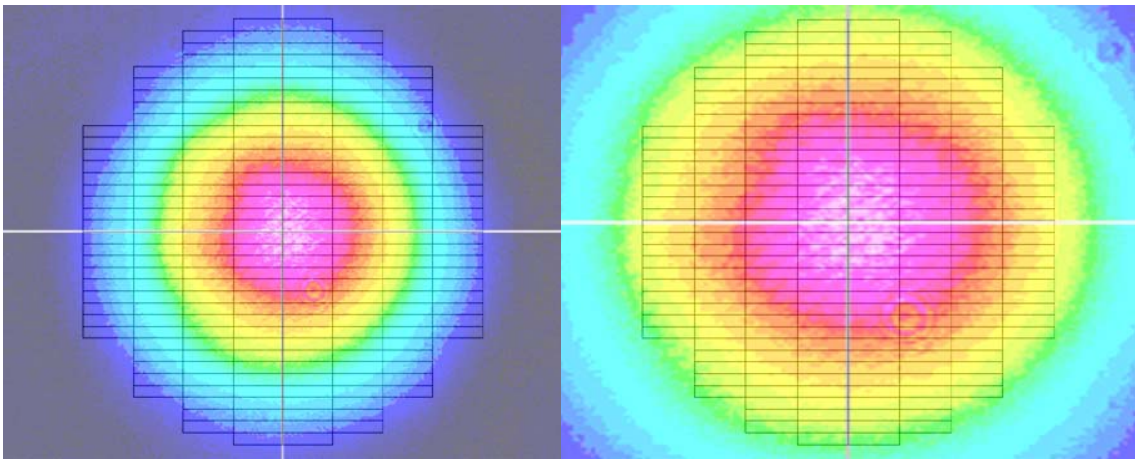

Figures 38a (left) and 38b (right). Figure on the left is a depiction of an under filled condition and the figure on the right is depiction of an overfilled condition for the case of a 4.4 mm diameter SCPA.

To begin, the equations used to derive the optimum Gaussian beam radius are defined. First let's define the area of the entire SCPA, A, as

$$A = \pi r^2, \tag{45}$$

where r is the radius of the SCPA (Figure 39).

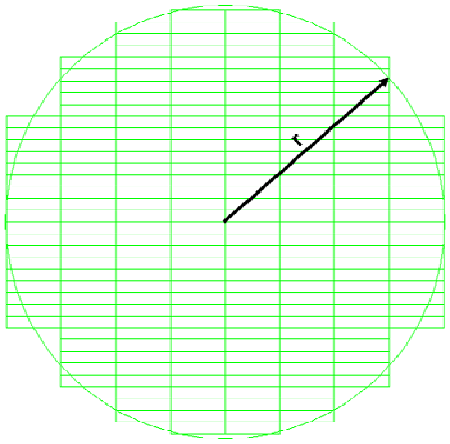

Figure 39. Schematic of an SCPA.

The area of an individual photocell is defined as

$$A_P = \frac{\pi r^2}{N}, \tag{46}$$

where N is the number of photocells. In the case of Gaussian illumination we have an intensity profile that is described by

$$I_P = I_{P0} e^{-\frac{2r^2}{w^2}}, \tag{47}$$

where I_{P0} is the peak intensity, which is located at the center of the beam, and w is the Gaussian beam radius. The Gaussian beam radius, w, is defined as the point at which the intensity has decreased to $1/e^2$ or 0.135 of the peak intensity, I_{P0} [12]. I_{P0} is defined as

$$I_{P0} = \frac{2P_{total}}{\pi w^2}, \tag{48}$$

where P_{total} is the total optical power.

Referring back to Eq. (44) the photo-generated current is defined by

$$I_L = \mathscr{R} A_P I_P, \tag{49}$$

where $\mathscr{R}$ is the wavelength dependent responsitivity (A/W) and I_p is the illumination intensity incident upon the photocell (W/cm^2). Using Eqs. (45) – (49) the photo-generated current now becomes

$$I_L = \mathscr{R} \frac{2P_{total}}{\pi w^2} e^{-\frac{2r^2}{w^2}} \frac{\pi r^2}{N}. \tag{50}$$

The value of w at which I_L is at a maximum for a given r is found by first differentiating Eq. (48) with respect to w and setting the result equal to zero. The derivative of I_L with respect to w is,

$$\frac{\partial I_L}{\partial w} = \mathscr{R} \frac{2P_{total}}{\pi w^2} \frac{\pi r^2}{N} e^{-\frac{2r^2}{w^2}} \frac{4r^2}{w^3} - \mathscr{R} \frac{4P_{total}}{\pi w^3} \frac{\pi r^2}{N} e^{-\frac{2r^2}{w^2}} = 0. \tag{51}$$

Factoring Eq. (49) gives,

$$\frac{\partial I_L}{\partial w} = 4\mathscr{R} \frac{P_{total}}{\pi w^3} \frac{\pi r^2}{N} e^{-\frac{2r^2}{w^2}} \left(\frac{2r^2}{w^2} - 1 \right) = 0. \tag{52}$$

After further simplification,

$$\frac{2r^2}{w^2} = 1, \tag{53}$$

and solving for w gives the result for the optimum beam radius,

$$w_{opt} = \sqrt{2}r\,. \tag{54}$$

Eq. (54) states that the maximum short circuit current from the SCPA is achieved with a Gaussian beam radius that is a **factor of $\sqrt{2}$ larger than the SCPA radius**. This result is illustrated in the next section in which an SCPA is characterized under the illumination of a diverging Gaussian beam.

There are two loss factors associated with Gaussian illumination. First, the cell that is illuminated the least limits I_{SC}. Therefore, illumination intensities above that which are incident along the circumference of the SCPA do not contribute to an increase in I_{SC}. In other words, the SCPA would have the same I_{SC} if it were uniformly illuminated at the same intensity as the Gaussian intensity along the circumference. Second, there is also a loss factor due to a portion of the light that incident outside of the SCPA. Based on these two loss factors, the power in the Gaussian profile that contributes to the generation of SCPA current, $P_{\text{effective}}$, is the product of the illumination intensity (W/cm^2) at the circumference of the SCPA and the area of the SCPA (cm^2). Using Eqs. (45) and (47) - (48) we have

$$P_{effective} = AI_p(r) = r^2 \frac{2P_{total}}{w^2} e^{-\frac{2r^2}{w^2}}. \tag{55}$$

The illumination efficiency, η_I, is the ratio of $P_{\text{effective}}/P_{\text{total}}$,

$$\eta_I = \frac{P_{effective}}{P_{total}} = r^2 \frac{2}{w^2} e^{-\frac{2r^2}{w^2}}, \tag{56}$$

and at w_{opt} the illumination efficiency is,

$$\eta_I(w_{opt}) = \frac{2r^2}{\left(\sqrt{2}r\right)^2} e^{-\frac{2r^2}{\left(\sqrt{2}r\right)^2}} = e^{-1} = 0.368. \tag{57}$$

Gaussian illumination is **at best 36.8% efficient** when compared to a uniform beam. Losses in I_{SC} are even higher for a beam radius other than that defined in Eq. (54).

4.2 Experimental Results

Theory presented in the previous section is illustrated by performing an experiment. The theory states that there is an optimum beam width with which to illuminate the SCPA that will maximize I_{SC}. In order to illustrate this theory an SCPA is illuminated with a diverging single-mode beam. The beam width is increased by increasing the distance between the SCPA and the optical source. I_{SC} is measured for various beam widths, normalized with respect to the maximum and then compared to the theory.

To begin, the single mode source used was a Nd:YAG laser manufactured by CrystaLaser. The laser has an operating wavelength of 1064 nm, output power of 500 mW CW, and a beam diameter of 0.45 mm with a 3.6 mrad full angle beam divergence. This laser was fixed mounted and aligned such that the beam passed through the center of two apertures. These apertures having the same height were mounted at opposite ends of an optic rail and defined the optical axis. The optic rail provided an easy method for varying the distance of optical components from the laser while maintaining rough alignment to the optical axis.

Once the optical axis was defined, a 23 mm focal length convex lens was placed in front of the laser to expand the laser beam as the beam traveled along the optical axis. The beam diameter was calculated at distances from the lens of 14 to 62 cm in 2 cm increments. This was done by first measuring the power output from the laser. Then the power was measured through a 3 or 5 mm aperture at the various points along the optical axis. Using the equation that defines the power in a radius for a Gaussian beam [12],

$$P_{optical}(r) = P_{total}\left(1 - e^{-\frac{2r^2}{w^2}}\right), \tag{58}$$

and solving for w,

$$w = \sqrt{\frac{-2r^2}{\ln\left(1 - \frac{P_{optical}(r)}{P_{total}}\right)}}, \tag{59}$$

we can now calculate the Gaussian beam radius by measuring the power through a known diameter aperture. The beam divergence characterization results are shown in Table 5 and Figure 40 and a schematic of the setup is shown in Figure 41.

Table 5. Beam divergence characterization results

r (mm)	Ptotal (mW)	distance (cm)	P(r) (mW)	w (mm)
3	447	14	384	3.030903
3	447	16	346	3.478699
5	447	18	433	3.799508
5	447	20	422	4.164005
5	447	22	406	4.574864
5	447	24	389	4.948173
5	447	26	367	5.390805
5	447	28	347	5.778535
5	447	30	325	6.205228
5	447	32	304	6.623493
5	447	34	283	7.061569
5	447	36	264	7.482413
5	447	38	244	7.958835
5	447	40	228	8.371283
5	447	42	213	8.789277
5	447	44	201	9.149877
5	447	46	187	9.605825
5	447	48	174	10.06986
5	447	50	163	10.49919
5	447	52	152	10.96872
5	447	54	143	11.38821
5	447	56	135	11.7924
5	447	58	128	12.174
5	447	60	121	12.58561
5	447	62	114	13.03179

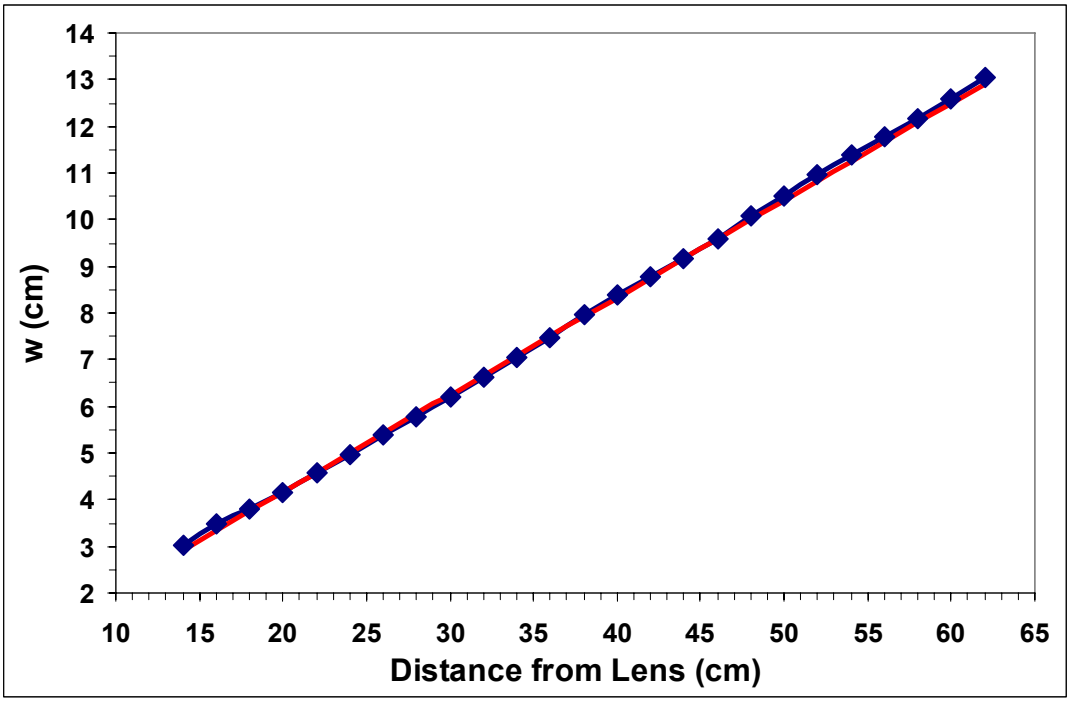

Figure 40. Plot of *w* as a function of distance from the lens. The blue trace represents the test data and the red trace is a linear fit to that data.

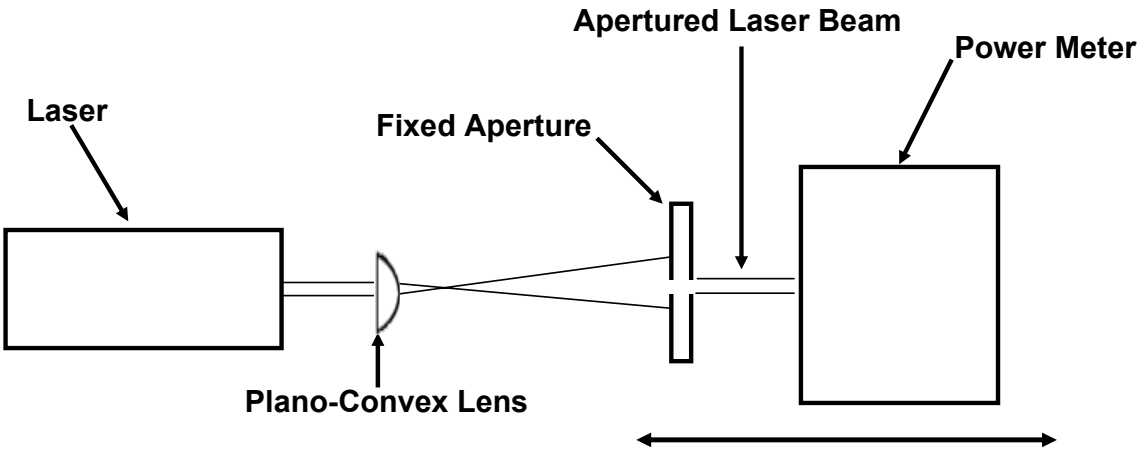

Figure 41. Schematic of test setup used to characterize the laser beam radius along the optical axis.

An image of the laser beam was taken using a WinCamD beam profiling camera. The laser beam is of good quality and the screen shot from the WinCamD software depicting the beam image is shown below in Figure 42. Referring to Figure 42, the laser beam has an ellipticity of 0.96, a Gaussian fit of 94% along one axis and a Gaussian fit of 96.1% along the other.

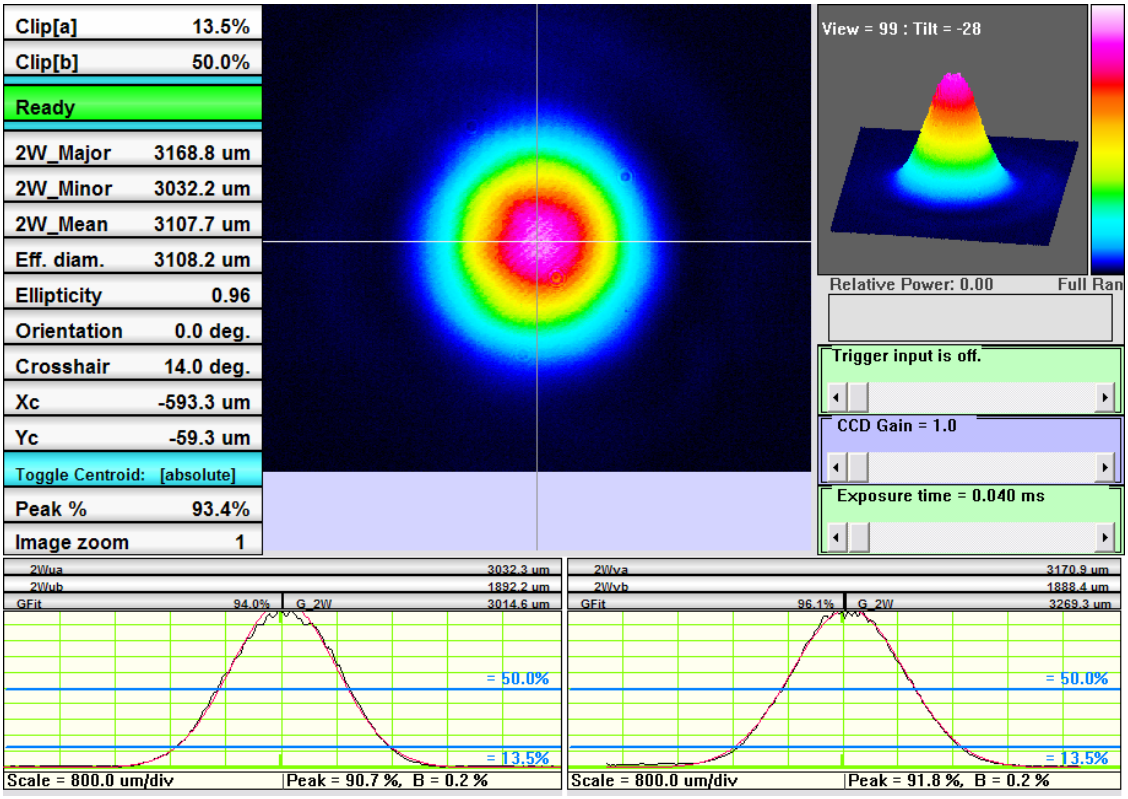

Figure 42. Screenshot of WinCamD software showing the laser beam profile.

Now that the beam divergence and profile have been characterized along the optical axis an SCPA is inserted in place of the aperture that was used to measure the beam diameter. The SCPA was mounted on an XYZ stage to allow for fine tuning of the alignment. A Tektronix 370b curve tracer was connected to measure I_{SC}. At each distance along the optical axis the SCPA alignment was fine tuned by adjusting the XYZ stage until maximum I_{SC} was achieved. When the alignment was optimum, the value of I_{SC} was recorded. I_{SC} data was taken at distances from 14 cm to 62 cm in increments of 2 cm, corresponding to the aperture measurements that were taken. Figure 43 is a schematic for the test setup and Figure 44 is a photograph.

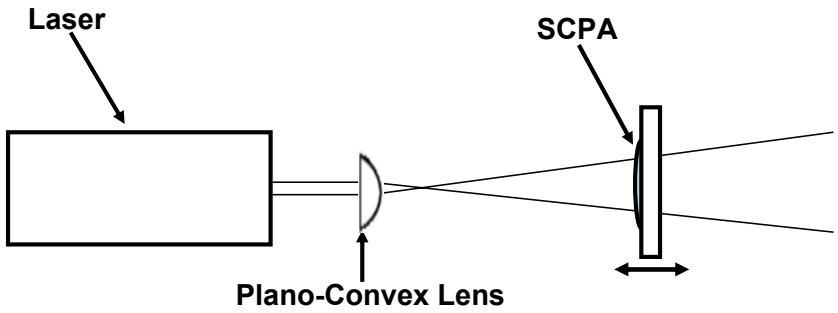

Figure 43. Schematic of test setup.

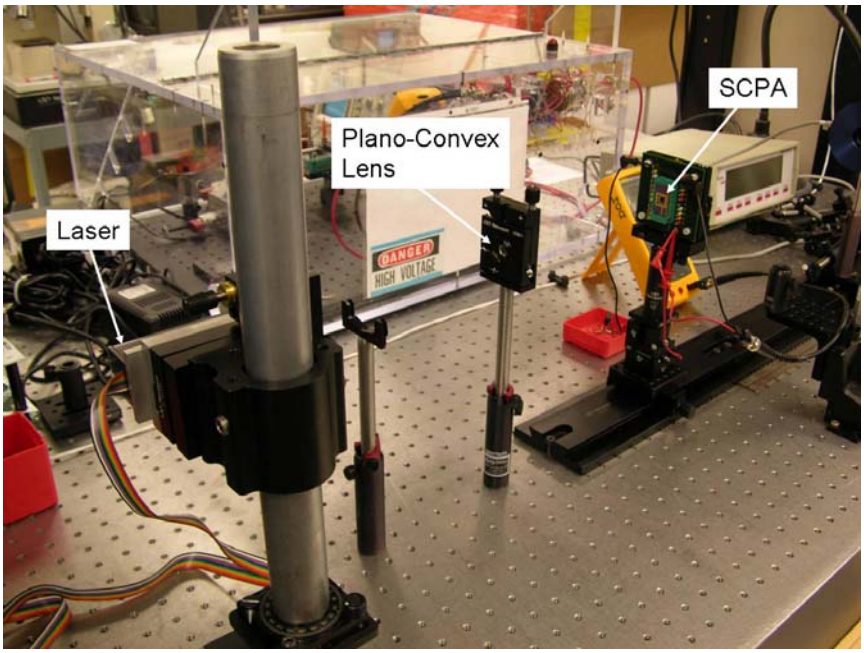

Figure 44. Single-mode experimental setup.

The SCPA used in this experiment consists of 230 cells each 120 x 550 μm in dimension. These cells are arranged in a circular fashion with a radius of 2.2 mm as shown in Figure 45. Based on the theory developed in the previous section, Eq. (54) can be used to calculate the optimum beam radius. Eq. (54) gives w_{opt} = 3.11 mm for the SCPA used in this experiment. A plot of the normalized I_{SC} versus w (Figure 46) for both the theoretical and test data shows excellent agreement and that indeed the maximum I_{SC} occurs at w = 3.11 mm. It should be noted that as the beam radius decreases from the optimum there is a rapid decease in I_{SC} relative to beam radii that are larger than the SCPA. This shows that current limiting is a stronger loss factor than the loss due to light being incident outside of the array.

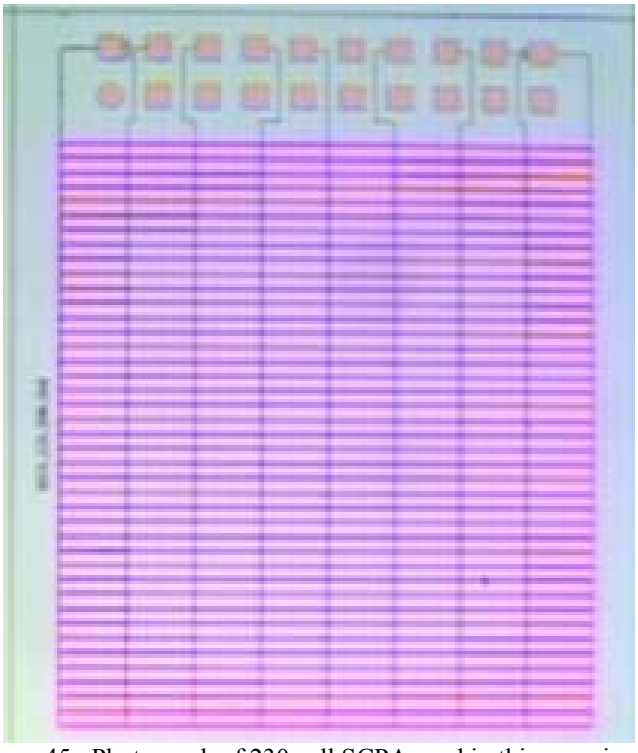

Figure 45. Photograph of 230 cell SCPA used in this experiment.

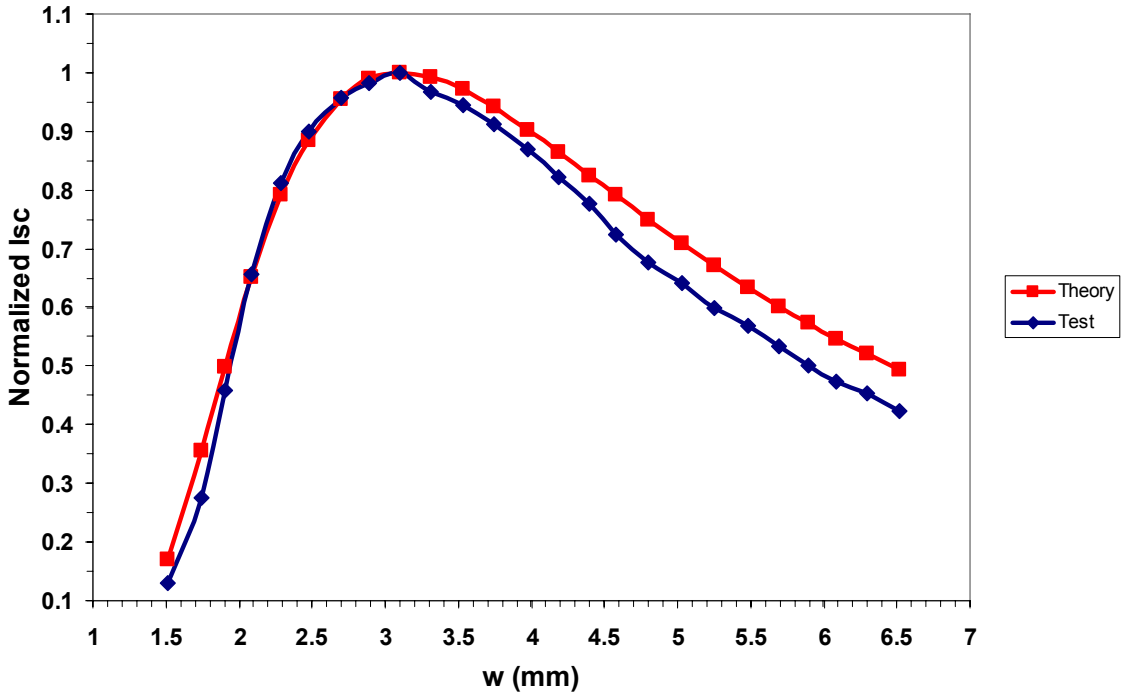

Figure 46. Plot of normalized I_{SC} as a function of laser beam radius. The red trace represents the theory and the blue trace shows the test results.

The slight discrepancy between the theory and test data is attributed to the SCPA geometry, which is not perfectly circular, and the beam profile of the laser used in this experiment is not an ideal Gaussian (See Figures 42 and 45).

4.3 SCPAs with Wedge Shaped Cells

SCPAs with individual cell geometries that are wedge shaped have been designed by both Sandia National Laboratories and JDSU. This geometry, under Gaussian illumination, will approximately perform as if the illumination were uniform (Figure 47) provided that the SCPA is sufficiently larger that the laser beam. The reason for this is that the radial variations of the Gaussian profile are averaged because the cells extend radially from the center of the SCPA. Integrating the Gaussian intensity profile, given by Eqs. (47) - (48), over the area of a single cell (Figure 47) yields the incident power,

$$P_{cell} = \int_0^{\frac{2\pi}{N}} \int_0^{r} \frac{2P_{total}}{\pi w^2} e^{\frac{-2r^2}{w^2}} r dr d\theta = \frac{1}{N} P_{total} \left(1 - e^{\frac{-2r^2}{w^2}} \right), \tag{60}$$

where r_{SCPA} is the radius of the SCPA, and N is the number of cells. We can easily see that Eq. (60) gives the same result for each cell within the array. The exponential term accounts for any power loss due to light that is incident outside of the SCPA. Note that Eq. (60) does not take into account misalignment which will further reduce the illumination efficiency.

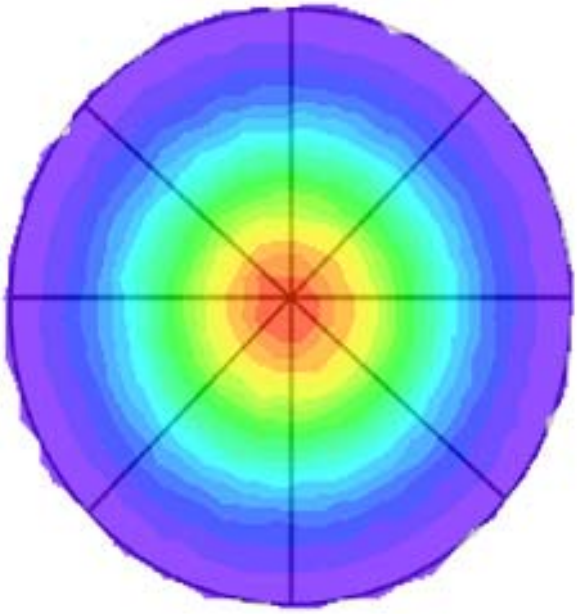

Figure 47. Illustration showing a Gaussian beam incident upon an SCPA with wedge shaped cells.

4.4 Summary

In summary, it was shown that there are two loss mechanisms when a SCPA of circular geometry is illuminated with a single-mode laser beam. First, there is loss from the current limiting effect due to the lower intensity incident along the circumference of the SCPA and secondly there is loss through power that is incident outside the active area of the SCPA (Figure 38). These conditions were then used to derive an equation for the

optimum Gaussian beam radius in order to maximize the short-circuit current, I_{SC}. This resulted in an optimum beam-SCPA radius ratio of $\sqrt{2}$ (Eq. (54)). Also, an equation was derived that calculated the optical efficiency, η_I, and it was shown that the best case optical efficiency is 36.8% (Eq. (57)).

These results were illustrated experimentally by illuminating an SCPA with a single-mode Nd:YAG laser. The test setup consisted of first defining the optical axis by aligning the laser beam through apertures of the same height at opposite ends of an optics rail. Different beam radii were created by inserting a plano-convex lens in front of the laser to diverge the beam as it propagated along the optical axis. The beam divergence along the optical axis was verified by measuring the power through fixed apertures and then calculating the beam radius using Eq. (59). Beam quality was also measured using a beam profiling camera. Once the experimental setup was characterized an SCPA was placed along the optical axis and its performance under increasing beam widths was measured by increasing the distance between the SCPA and the laser. Test results are in good agreement with the theory as shown in Figure 46. Slight deviations between the test data and theory are due to a less than perfect circular SCPA geometry and non-ideal Gaussian illumination. Also, theory for the Gaussian illumination efficiency of an SCPA with wedge shaped cells was given.

5 Multi-Mode Illumination of SCPAs

In this chapter the effects of coherent multi-mode optical fiber illumination on the I_{SC} of an SCPA are addressed. Coherent multi-mode illumination has a speckled intensity pattern. These speckles contain regions of lower intensity that cause some of the photocells within the array to be under illuminated. As discussed previously the weakest illuminated photocell within the SCPA limits the current through the entire array. As the ratio of the cell area to the speckle correlation area decreases, so does the optical efficiency. In fact, if the ratio is small enough, a cell can be completely dark. This would result in an $I_{SC} = 0$ and would be the case regardless of the incident optical power. Figure 48 illustrates a speckled intensity profile incident upon an SCPA.

Ultimately the goal is to determine the speckle correlation area as a function of fiber diameter, wavelength, and distance. The mean speckle correlation area is calculated by integrating the normalized mutual intensity function, μ, of the light incident at the SCPA. One can find the mutual intensity, J, through the use of the van Cittert-Zernike theory which describes the propagation of J from a source.

Theory covered in this Chapter begins with a discussion of speckle statistics. Basic properties of step-index multi-mode fibers and how speckle theory applies is presented next. It is then shown that the illumination efficiency of an SCPA can be determined by applying the theory of integrated speckle and this theory is illustrated by an experiment. A discussion on applications and design considerations are covered next and the Chapter is concluded with a summary of the results.

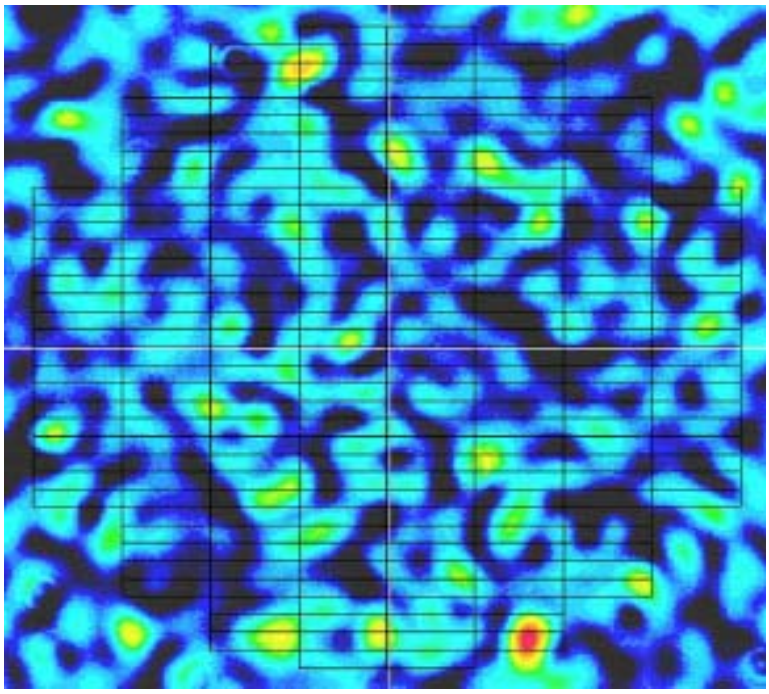

Figure 48. Speckled intensity pattern overlaid upon a schematic drawing of an SCPA.

5.1 Speckle

Speckle statistics are covered in great depth by [13] – [15]. The theory in Goodman's books is presented in the case of free space propagation of coherent light reflected off of a rough scattering surface. This theory is summarized here and then modified for the case in which we have a source represented by a multi-mode fiber instead of a rough scattering surface.

5.1.1 General Description of Speckle

A speckle pattern can be described as a random intensity distribution. This random intensity distribution is the result of the interference of coherent waves. Speckle is observed when the optical path lengths traveled by coherent light waves differ significantly on the scale of a wavelength. Such situations, for example, are encountered

when a coherent laser beam is reflected off of a rough surface or in the case of propagation in a multimode fiber.

In Goodman's most recent book [13] the cause of speckle at a point in space is described intuitively as the sum of many phasor contributions that produce a resultant with a relatively large or small sum. The value of the sum depends on whether or not the interference is predominately constructive or destructive, respectively. This phenomenon has been termed "random walk" and is illustrated in Figure 49.

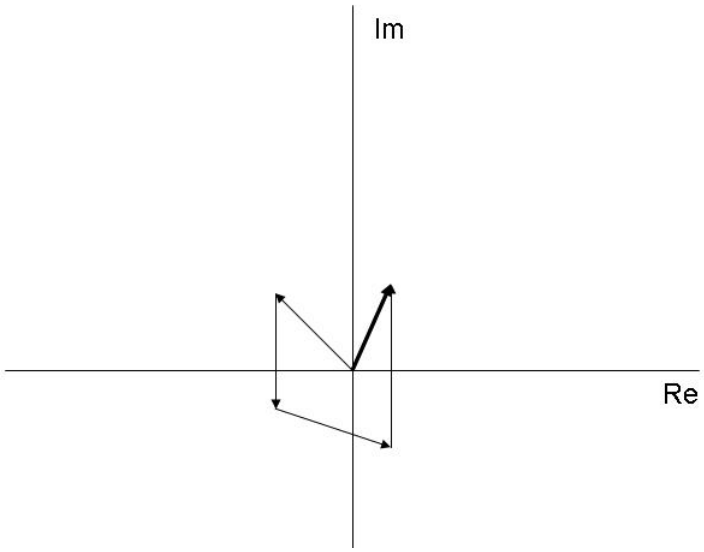

Figure 49. Illustration of random walk resulting in constructive interference.

5.1.2 Some Statistical Properties of Speckle

Autocorrelation functions are used to describe the coherence of optical waves and are of great importance in speckle theory. Consider the case in which light is incident upon a rough scattering surface and we want to know the mean speckle correlation area at an observation plane at distance *z* (Figure 50). The mean speckle correlation area can be calculated by taking the autocorrelation of the intensity distribution in the *(x, y)* plane,

$$R_I(x_1, y_1; x_2, y_2) = \langle I(x_1, y_1) I(x_2, y_2) \rangle, \tag{61}$$

where <..> denotes an ensemble average. The width of the "spike" in this autocorrelation function can then be related to the mean speckle correlation area and is discussed later.

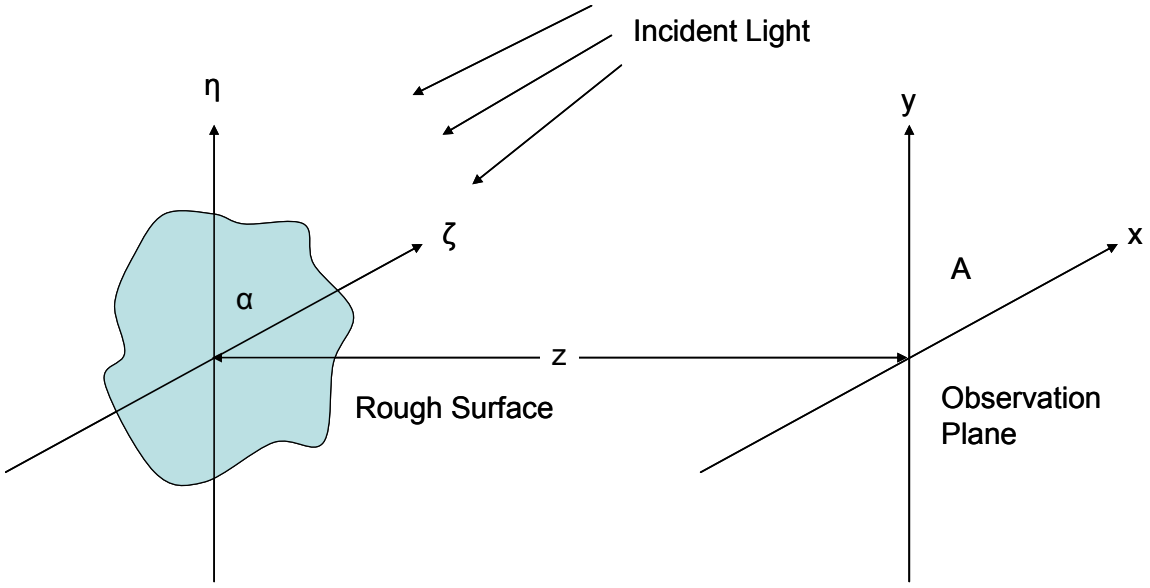

Figure 50. Geometry of free space speckle propagation.

To calculate the autocorrelation of the intensity pattern, *I(x, y)*, we take into account that the complex field, *A(x, y)*, obeys circular complex Gaussian statistics [13] – [15]. In such a case the autocorrelation function of the intensity is given in terms of the autocorrelation function of the fields by the relation

$$R_I(x_1, y_1; x_2, y_2) = \langle I(x_1, y_1) \rangle \langle I(x_2, y_2) \rangle + |J_A(x_1, y_1; x_2, y_2)|^2, \tag{62}$$

where J_A is referred to as the mutual intensity of the fields in the observation plane

$$J_A(x_1, y_1; x_2, y_2) = \langle A(x_1, y_1) A^*(x_2, y_2) \rangle, \tag{63}$$

and

$$J_A(x, y; x, y) = \langle I(x, y) \rangle. \tag{64}$$

Calculating R_I has now been reduced to calculating the mutual intensity of the fields, J_A.

Using the van Cittert-Zernike theorem we can describe the propagation of the mutual intensity of source, J_α, to an observation plane. Assuming that the source area is much larger than the speckle correlation area and that variations in the source intensity distribution are coarse the mutual intensity of the source can be approximated by [15],

$$J_\alpha\left(\xi_1,\eta_1;\xi_2,\eta_2\right)=I\left(\bar{\xi},\bar{\eta}\right)\mu_\alpha\left(\Delta\xi,\Delta\eta\right) \tag{65}$$

and,

$$\Delta\xi=\xi_1-\xi_2\,,\qquad \bar{\xi}=\frac{\xi_1+\xi_2}{2}$$

$$\Delta\eta=\eta_1-\eta_2\,,\qquad \bar{\eta}=\frac{\eta_1+\eta_2}{2}\,. \tag{66}$$

The generalized form of the van Cittert-Zernike theorem is [15]

$$J_A\left(x_1,y_1;x_2,y_2\right)=\frac{\kappa\left(\bar{x},\bar{y}\right)e^{-j\psi}}{\left(\lambda z\right)^2}\int_{-\infty}^{\infty}\int_{-\infty}^{\infty}I\left(\bar{\xi},\bar{\eta}\right)e^{\frac{j2\pi}{\lambda z}\left(\Delta x\bar{\xi}+\Delta y\bar{\eta}\right)}d\bar{\xi}\,d\bar{\eta}\,, \tag{67}$$

where

$$\kappa\left(\bar{x},\bar{y}\right)=\int_{-\infty}^{\infty}\int_{-\infty}^{\infty}\mu_\alpha\left(\Delta\xi,\Delta\eta\right)e^{\frac{j2\pi}{\lambda z}\left(\bar{x}\Delta\xi+\bar{y}\Delta\eta\right)}d\Delta\xi\,d\Delta\eta\,, \tag{68}$$

and

$$\Delta x=x_1-x_2\,,\qquad \bar{x}=\frac{x_1+x_2}{2}$$

$$\Delta y=y_1-y_2\,,\qquad \bar{y}=\frac{y_1+y_2}{2}\,. \tag{69}$$

It should be noted that the approximations used in this form of the equation only holds under the following requirement

$$z>2\frac{Dd_c}{\lambda}\,. \tag{70}$$

where D is the maximum linear dimension of the source and d_c is the maximum dimension of the source coherence area. This requirement ensures that the observation distance is greater than the geometric mean of the far field distances for the source and the source coherence area.

Equation (67) can be interpreted as follows. The complex coherence factor at the source, $\mu_\alpha(\Delta\xi,\Delta\eta)$, determines the average intensity in the observation plane, $I(\bar{x},\bar{y})$, and the average intensity at the source, $I(\bar{\xi},\bar{\eta})$, determines the complex coherence factor in the observation plane, $\mu_A(\Delta x,\Delta y)$. This is a result of the reciprocal width relationship of Fourier transform pairs (Figure 51).

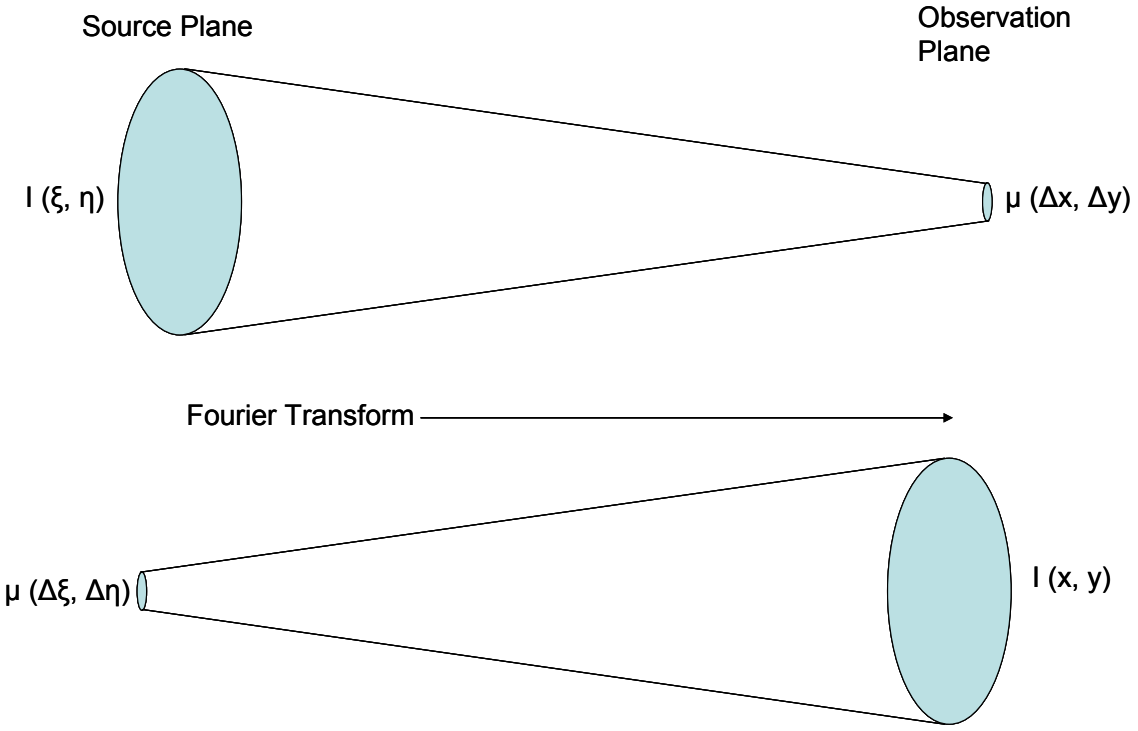

Figure 51. Illustration of the reciprocal width relation of Fourier transform pairs.

For the purposes of calculating the mean speckle correlation area it will be convenient to normalize the mutual intensity,

$$\mu_A(x_1, y_1; x_2, y_2) = \frac{J_A(x_1, y_1; x_2, y_2)}{\left[J_A(x_1, y_1; x_1, y_1) J_A(x_2, y_2; x_2, y_2)\right]^{\frac{1}{2}}}. \tag{71}$$

This normalized form of the mutual intensity is commonly referred to as the complex coherence factor. Calculating the mean speckle correlation area, A_c, is now just a matter of integrating $|\mu|^2$,

$$A_c = \int_{-\infty}^{\infty} \int_{-\infty}^{\infty} \left|\mu_A(\Delta x, \Delta y)\right|^2 d\Delta x d\Delta y. \tag{72}$$

5.1.3 Speckle in Step-Index Multi-Mode Fibers

In this Section some basic properties of step-index multi-mode fibers are discussed and these properties are then applied to the speckle covered in the previous Section. Speckle occurs within an optical fiber when a coherent source is used. There are two methods that can be used to describe the underlying cause of speckle in this case. One method is to consider the geometry in Figure 52. Rays enter the fiber at different angles, θ, and therefore will travel different distances to reach the end face of the fiber. Differences in the index of refraction in the core and cladding region determine the maximum angle of incidence at which the ray will remain confined within the fiber core and is commonly referred to as the numerical aperture (NA) [16],

$$NA = \sin(\theta_{\max}) = \left(n_1^2 - n_2^2\right)^{\frac{1}{2}}, \tag{73}$$

where n_1 and n_2 are the indices of refraction in the core and cladding respectively. The path length differences result in phase differences between the rays at the end face of the fiber. These phase differences create random constructive and destructive interferences that produce a speckled pattern.

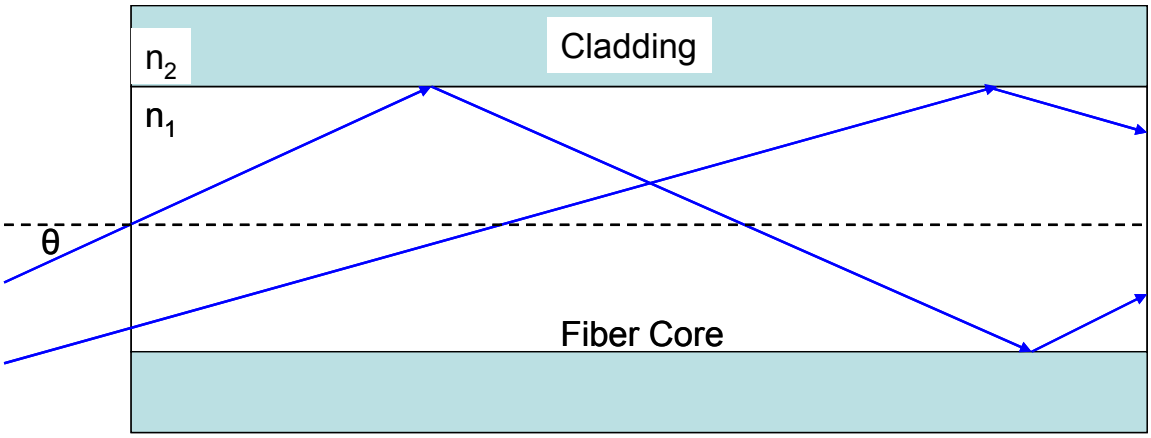

Figure 52. Step-index multi-mode fiber geometry.

A second method is to consider the modal properties of the fiber. The number of modes supported is a function of the wavelength of the light emitted by the source (λ), fiber radius, and the numerical aperture. Calculating the approximate number of modes can be accomplished by first determining the normalized frequency of the fiber, V, which is also referred to as the "V parameter" [16]

$$V = k_0 aNA\,, \tag{74}$$

where k_0 is the free-space wave number ($2\pi/\lambda$) and a is the radius of the fiber core. We can relate the number of modes to V by,

$$M = \frac{V^2}{2}. \tag{75}$$

The speckled pattern at the end-face of the fiber is a result of the superposition of the different mode field patterns. Figure 53 illustrates the first few mode field patterns and Figure 54 shows the speckle pattern at the end of a 400 μm fiber.

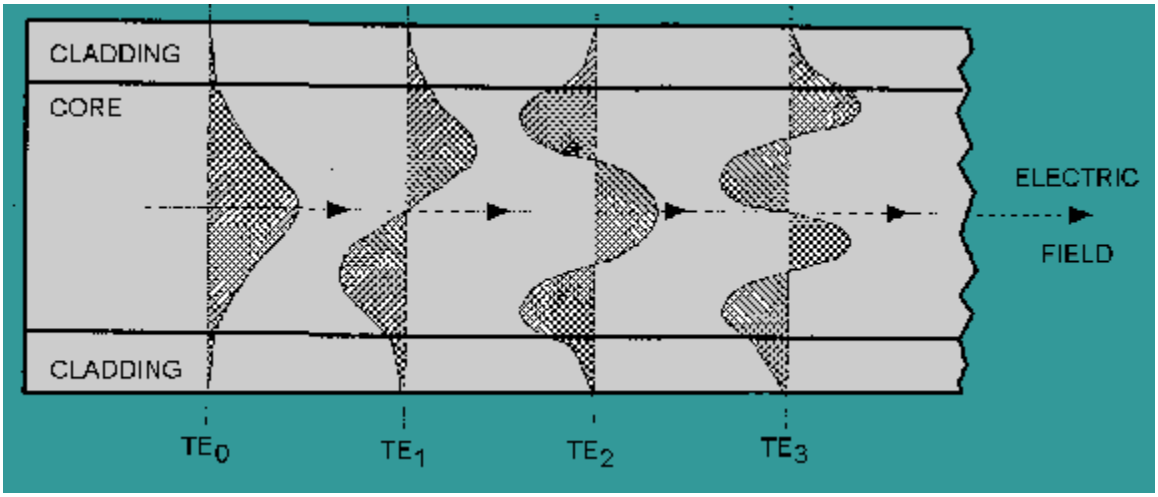

Figure 53. Mode field patterns in an optical fiber [17].

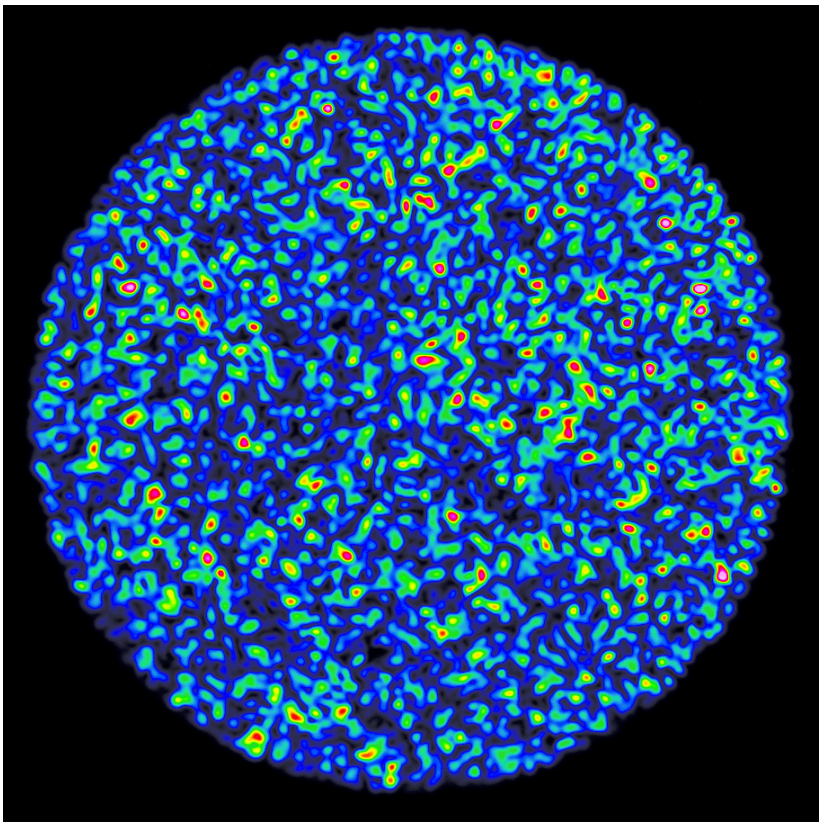

Figure 54. Speckled intensity measured at the end face of a multimode fiber.

One can easily see that the intensity has a uniform envelope that is randomly "dotted with speckle". Referring back to Eq. (65) mutual intensity at the fiber face has the form

$$J_\alpha\left(\xi_1,\xi_2;\eta_1,\eta_2\right)=\left[I\left(\xi_1,\eta_1\right)I\left(\xi_2,\eta_2\right)\right]^{\frac{1}{2}}\mu_\alpha\left(\Delta\xi,\Delta\eta\right). \tag{76}$$

The intensity envelope is described by the circ function

$$I(\xi,\eta)=I_0 circ\left(\frac{\sqrt{\xi^2+\eta^2}}{a}\right). \tag{77}$$

In the literature the complex coherence factor at the end face of a step-index multi-mode fiber is approximated as [18] – [20]

$$\mu_\alpha\left(\Delta\xi,\Delta\eta\right)=2\frac{J_1\left(\frac{2\pi}{\lambda}NA\sqrt{\Delta\xi^2+\Delta\eta^2}\right)}{\frac{2\pi}{\lambda}NA\sqrt{\Delta\xi^2+\Delta\eta^2}}. \tag{78}$$

Recall that the intensity profile is determined by the Fourier transform of the complex coherence factor. Taking the Fourier transform of Eq. (78) results in a circ function. The intensity profile of light propagating from a multi-mode fiber has a roll off and is not accurately described by circ function (Figure 55).

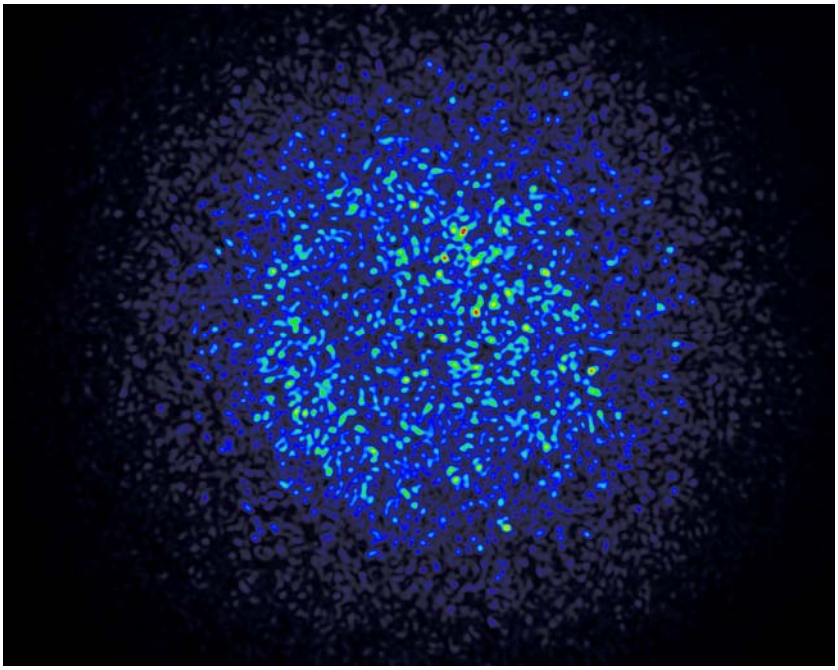

Figure 55. Measured illumination profile after propagating 23 mm from a 400 μm fiber.

The complex coherence factor was derived using geometric approximation while in reality this is a modal phenomenon. Also, the Bessel function is truncated by the fiber core and taking the Fourier transform would result in a roll of in the intensity pattern. Even though Eq. (78) is an approximation it will not have an effect on the calculations of speckle correlation area at an observation plane as the speckle correlation area is determined by the intensity profile at the source.

Speckle in multi-mode optical fibers is also addressed in the literature under a different context termed modal noise and the primary application is in the communications field [20] – [25]. Modal noise is defined as fluctuations in power measured by a receiver. These fluctuations are due to the temporally changing spatial variations in the speckled intensity pattern. Modal noise would occur under the condition where the fiber core is larger than the receiver and/or misaligned such that some of the light is incident outside of the receiver. Modal noise does not directly apply to the case of illuminating an SCPA for a few reasons. In the case of illuminating an SCPA we have several photocells connected in series not just a single element. Also, in these papers the receiver is typically either in intimate with the fiber core or very close to it and they do not address the complex coherence factor at the as it propagates from the fiber surface.

With the knowledge of both the intensity and the complex coherence factor at the end of a fiber we can now calculate the mean speckle correlation area in an observation plane at

a distance z from the fiber by applying the generalized van Cittert-Zernike theorem discussed in the previous section.

Substituting Eqs. (77) and (78) into Eqs. (67) and (68), respectively, we have

$$J_A\left(x_1,y_1;x_2,y_2\right)=\frac{\kappa\left(\bar{x},\bar{y}\right)e^{-j\psi}}{\left(\lambda z\right)^2}\int_{-\infty}^{\infty}\int_{-\infty}^{\infty}I_0 circ\left(\frac{\sqrt{\bar{\xi}^2+\bar{\eta}^2}}{a}\right)e^{\frac{j2\pi}{\lambda z}\left(\Delta x\bar{\xi}+\Delta y\bar{\eta}\right)}d\bar{\xi}\,d\bar{\eta}\,, \tag{79}$$

and

$$\kappa\left(\bar{x},\bar{y}\right)=\int_{-\infty}^{\infty}\int_{-\infty}^{\infty}2\frac{J_1\left(\frac{2\pi}{\lambda}NA\sqrt{\Delta\xi^2+\Delta\eta^2}\right)}{\frac{2\pi}{\lambda}NA\sqrt{\Delta\xi^2+\Delta\eta^2}}e^{\frac{j2\pi}{\lambda z}\left(\bar{x}\Delta\xi+\bar{y}\Delta\eta\right)}d\Delta\xi d\Delta\eta\,. \tag{80}$$

The circ and J_1 functions form the Fourier transform pair

$$circ\left(\frac{\sqrt{\xi^2+\eta^2}}{a}\right)\overset{\Im}{\Leftrightarrow}a^2\frac{J_1\left(2\pi a\sqrt{x^2+y^2}\right)}{a\sqrt{x^2+y^2}}, \tag{81}$$

which, results in

$$J_A\left(x_1,y_1;x_2,y_2\right)=\frac{\kappa\left(\bar{x},\bar{y}\right)e^{-j\psi}}{\left(\lambda z\right)^2}I_0a^2\left(2\frac{J_1\left(\frac{2\pi}{\lambda z}a\sqrt{\Delta x^2+\Delta y^2}\right)}{\frac{2\pi}{\lambda z}a\sqrt{\Delta x^2+\Delta y^2}}\right) \tag{82}$$

where,

$$\kappa\left(\bar{x},\bar{y}\right)=2\frac{1}{2\pi\left(\frac{NA}{\lambda}\right)^2}circ\left(\frac{1}{zNA}\sqrt{\bar{x}^2+\bar{y}^2}\right). \tag{83}$$

Reducing Eqs. (82) and (83) gives the final result

$$J_A(x_1,y_1;x_2,y_2) = I_0 \frac{\pi r^2}{\pi(zNA)^2} circ\left(\frac{1}{zNA}\sqrt{\bar{x}^2+\bar{y}^2}\right)\left(2\frac{J_1\left(\frac{2\pi}{\lambda z}a\sqrt{\Delta x^2+\Delta y^2}\right)}{\frac{2\pi}{\lambda z}a\sqrt{\Delta x^2+\Delta y^2}}\right). \quad (84)$$

The phase term $e^{-j\psi}$ has been dropped since we are only concerned with the intensity.

Eq. (84) can also be written as

$$J_A(x_1,y_1;x_2,y_2) = I(\bar{x},\bar{y})\,\mu_A(\Delta x,\Delta y) \quad (85)$$

where

$$I(\bar{x},\bar{y}) = I_0 \frac{\pi r^2}{\pi(zNA)^2} circ\left(\frac{1}{zNA}\sqrt{\bar{x}^2+\bar{y}^2}\right) \quad (86)$$

is a function of the coordinate positions and represents the course variation in intensity and

$$\mu_A(\Delta x,\Delta y) = \left(2\frac{J_1\left(\frac{2\pi}{\lambda z}a\sqrt{\Delta x^2+\Delta y^2}\right)}{\frac{2\pi}{\lambda z}a\sqrt{\Delta x^2+\Delta y^2}}\right). \quad (87)$$

is a function of the difference of coordinates and represents the speckle correlation area. We can see from Eq. (86) that the area of the intensity envelope increases while the average intensity decreases at a rate proportional to the NA of the fiber as the mutual intensity propagates away from the fiber, which is what one would intuitively expect. As mentioned in the previous Section we again see that it is the source speckle correlation area determines the average intensity in the observation plane and the source intensity envelope determines the observed speckle correlation area.

Now that the propagation of the mutual intensity in the case of a multi-mode fiber has been determined we can now calculate the mean speckle correlation area which, using Eq. (72) is

$$A_c = \int_{-\infty}^{\infty}\int_{-\infty}^{\infty} \left|\mu_A\left(\Delta x, \Delta y\right)\right|^2 d\Delta x d\Delta y = \int_{-\infty}^{\infty}\int_{-\infty}^{\infty} \left| 2\frac{J_1\left(\frac{2\pi}{\lambda z} a\sqrt{\Delta x^2 + \Delta y^2}\right)}{\frac{2\pi}{\lambda z} a\sqrt{\Delta x^2 + \Delta y^2}} \right|^2 d\Delta x d\Delta y \,. \qquad (88)$$

The evaluation of Eq. (88) is given in [13] and [20],

$$A_c = \frac{\lambda^2 z^2}{\pi a^2} \,. \qquad (89)$$

Eq. (89) states that the mean speckle correlation area is a function of the source wavelength, fiber core area, and distance. Speckle can be minimized by using a source with a smaller wavelength, using a larger fiber, and minimizing the distance between the fiber and the SCPA.

It is worth mentioning that the above equations assume that all of the modes within the fiber are evenly excited. Failure to evenly excite the all of modes within the fiber will result in an increased speckle correlation area. Using Eq. (75) and Eq. (89) we see that the speckle correlation area is related to the number of modes in a fiber,

$$A_C = 2\pi \frac{NA^2 z^2}{M} \,. \qquad (90)$$

At this point we should reemphasize that speckle is a phenomena of coherent light. If the fiber were to be illuminated with an incoherent source, such as an LED, a speckle pattern would not be observed. Also, there is a limitation to which coherence exists. This

limitation is due to what is referred to as the coherence time. Coherence time is defined as the maximum relative time delay between two interfering beams [15], or in this case interfering modes, in which interference will occur. The coherence time of a source is determined by the optical bandwidth of the source

$$\tau_c = A\frac{1}{\Delta\nu}, \tag{91}$$

where A is a constant dependent on the shape of the power spectral density and $\Delta\nu$ is the half-power optical bandwidth. The coherence time is related to a path length difference over which interference will occur (coherence length) by

$$l_c = c\,\tau_c, \tag{92}$$

where c is the speed of light.

We can now use this relation to determine a fiber length over which a reduction in coherence will begin to take place. Using a ray approximation, the shortest path length traveled by a ray occurs at an angle of incidence $\theta = 0$ and is simply equal to the fiber length, L. The longest path length occurs for a ray incident at the maximum angle of incidence upon the fiber face at which internal reflection will still occur, θ_{max}, and travels a distance of $L/\cos(\theta_{max})$. The maximum path length difference within an optical fiber is given by,

$$\Delta L = \frac{L}{\cos\left(\theta_{\max}\right)} - L, \tag{93}$$

and the corresponding time delay is

$$\Delta T = \frac{n_1}{c}\Delta L. \tag{94}$$

Using Eq. (93) we see that the condition

$$\Delta L >> l_c \tag{95}$$

will result in a reduction in coherence between light traveling the two paths and therefore a reduction in speckle contrast. For example, the source used in the experiment discussed in Section 5.2 has a coherence length of 300 m. The laser light is launched down a 100 μm fiber with an NA of 0.22. One would need a fiber length greater than 1 km before a reduction in speckle contrast would be observed.

We can also define a fiber length in terms of the mode velocities. The velocity of a mode, v_{lm}, is governed by [26],

$$v_{lm} = \frac{c}{n_1}\left[1 - \frac{(l+2m)^2}{M}\Delta\right], \tag{96}$$

for $V >> 1$, where l and m are the mode indices with ranges of

$$l = 0, 1, ..., \sqrt{M} \tag{97}$$

$$m = 1, 2, ..., \frac{\left(\sqrt{M} - l\right)}{2} \tag{98}$$

and

$$\Delta = \frac{n_1 - n_2}{n_1}. \tag{99}$$

The time delay between modes is [27]

$$\Delta T = L\left[\frac{1}{v_{\min}} - \frac{1}{v_{\max}}\right], \tag{100}$$

and therefore the condition where L is such that $\Delta T \gg \tau_c$ will result in a reduction of coherence between the fastest and slowest propagating modes.

5.1.4 Integrated Speckle

The previous Section presented theory that describes speckle statistics at one or more points in space. When a photocell is illuminated with a speckled intensity pattern the incident light is integrated over the finite active photocell area and for this reason the statistical properties of integrated speckle must also be considered. In this Section the theory of integrated speckle is presented and follows that in [13]. It will be shown here that the illumination efficiency is a function of the ratio of the photocell area and the speckle correlation area. We begin the analysis with the case of a fully polarized speckle pattern and then modify the result to take into account the degree of polarization.

Individual photocells within the array have a finite area and their output is proportional to the average intensity incident upon the active area. The averaging of the intensity in the case of a finite area photocell is defined by

$$W = \frac{1}{A_P} \int_{-\infty}^{\infty} \int_{-\infty}^{\infty} D(x,y) I(x,y) dxdy \,, \tag{101}$$

where $I(x,y)$ is the incident intensity and $D(x,y)$ is a weighing function that represents the photocells responsivity over the active area. $D(x,y)$ in the case of a photocell with a uniform responsivity is described by

$$D(x,y) = \begin{cases} 1 & \textit{Inside Active Area} \\ 0 & \textit{Outside Active Area} \end{cases}, \tag{102}$$

and the photocell area, A_D, is

$$A_D = \int_{-\infty}^{\infty}\int_{-\infty}^{\infty} D(x,y)dxdy\,. \tag{103}$$

The mean integrated intensity is defined in as

$$\bar{W} = \frac{1}{A_D}\int_{-\infty}^{\infty}\int_{-\infty}^{\infty} D(x,y)\bar{I}dxdy = \bar{I}\,, \tag{104}$$

and the variance of W is,

$$\sigma_W{}^2 = \frac{\bar{I}^2}{A_D{}^2}\int_{-\infty}^{\infty}\int_{-\infty}^{\infty} K_D(\Delta x,\Delta y)\left|\mu_A(\Delta x,\Delta y)\right|^2 d\Delta x d\Delta y\,, \tag{105}$$

where K_D is the autocorrelation of the of the aperture

$$K_D(\Delta x,\Delta y) = \int_{-\infty}^{\infty}\int_{-\infty}^{\infty} D(x_1,y_1)D(x_1-\Delta x,y_1-\Delta y)\,dx_1 y_1\,. \tag{106}$$

A quantity of great importance to determining the illumination efficiency is the contrast of the integrated speckle and is defined by

$$C = \frac{\sigma_W}{\bar{W}}\,. \tag{107}$$

The reciprocal of the contrast is the rms signal-to-noise ratio

$$\left(\frac{S}{N}\right)_{rms} = \frac{\bar{W}}{\sigma_W}\,. \tag{108}$$

Defining

$$M = \left[\frac{1}{A_D{}^2}\int_{-\infty}^{\infty}\int_{-\infty}^{\infty} K_D(\Delta x,\Delta y)\left|\mu_A(\Delta x,\Delta y)\right|^2 d\Delta x d\Delta y\right]^{-1} \tag{109}$$

we have

$$C = \frac{1}{\sqrt{M}} \tag{110}$$

and

$$\left(\frac{S}{N}\right)_{rms} = \sqrt{M}\ . \tag{111}$$

The M parameter is paramount to determining the statistics of the integrated speckled intensity incident upon a photocell and is interpreted as being the average number of speckles incident upon the photocell. Since this is the case M warrants some further discussion. Let's begin by considering the two limiting cases; an extremely large photocell compared to the speckle correlation area and the case where the speckle is extremely small compared to the photocell.

For the first case, $K_D(\Delta x,\Delta y)$ is significantly wider than the complex coherence factor and we can pull $K_D(0,0)$ outside of the integral with the result

$$K_D(0,0) = \int_{-\infty}^{\infty}\int_{-\infty}^{\infty} D^2(x_1,y_1)dx_1dy_1\ , \tag{112}$$

which was the dimensions of area. Since $A_D{}^2/K_D(0,0)$ also has the dimensions of area we can define this quantity as the effective photocell area,

$$A_M = \frac{A_D{}^2}{\int_{-\infty}^{\infty}\int_{-\infty}^{\infty} D^2(x_1,y_1)dx_1dy_1}\ . \tag{113}$$

If the photocell has a uniform responsivity, $D(x_1,y_1)$ is unity inside the active area of the photocell and zero otherwise resulting in $A_M = A_D$.

Also, recalling Eq. (72)

$$A_c = \int_{-\infty}^{\infty}\int_{-\infty}^{\infty} \left|\mu_A(\Delta x,\Delta y)\right|^2 d\Delta x d\Delta y \tag{114}$$

shows that the parameter M, in this extreme case, is equal to the ratio of the area of the photocell and speckle correlation areas

$$M \approx \frac{A_D}{A_C} \quad \left(A_D >> A_C\right). \tag{115}$$

For the second case where the photocell is much smaller than the speckle, we can replace $|\mu|^2$ with unity resulting in

$$M \approx \left[\frac{1}{{A_D}^2}\int_{-\infty}^{\infty}\int_{-\infty}^{\infty} K_D(\Delta x,\Delta y)\,d\Delta x d\Delta y\right]^{-1} = 1 \quad \left(A_M << A_C\right). \tag{116}$$

Here we see that M never falls below unity and agrees with the interpretation of M as being the average number of speckles incident upon the photocell for no matter how small the photocell is there will always be at least one speckle incident upon the photocell.

An exact expression for M in the case of a step-index multi-mode fiber can be found by inserting the photocell aperture function and the appropriate complex coherence factor (Eq. (87)) into Eq. (109) which gives

$$M = \left[\frac{1}{{A_D}^2}\int_{-\infty}^{\infty}\int_{-\infty}^{\infty} K_D(\Delta x,\Delta y)\left|2\frac{J_1\left(\frac{2\pi}{\lambda z}a\sqrt{\Delta x^2+\Delta y^2}\right)}{\frac{2\pi}{\lambda z}a\sqrt{\Delta x^2+\Delta y^2}}\right|^2 d\Delta x d\Delta y\right]^{-1}. \tag{117}$$

Putting the argument of μ_A in terms of the mean speckle correlation area, A_C, given by Eq. (89) and assuming a uniform photocell responsivity we get

$$M = \left[\frac{1}{{A_D}^2}\int_{-\infty}^{\infty}\int_{-\infty}^{\infty} K_D(\Delta x,\Delta y)\left|2\frac{J_1\left(2\sqrt{\frac{\pi}{A_C}}\sqrt{\Delta x^2+\Delta y^2}\right)}{2\sqrt{\frac{\pi}{A_C}}\sqrt{\Delta x^2+\Delta y^2}}\right|^2 d\Delta x d\Delta y\right]^{-1}. \tag{118}$$

A plot of $M(A_D/A_C)$ is shown below (Figure 56) for the case of a step-index multi-mode fiber and a rectangular photocell with dimensions $4L$ x L. Note that the values of M in the two extremes mentioned previously are in agreement with Eqs. (115) and (116).

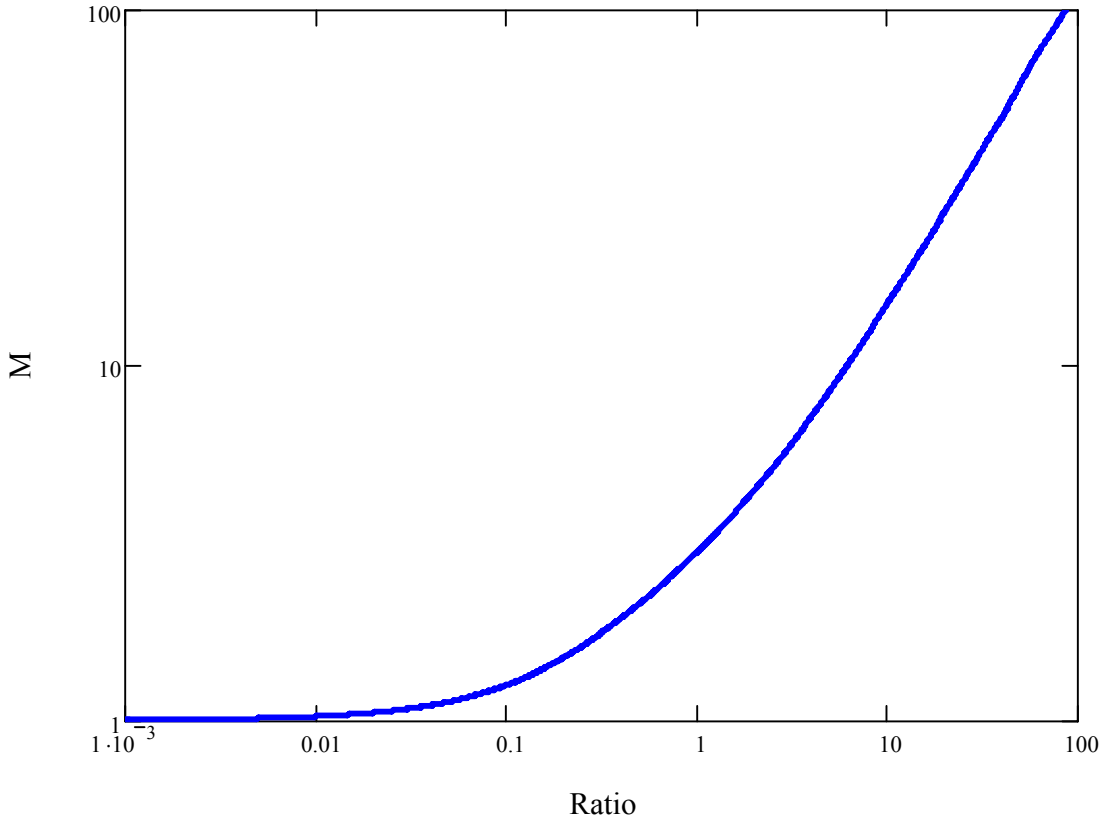

Figure 56. Plot of M as a function of the ratio of the photocell and speckle areas (A_D/A_C).

At this point, illumination efficiency can be statistically defined by considering that there will be some photocells that illuminated more than others due to the random nature of speckle. Also, the illumination efficiency will be determined by the photocell that is illuminated the least, W_{min}. With in mind, we define the illumination efficiency as

$$\eta_I = \frac{W_{\min}}{\bar{W}}, \tag{120}$$

and assume that the least illuminated cell is illuminated at a value one standard deviation below the mean

$$W_{\min} = \bar{W} - \sigma_W . \tag{121}$$

Substituting Eq. (121) into Eq. (120) gives

$$\eta_I = \frac{\bar{W} - \sigma_W}{\bar{W}} = 1 - \frac{\sigma_W}{\bar{W}}, \tag{122}$$

and recognizing that the last term is equal to the integrated speckle contrast (Eq. (110)) and using Eq. (122) we have

$$\eta_I = 1 - C = 1 - \frac{1}{\sqrt{M}} . \tag{123}$$

Up to this point it had been assumed that the speckle pattern was polarized. Multi-mode fibers generally have an unpolarized output. We now take into account the degree of polarization, *P*, of the speckle pattern and its effect on the illumination efficiency. Goodman [13] treats the polarization effect by expressing the intensity, *I*(*x,y*), in terms of two statistically independent intensities

$$I(x,y) = I_{\parallel}(x,y) + I_{\perp}(x,y), \tag{124}$$

using

$$\begin{aligned} \bar{I}_{\parallel} &= \frac{1}{2}\bar{I}(1+P) \\ \bar{I}_{\perp} &= \frac{1}{2}\bar{I}(1-P) \end{aligned}, \tag{125}$$

and following the same process as for a polarized speckle pattern to arrive at

$$C = \frac{1}{2}\left[\frac{(1+P)^2}{M_{\parallel}} + \frac{(1-P)^2}{M_{\perp}} \right]^{\frac{1}{2}} . \tag{126}$$

If $M_{\parallel} = M_{\perp} = M$, then *C* becomes

$$C = \left[\frac{\left(1 + P^2\right)}{2M} \right]^{\frac{1}{2}}, \tag{127}$$

where for the case of completely polarized speckle, $P = 1$, we get Eq. (110) and in the case of an unpolarized multi-mode fiber output, $P = 0$, the efficiency is

$$\eta_I = 1 - \frac{1}{\sqrt{2M}}. \tag{128}$$

One can easily see that it is more efficient to illuminate an SCPA using an unpolarized speckle pattern. To illustrate this, the illumination efficiency is plotted for both the polarized and unpolarized case (Figure 57). There is a roll off in efficiency that occurs at a ratio of 5. At a ratio of 20 the illumination efficiency is ~85% for the unpolarized case and ~ 80% for the polarized case. Increasing the ratio to 100 only gives an additional ~10% in efficiency.

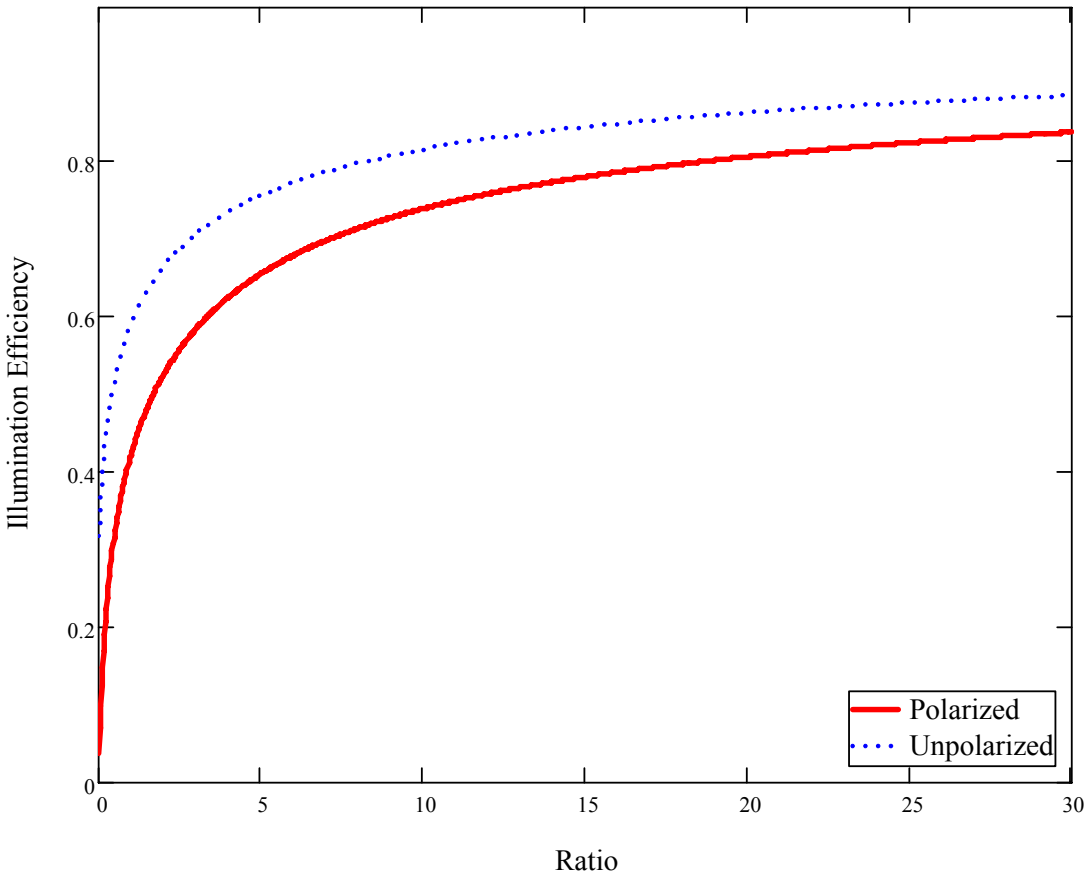

Figure 57. Plot of the illumination efficiency for both the polarized and unpolarized case.

Eq. (128) is derived by defining the minimum integrated speckle intensity as being one standard deviation below the mean. As such, Eq. (128) is an upper limit for the illumination efficiency and the actual value may be lower due to the probability of having a value of $W_{\min}$ that is lower than one standard deviation below the mean. Also, a non-uniform illumination intensity envelope incident across the SCPA will lower the value of η_I.

5.2 Experimental Results

Optical efficiency when using multi-mode illumination is dependent on the ratio of the photocell area to the speckle correlation area. The speckle correlation area is dependent on wavelength, fiber core radius, and propagation distance. Theory presented in the previous sections is demonstrated here by measuring the I_{SC} relative to the optical power incident upon an SCPA as a function of the mean speckle correlation area.

In this experiment, SCPAs are illuminated with 100 μm core and 400 μm core, 0.22 NA multi-mode optical fibers. Two SCPA configurations were tested. On configuration consisted of 920 series connected photocells arranged in a circular geometry (r = 2.2mm) with each photocell being 60 x 270 μm in dimension (Figure 58) and the other configuration is similar to the first except that the array consisted of 230 photocells that are 120 x 550 μm. The illumination source is the same 1064 nm source that was used in the single-mode illumination experiment. Light from the laser is focused into the optical fibers which are ~1 m in length and looped such that it passes through a mode scrambler three times in order to evenly excite all of the modes within the optical fiber. The distance between the fiber output and the SCPA is increased in order to increase the speckle correlation area. Figure 59 shows a schematic of the test setup.

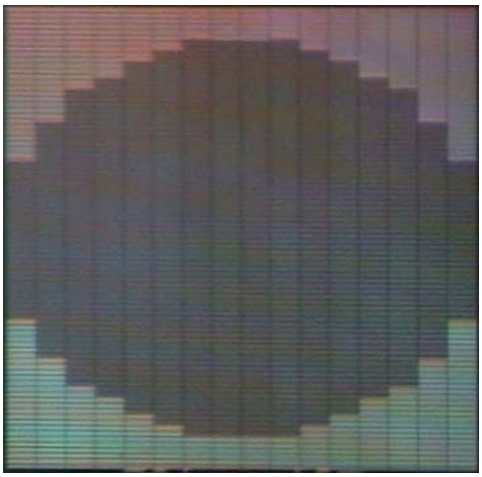

Figure 58. Microscope image of a 920 cell SCPA.

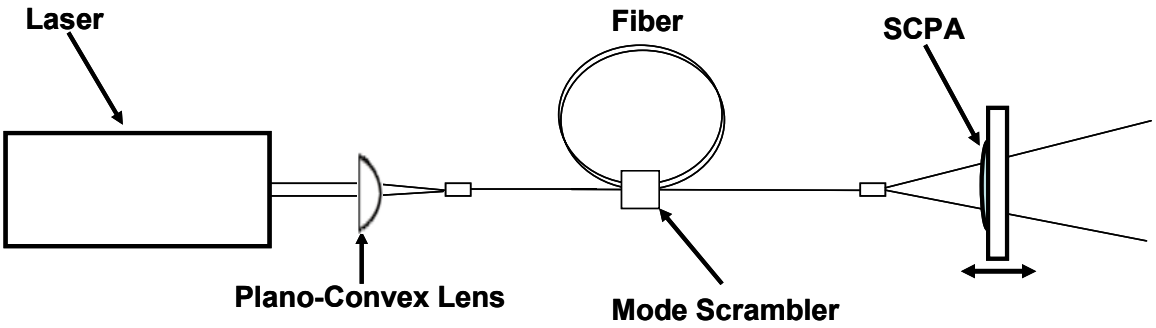

Figure 59. Schematic of multi-mode illumination test setup.

When experimentally determining $\eta_{I,}$ for increasing distances from the fiber surface (increased speckle correlation areas), we need to know three things: $\mathscr{R}_{array}$, I_{SC}, and the optical power that is incident upon the SCPA, $P_{incident}$. Using the above pieces of information and the following equation,

$$\eta_I = \frac{I_{SC}}{P_{incident}\mathscr{R}_{array}}, \tag{129}$$

the illumination efficiency can be calculated. The ratio $A_D \backslash A_c$ must also be known for each point the illumination efficiency is calculated in order to directly compare the data to the theory.

The first step in this experiment is to determine, $\mathscr{R}_{array}$, the SCPA responsivity. This is done by illuminating the SCPA using the single-mode experimental setup and applying Eq. (55) to calculate the effective power, or the power that contributes to I_{SC}. When a 2.2 mm radius SCPA is illuminated with a 446 mW Gaussian beam, at an optimum beam diameter, Eq. (55) gives an effective power of 164 mW. I_{SC} is calculated by measuring the voltage across a small valued resistor that is connected in series with the SCPA. The responsivity for the array is then given by

$$\mathscr{R}_{array} = \frac{I_{SC}}{P_{effective}}, \tag{130}$$

The measured responsivity for each device tested is listed below in Table 6 (230 cell SCPA) and Table 7 (920 cell).

Table 6. Responsivity measurements for 230 cell SCPAs.

S/N	V_{out} (mV)	R (kΩ)	I_{sc} (μA)	$\mathscr{R}_{array}$ (μA/W)
1	667.4	145.61	2.02	27.95
2	1165.4	145.61	1.78	48.76
3	888.5	145.61	6.08	37.06

Table 7. Responsivity measurements for 920 cell SCPAs.

S/N	V_{out} (mV)	R (kΩ)	I_{sc} (μA)	$\mathscr{R}_{array}$ (μA/W)
1	294.84	145.61	2.02	12.31
2	259.34	145.61	1.78	10.85

The array responsivity assumes that each cell is identical in performance. Initially the differences in responsivities for the SCPAs were a concern. It was thought that these differences could be due to an underperforming cell(s) within an array. If this was correct it would be impossible to determine the true responsivity of the array given uniform cell performance. This is due again to the current limiting behavior of the least illuminated cell or in this case the cell with the lowest responsivity. If the current were

actually limited by this, the array responsivity would be lower as a result. Fortunately, it appears the differences in array responsivities are indeed uniform throughout the respective array. This conclusion is based on two things. First, as we shall see later (Figures 62 - 65), the SCPAs produced similar experimental results. Second, the device designer is confident that the fabrication process is such that it is unlikely there would be non-uniformities from cell to cell. Any non-uniformity would be on the scale of a wafer.

Next, we measure the power incident on the SCPA. The laser beam is focused into a step-index multi-mode optical fiber and the fiber output was aligned such that the beam was propagating in parallel with the optics rail. An aperture having the same radius as the SCPA (2.2 mm) was attached to the optics rail and the power through the aperture was recorded at several distances from the fiber surface (Figure 60). The SCPA was then placed at those same distances and I_{SC} was recorded using a curve tracer. Mounting of the SCPA to the optics rail was achieved using translation stages which allowed for optimization of the alignment and precise control of the distance from the fiber surface (Figure 61). Now that $\mathscr{R}_{array}$, I_{SC}, and $P_{incident}$ are known we can now calculate η_I by using Eq. (129). The results from this experiment are plotted below in Figures 62 and 63 for the 230 cell SCPA with a 100 μm and 400 μm core diameter fiber, respectively. Figures 64 and 65 give the results from the 920 cell SCPA with a 100 μm and 400 μm core diameter fiber, respectively. The data shows that the efficiency indeed does decrease as a function of distance from the fiber. This again is due to an increase in the mean speckle correlation area as z increases. At this point the illumination efficiency is in terms of distance from the fiber, z. Next, we will discuss the measurement of the mean

speckle correlation area in terms of z and then compare the efficiency data to the theory discussed in the previous Section.

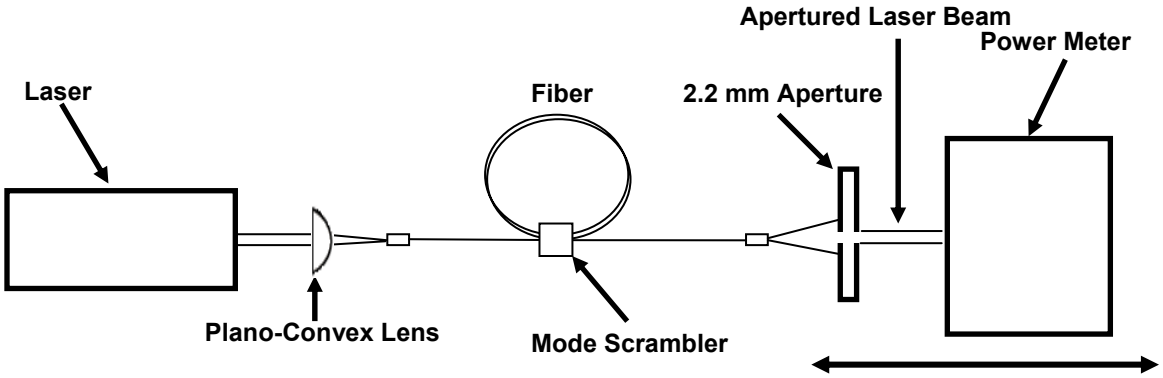

Figure 60. Schematic of test setup used to measure the power incident upon the SCPA.

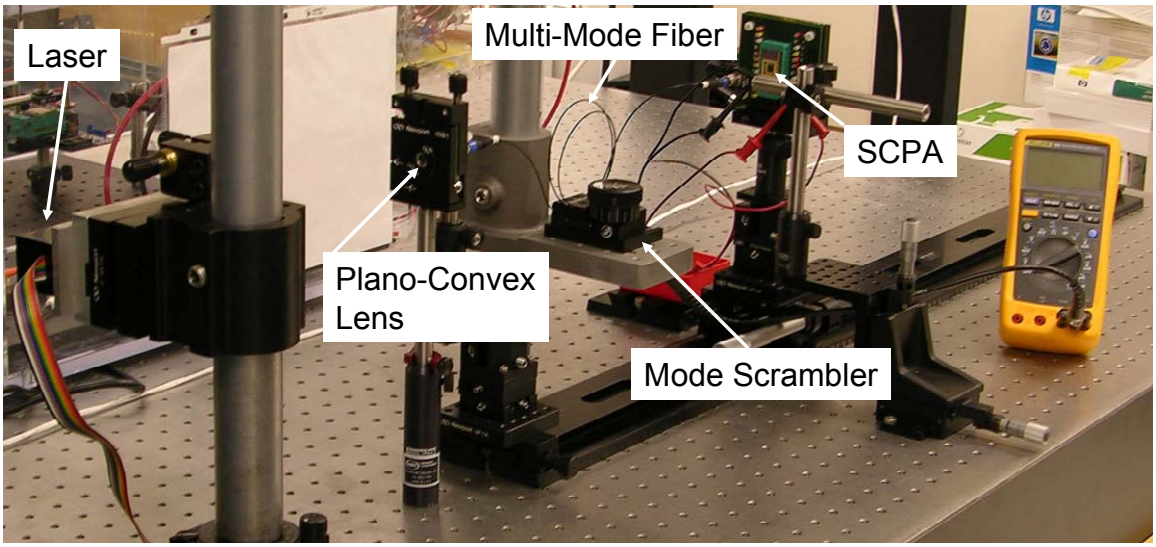

Figure 61. Photograph of multi-mode test setup

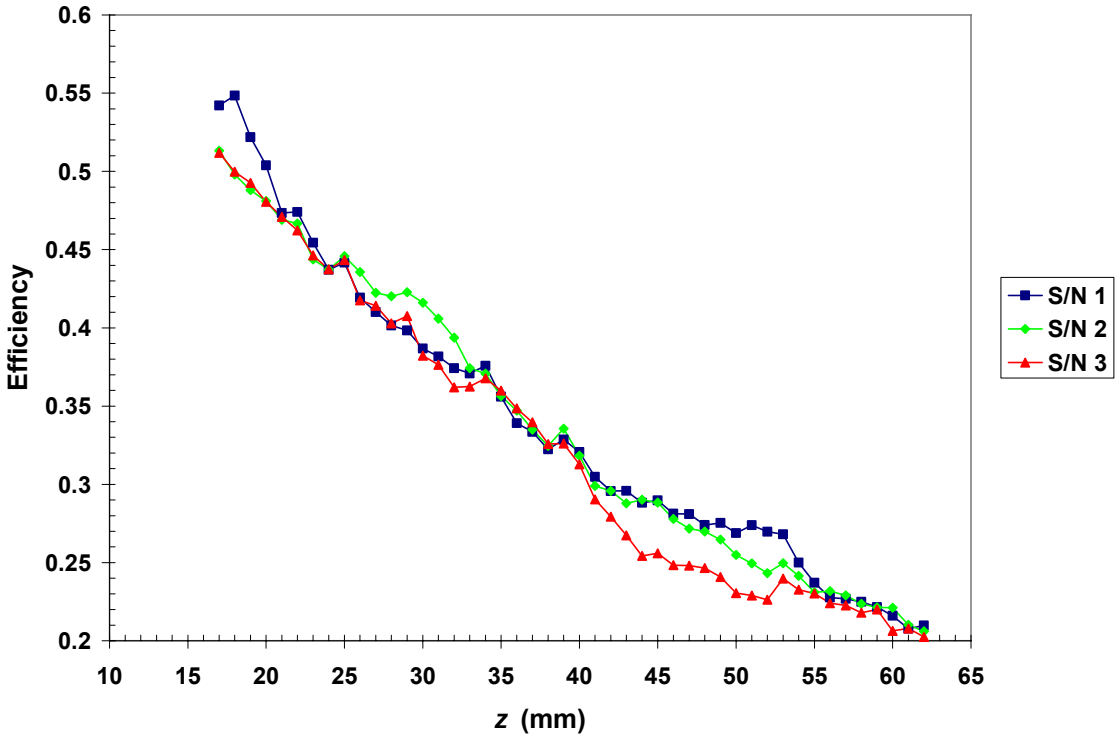

Figure 62. Test results for 230 cell SCPAs illuminated with a 100 µm core fiber.

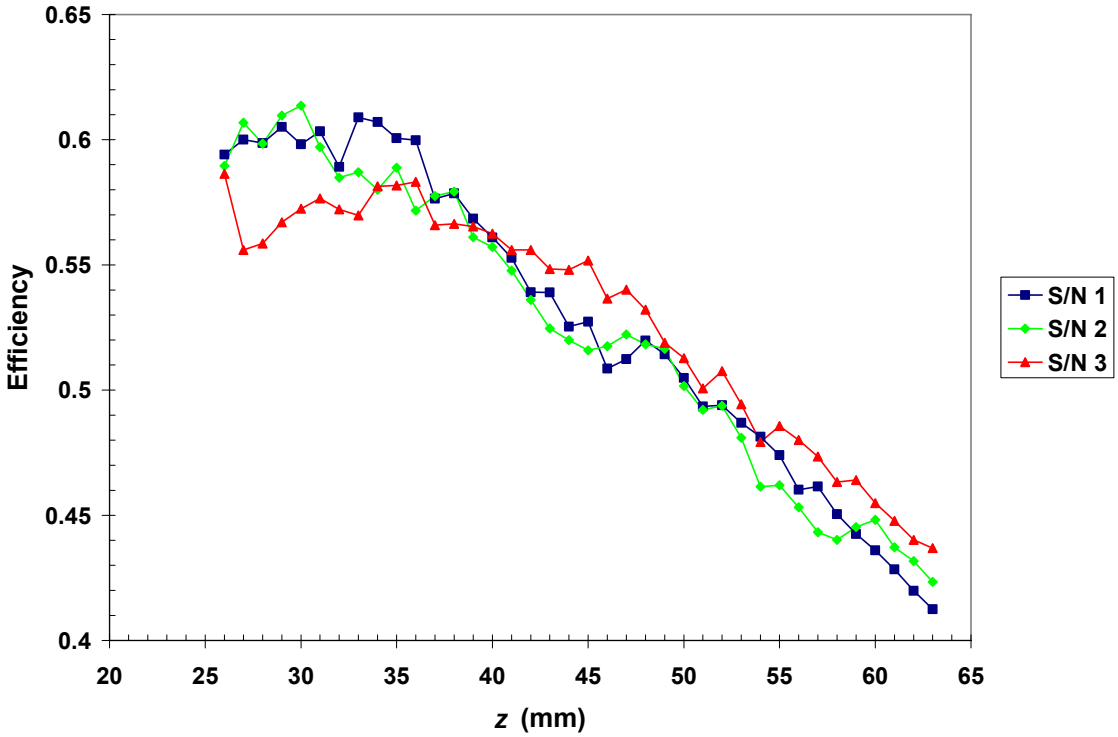

Figure 63. Test results for 230 cell SCPAs illuminated with a 400 µm core fiber.

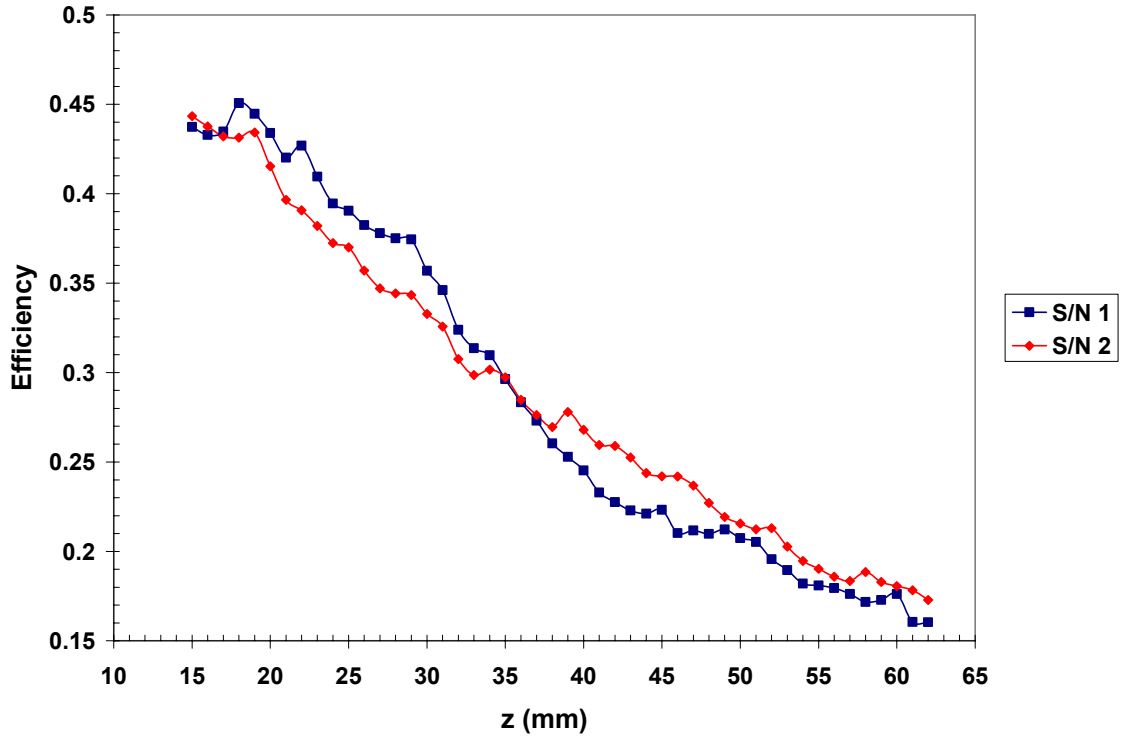

Figure 64. Test results for 920 cell SCPAs illuminated with a 100 µm core fiber.

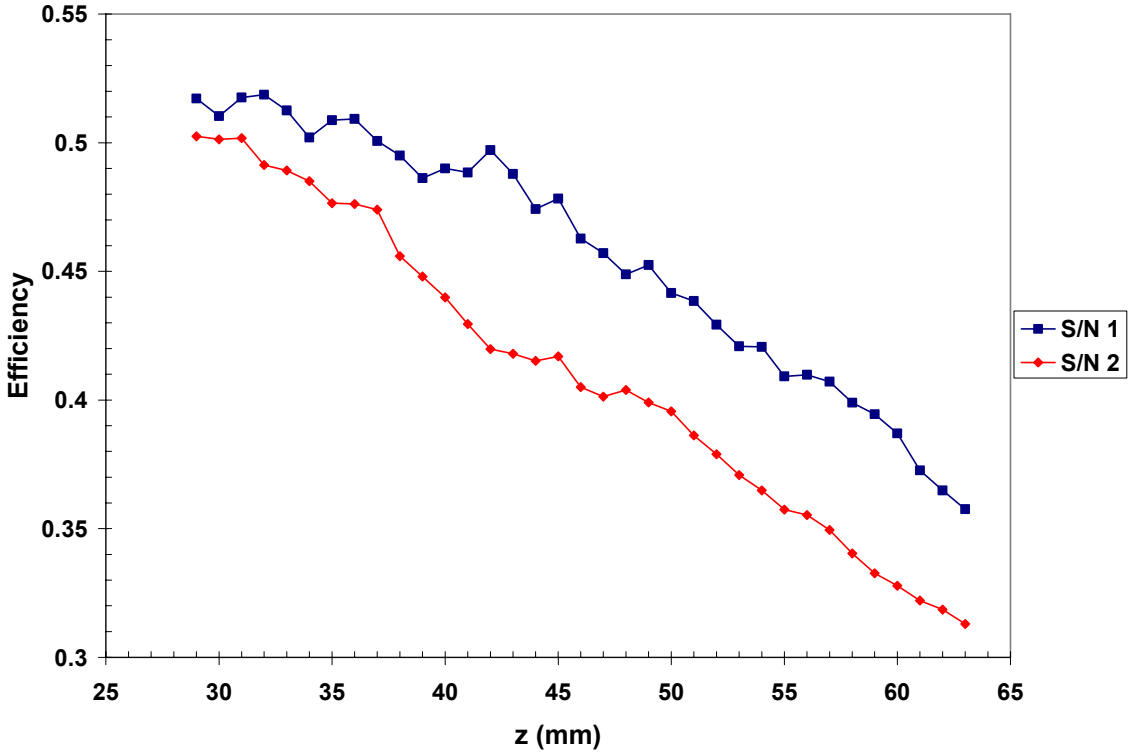

Figure 65. Test results for 920 cell SCPAs illuminated with a 400 µm core fiber.

The last piece of information required from this experiment is the speckle correlation area along z. Determining the speckle correlation area is a three part process. First, an image of the speckled intensity profile, at a known z, is obtained using a beam profiling camera. Second, we need to calculate the autocorrelation function of that image. Then the width of the spike in the autocorrelation function is related to A_C.

The test setup for measuring the speckle width was accomplished by first replacing the SCPA with a laser beam profiler (Figure 66). An image of the speckled intensity profile was then recorded at several distances along z. This process was performed for both fiber diameters. The autocorrelation function is calculated for each image using MATLAB. A single speckled image and the corresponding autocorrelation image are shown in Figures 67 and 68, respectively. These images are produced by a 400 μm core fiber at a distance of 70.5 mm.

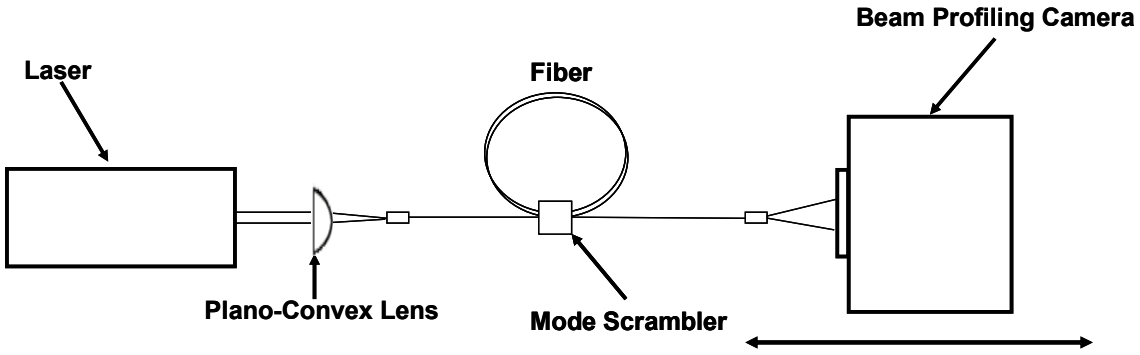

Figure 66. Schematic of setup used in acquiring images of the speckled intensity profile.

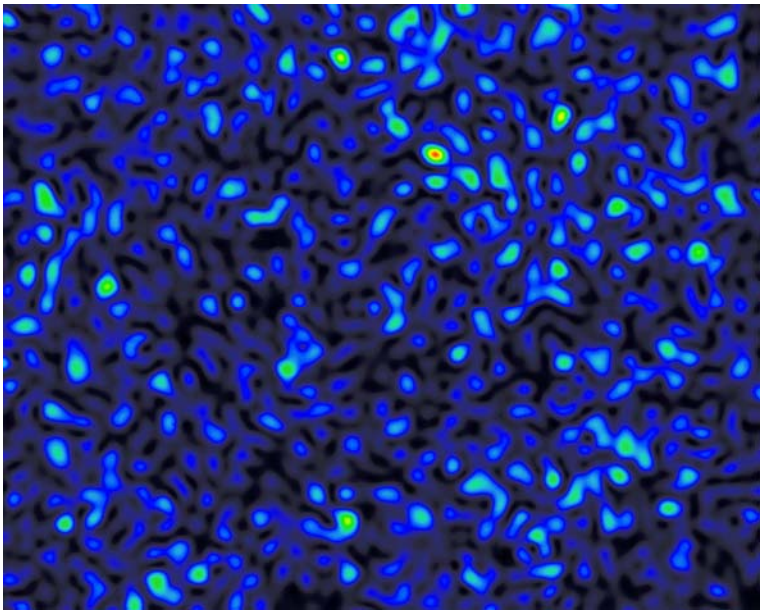

Figure 67. Image of a speckle pattern produced by a 400 μm fiber at distance of 70.5 mm.

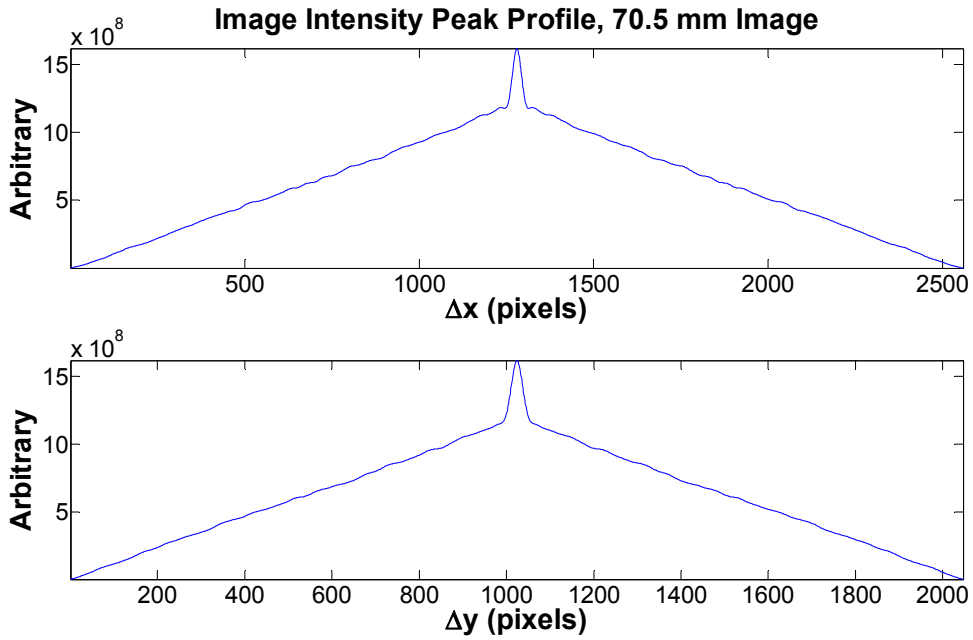

Figure 68. Autocorrelation of a speckle pattern produced by a 400 μm fiber at distance of 70.5 mm.

Figure 68 is a 2D cross-section of the 3D autocorrelation taken along the major and minor axes. The mean speckle correlation area is found by measuring the base width of the spike in the image autocorrelation. Referring back to Eqs. (61) and (62)

$$R_I\left(x_1,y_1;x_2,y_2\right)=\left\langle I\left(x_1,y_1\right)I\left(x_2,y_2\right)\right\rangle, \tag{131}$$

and

$$R_I\left(x_1,y_1;x_2,y_2\right)=\left\langle I\left(x_1,y_1\right)\right\rangle\left\langle I\left(x_2,y_2\right)\right\rangle+\left|J\left(x_1,y_1;x_2,y_2\right)\right|^2, \tag{132}$$

we see that the autocorrelation depicted in Figure 66 consists of two terms.

The first term represents the intensity envelope and is broad in terms of (Δx,Δy) and the second term represents the mutual intensity of the fields and is narrow in terms of (Δx,Δy). The triangular shape of the first term is a result of the rectangular intensity envelope. The rectangular shape of the intensity envelope is due to the aperturing caused by the geometry of the detector array in the beam profiling camera. Taking the autocorrelation of rect (x) gives tri (x) with a base width twice that of rect (x). Note that the detector array in the beam profiling camera consists of 1280 x 1024 pixels and the width of the image autocorrelation is 2560 x 2048.

We now turn our attention to the second term in Eq. (132), the mutual intensity, which we will use to calculate the mean speckle correlation area. Eq. (84) tells us that the spike in the autocorrelation function is of the form

$$J_A\left(x_1,y_1;x_2,y_2\right)=I_0\frac{\pi r^2}{\pi\left(zNA\right)^2}circ\left(\frac{1}{zNA}\sqrt{\bar{x}^2+\bar{y}^2}\right)\left(2\frac{J_1\left(\frac{2\pi}{\lambda z}a\sqrt{\Delta x^2+\Delta y^2}\right)}{\frac{2\pi}{\lambda z}a\sqrt{\Delta x^2+\Delta y^2}}\right). \tag{133}$$

Recalling that the normalized mutual intensity (Eq. (71)),

$$\mu\left(x_1,y_1;x_2,y_2\right)=\frac{J\left(x_1,y_1;x_2,y_2\right)}{\left[J\left(x_1,y_1;x_1,y_1\right)J\left(x_2,y_2;x_2,y_2\right)\right]^{\frac{1}{2}}}, \tag{134}$$

is related to the mean speckle correlation area by Eq. (72)

$$A_c = \int_{-\infty}^{\infty}\int_{-\infty}^{\infty} \left|\mu(\Delta x, \Delta y)\right|^2 d\Delta x d\Delta y \,, \tag{135}$$

we have (Eq. (88)),

$$A_c = \int_{-\infty}^{\infty}\int_{-\infty}^{\infty} \left|\mu(\Delta x, \Delta y)\right|^2 d\Delta x d\Delta y = \int_{-\infty}^{\infty}\int_{-\infty}^{\infty} \left| 2\frac{J_1\left(\frac{2\pi}{\lambda z} a\sqrt{\Delta x^2 + \Delta y^2}\right)}{\frac{2\pi}{\lambda z} a\sqrt{\Delta x^2 + \Delta y^2}} \right|^2 d\Delta x d\Delta y \,. \tag{136}$$

Referring to Eq. (89) we have,

$$A_c = \frac{\lambda^2 z^2}{\pi a^2} \,. \tag{137}$$

Taking the base-width of the spike in the autocorrelation image, which we will loosely call the "speckle width" (S_0), as being equal to the twice the value of $\sqrt{\Delta x^2 + \Delta y^2}$ where

$$2\frac{J_1\left(\frac{2\pi}{\lambda z} a\sqrt{\Delta x^2 + \Delta y^2}\right)}{\frac{2\pi}{\lambda z} a\sqrt{\Delta x^2 + \Delta y^2}} \tag{138}$$

first falls to zero,

$$J_1(3.83) = 0 \,, \tag{139}$$

we have

$$S_0 = 3.83\frac{\lambda z}{\pi a} \,. \tag{140}$$

The mean speckle correlation area is related to the speckle width by

$$A_C = \frac{\pi}{3.83^2} S_0^{\,2} = 0.214 S_0^{\,2} \,. \tag{141}$$

Even though the autocorrelation image was not normalized the results are still valid because the normalization of the mutual intensity has absolutely no effect on the argument of the Bessel function. In Figures 69 and 70 S_0 is plotted as a function of z and compared to the theory for the case of a 100 μm and 400 μm core fiber, respectively. Figures 71 and 72 are plots of A_C using Eq. (141) compared to calculated values of A_C using Eq. (137) for the 100 μm and 400 μm core fiber respectively. The data is in agreement with the theory in all four figures.

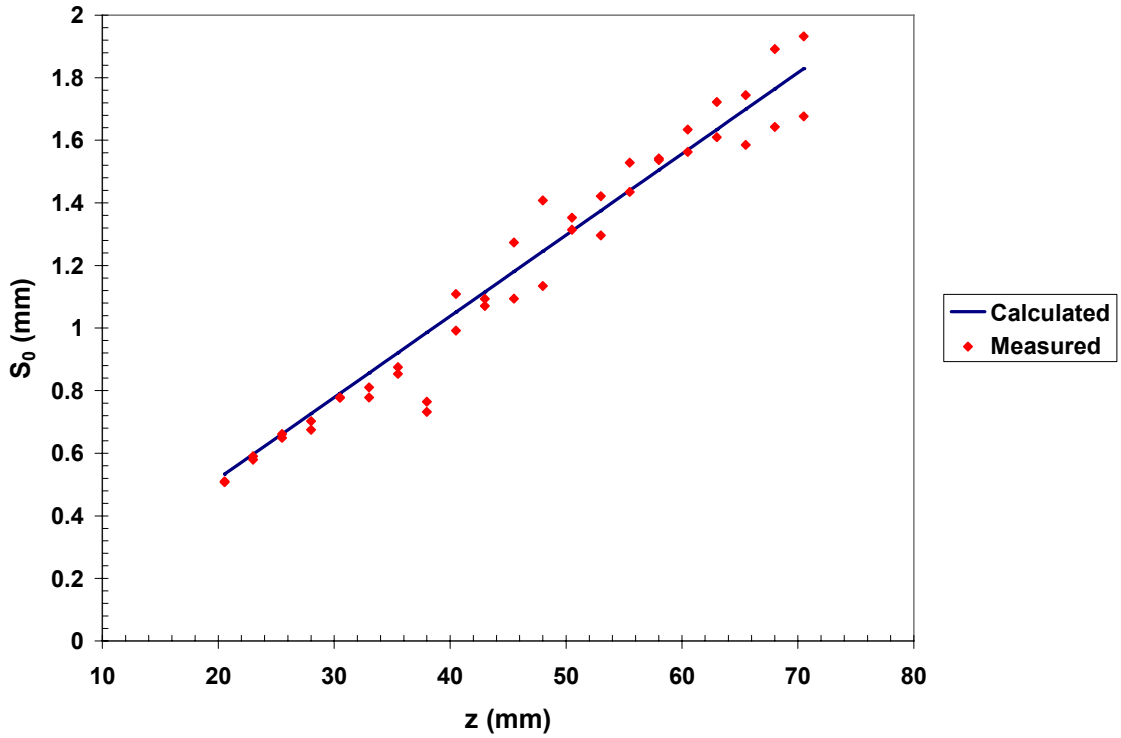

Figure 69. Speckle width (S_0) along the major and minor axes of the observation plane for a 100 μm fiber.

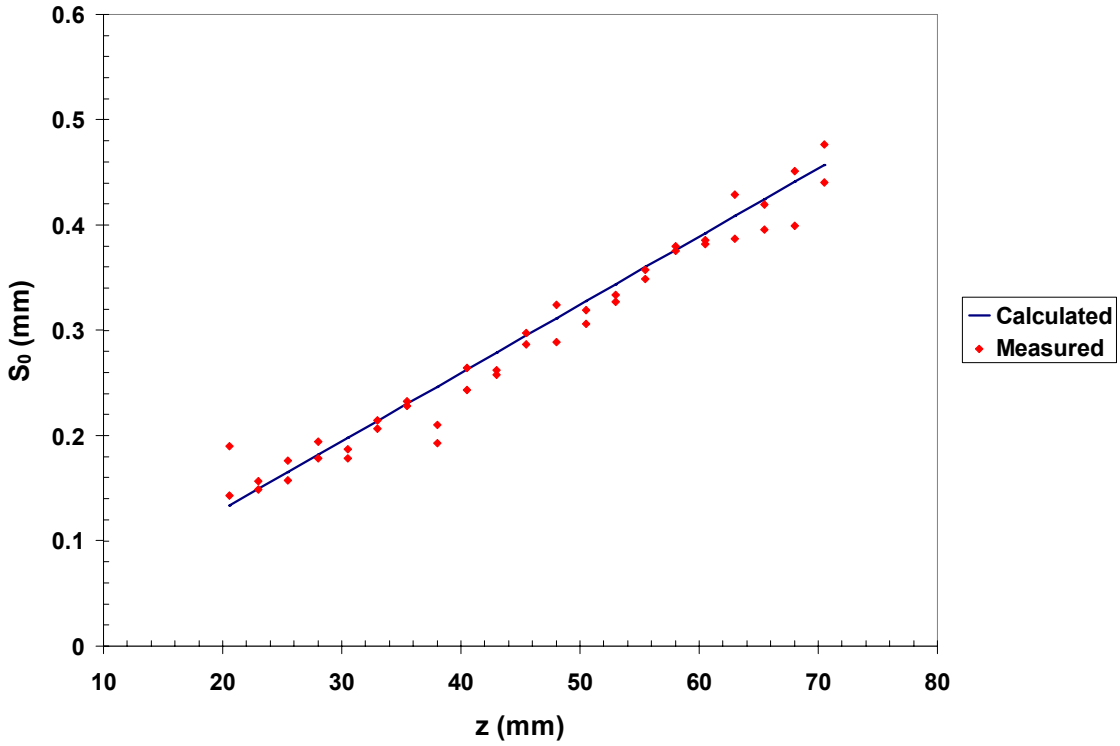

Figure 70. Speckle width (S_0) along the major and minor axes of the observation plane for a 400 µm fiber.

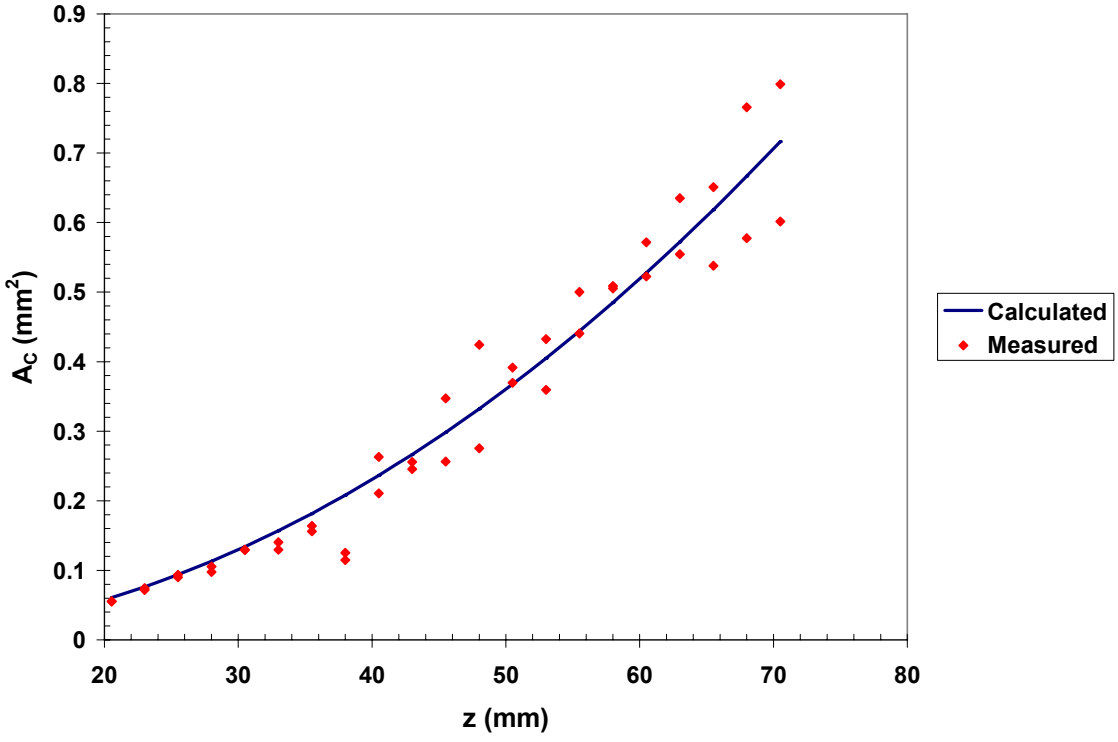

Figure 71. Speckle correlation area (A_C) along the major and minor axes of the observation plane for a 100 µm fiber.

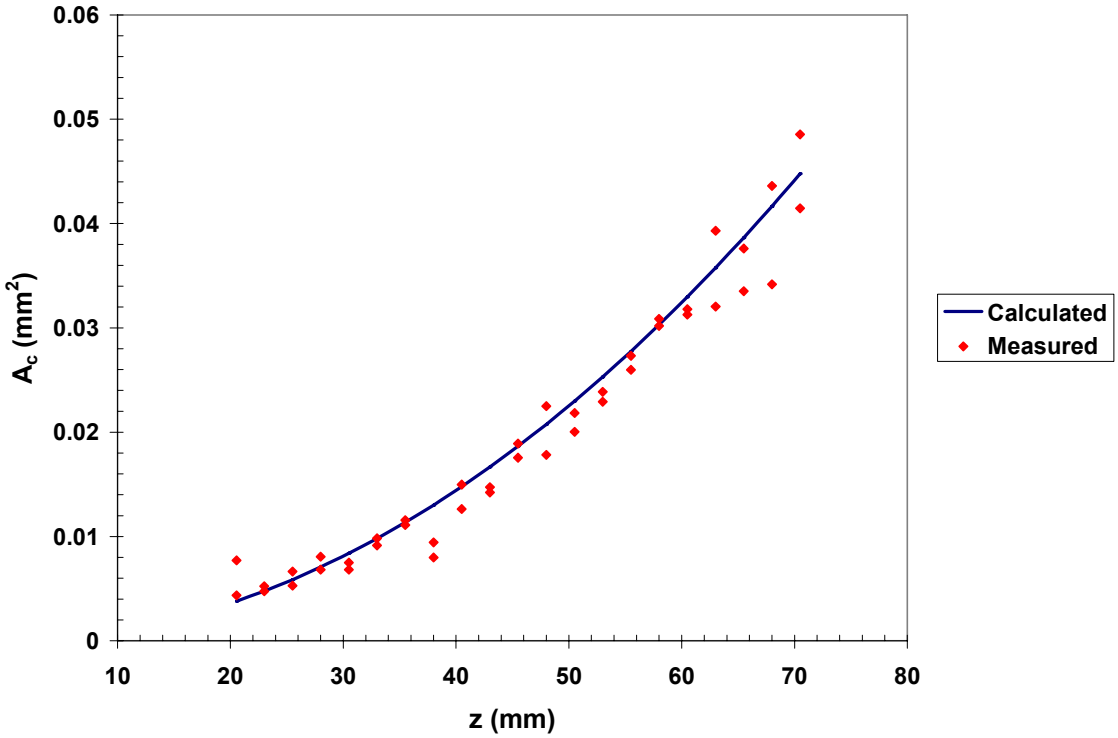

Figure 72. Speckle correlation area (A_C) along the major and minor axes of the observation plane for a 400 μm fiber.

Now we plot the results from the illumination efficiency tests as a function of the ratio A_D/A_C (Figure 73). The data is plotted against the efficiency curve for unpolarized illumination given that illumination from a multi-mode fiber is generally unpolarized. Two methods were used to verify that the illumination was indeed unpolarized. First a polarizer was inserted between the fiber output and a power meter. The polarizer was rotated while monitoring the power meter. As the polarizer was rotated there was no change in transmitted power indicating that the light was completely unpolarized. Another indication of the degree of polarization of the speckle pattern is the contrast, C, of the pattern. For a completely polarized and fully developed speckle pattern the ratio of the standard deviation to the mean is unity ($C = 1$). In the case of an unpolarized speckle

pattern this ratio is $C = 1/\sqrt{2}$ [11]. Measurements of the contrast of the acquired speckle patterns also show that indeed the speckle pattern is unpolarized. Measurements of the contrast of the speckle pattern produced by a 100µm core fiber ranged between 0.6 and 0.72 and the 400 µm fiber had a contrast ranging between 0.57 and 0.68.

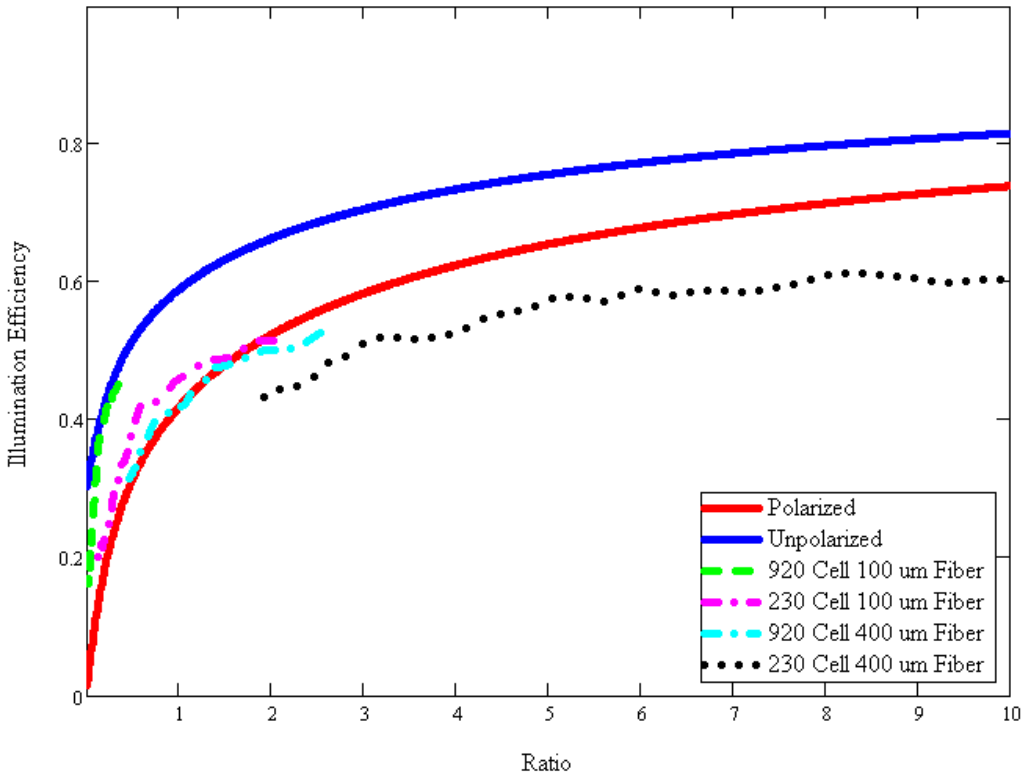

Figure 73. Unpolarized multi-mode illumination efficiency test results plotted as a function of the ratio A_D/A_C.

The trend in the data is in good agreement with the theory but there is a quantative deviation from the theory for the cases in which the 230 cell SCPA is illuminated with a 100 µm fiber and for both SCPA types in the case of 400 µm fiber illumination. These quantative differences are explained by the two following arguments.

First, as mentioned earlier, Eq. (128) was considered an upper limit on the efficiency. This is due to the statistical nature of speckle. Illumination efficiency was defined in Eq. (120) in terms of the ratio of the least illuminated photocell and the average illumination intensity. The photocell that is illuminated the least, $W_{\min}$, was defined in Eq. (121) as being one standard deviation below the mean. This definition was chosen so that η_I could be defined in terms of the mean speckle correlation area through the contrast, C, of the integrated speckle pattern. In reality, a probability exists that the minimally illuminated photocell may be illuminated at a level less than one standard deviation below the mean and as such would result in a lower efficiency. By integrating the probability density function (PDF) of the integrated speckle pattern we can calculate the probability of any value of $W_{\min}$ for a given value of M.

An approximation for the PDF of polarized integrated speckle is [13] – [14]

$$p(W) = \frac{\left(\frac{M}{\overline{W}}\right)^{M} W^{M-1} e^{-M\frac{W}{\overline{W}}}}{\Gamma(M)}, \tag{142}$$

where $\Gamma(M)$ is the gamma function. A closed form solution for the PDF of an unpolarized integrated speckle is not known. Obtaining such a solution would involve the Fourier inversion of the product of the characteristic functions for both polarization components. We can nonetheless gain insight by considering the case of polarized speckle. Figure 74 shows Eq. (142) plotted as a function of $W/\overline{W}$ for several values of M.

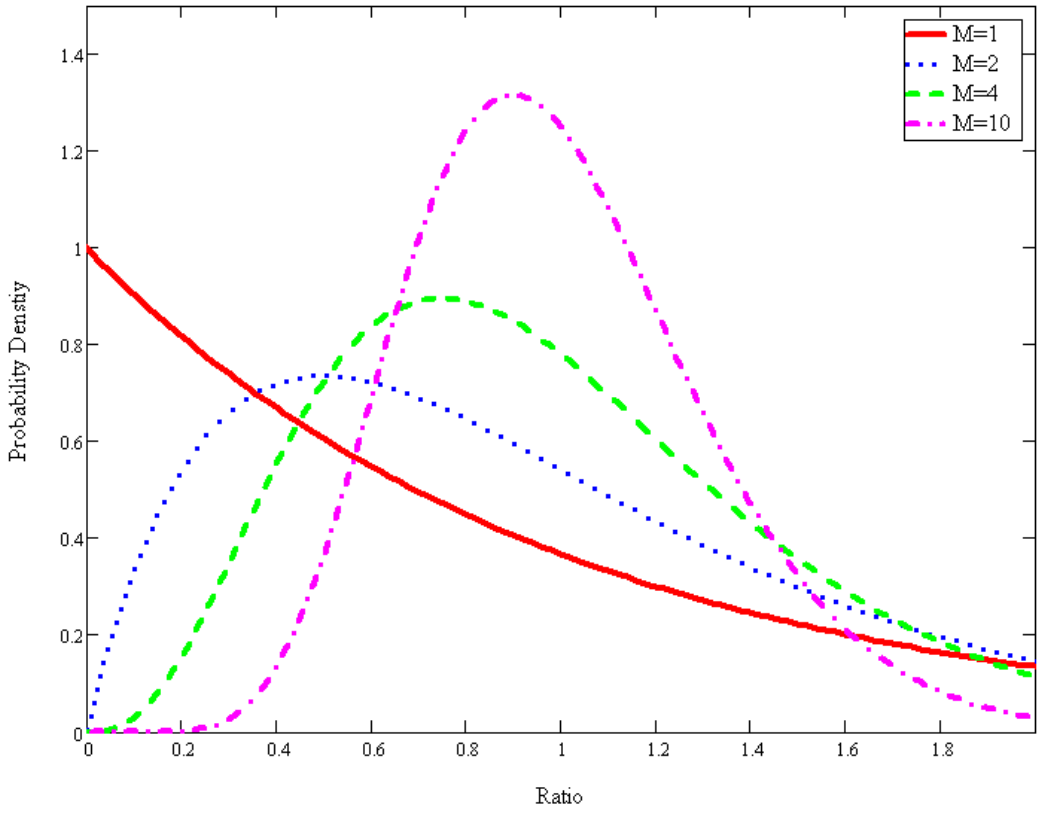

Figure 74. PDF of an unpolarized integrated speckle pattern plotted as a function of the ratio $W/\bar{W}$.

Let's consider the following example. Using Eq. (115) we see that M=10 gives an efficiency of 68.4%. This again assumes that the least illuminated photocell is illuminated at a level that is one standard deviation below the mean. Integrating Eq. (142) will give us the probability of $W/\bar{W}$ along a given interval. This ratio can be related to the illumination efficiency (Eq. (120)) and referring to Figure 75 we can see that there exists a probability that the ratio $W/\bar{W}$ is less than 0.684. Even though the probability is small for a single photocell it becomes significant when there are hundreds of photocells within the array. Figure 76 shows a speckle pattern overlaid upon an SCPA schematic drawing and further illustrates the statistical nature of speckle.

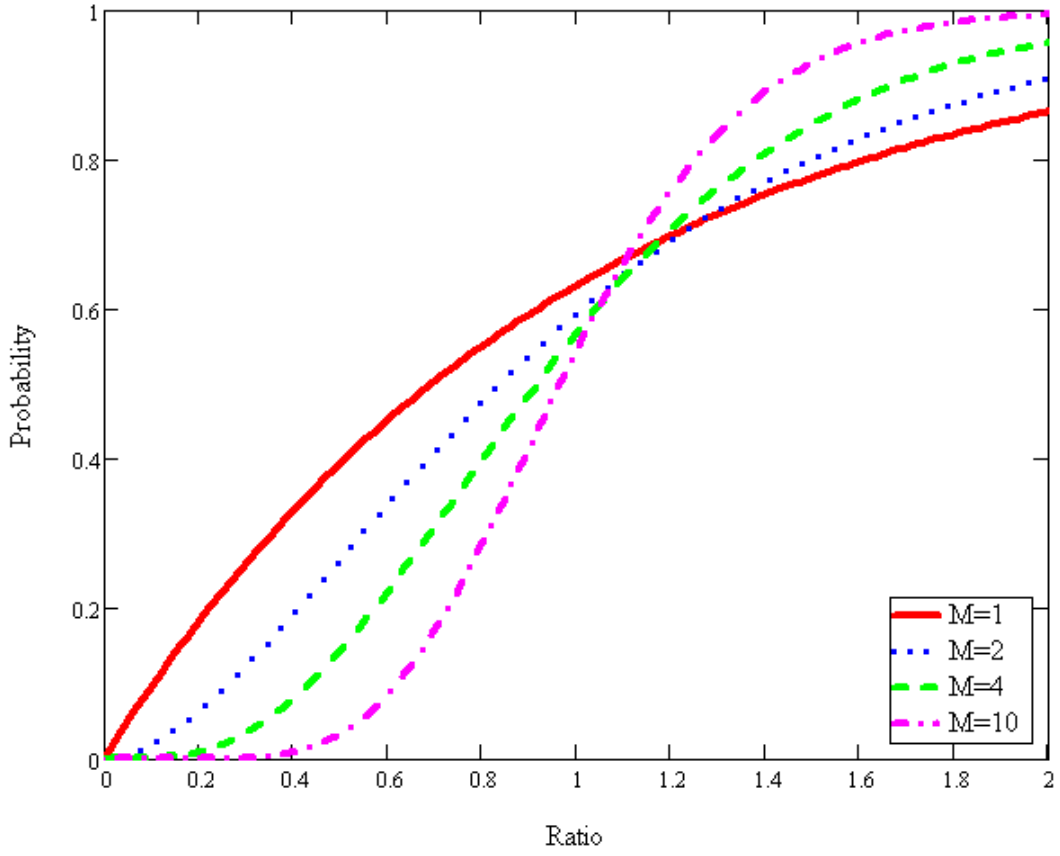

Figure 75. Probability of $W/\bar{W}$ for a given M.

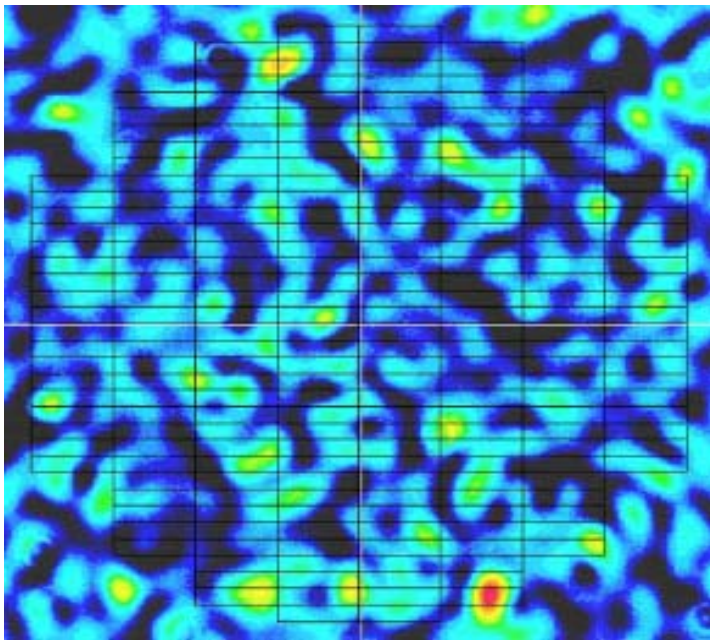

Figure 76. Speckled intensity pattern overlaid upon a schematic drawing of an SCPA.

Second, it appears that the results from the test condition of where we have a 920 cell SCPA illuminated with a 100 μm fiber is not explained by the above hypothesis. It is believed that Zener breakdown of one or more of the dark cells explains why this test condition deviated from the trend in the test data. For this test configuration the SCPA had a large number of photocells with small areas. This coupled with the use of the 100 μm fiber (large speckle correlation area) leads to a condition where one or more of the cells can be completely dark. Under short-circuit conditions a completely dark photocell has the potential of the entire SCPA dropped across it in the reverse bias direction. As long as the reverse bias potential does not exceed the reverse bias breakdown voltage of the photocell it will continue to limit the current. Typically the reverse bias breakdown voltage per cell is several times higher in magnitude than the illumination generated voltage. This means that there must be several times as many cells that are illuminated versus those that are not. It is probable that the test conditions were such that reverse bias breakdown could easily occur. To confirm this thought a single photocell of the same geometry as those that comprise the 920 cell array is reversed biased until current flowed. The photocell has a measured reverse bias breakdown voltage of around 8 V as shown in Figure 77.

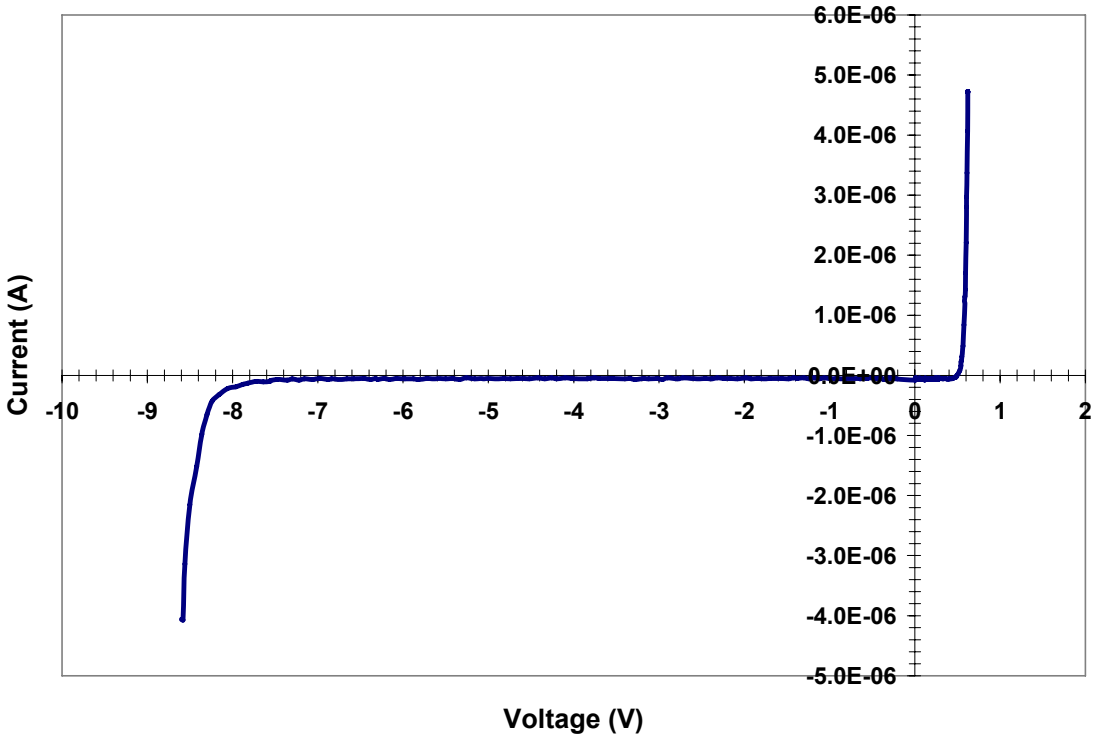

Figure 77. Reverse bias breakdown in a 270 μm x 60 μm photocell.

5.3 Engineering Example

To summarize the theory we present the following example. We wish to design an optical power transfer system using a 5 mm radius SCPA with a V_{OC} of 120 V. Si photocells are used and each cell generates 0.6 V and therefore the SCPA will consist of 200 photocells with each cell having an area of 0.654 μm^2. An 808 nm laser diode that is fiber coupled serves as the illumination source. The fiber has a core diameter of 100 μm and an NA of 0.22. It is assumed that the illumination profile radiated from the multi-mode fiber is uniform and that the least illuminated cell is illuminated at a level that is one standard deviation below the mean. Reverse bias breakdown is also assumed not to occur. Given these parameters what is the maximum illumination efficiency that can be obtained?

First let's determine the spacing between the SCPA and fiber such that the light diverges enough to cover the entire array. The beam radius, r_{beam}, increases as a function of distance, z, according to

$$r_{beam} = a + \tan\left(\sin^{-1}\left(NA\right)\right) z\,, \tag{143}$$

where a is the fiber radius. At $z = 22.1\,\text{mm}$ the beam has expanded to a radius of 5 mm. The mean speckle correlation area at this distance (Eq. (137)) is 0.041 μm^2. This gives a speckle/cell area ratio, A_D / A_C , of 15.95. Eq. (115) states,

$$M \approx \frac{A_D}{A_C} \quad \left(A_D >> A_C\right), \tag{144}$$

and using Eq. (128) results in an efficiency of

$$\eta_I = 1 - \frac{1}{\sqrt{2M}} = 82.3\%\,. \tag{145}$$

5.4 Summary

Covered in this Chapter were the effects of coherent multi-mode optical fiber illumination on the efficiency of an SCPA due to speckle. The efficiency was defined in terms of the ratio of the mean speckle correlation area and the area of the individual photocells within the array. The generalized van Cittert-Zernike theory was applied to the case of a multi-mode optical fiber and the result was used to calculate the mean speckle correlation area as a function of fiber diameter, wavelength, and propagation distance.

Photocell current is directly related to the incident power. This power is determined by the integral of the incident speckled intensity incident over the photocell area. An equation for the upper bound on the illumination efficiency for the SCPA was derived by applying the theory of unpolarized integrated speckle along with the generalized van Cittert-Zernike theory and considering the limiting case of the least illuminated photocell.

Experiments were performed that measured the mean speckle correlation area and the illumination efficiency. The speckle measurements were in good agreement with the theory while quantative differences in the measured illumination efficiencies were observed. Deviations from the theory in the observed efficiency measurements were attributed to the probability of a mean speckle correlation area being larger than a standard deviation below the mean. There was one test condition were the results deviated from the trend in the test data. For this condition the photocell geometry and illumination was such that it is highly probable that a photocell was entirely unilluminated therefore resulting in reverse bias voltage breakdown.

The results of the theory presented in this Chapter clearly lays out the design criteria that one must consider when designing an optical power transfer system and is concluded with an engineering example.

6 Beam Shaping Considerations

The efficiencies possible using a single-mode beam and multi-mode optical fiber illumination have been addressed up to this point. There are methods with which to

shape the illumination profile and increase the illumination efficiency. Although beam shaping is outside the scope of this thesis, the reader is given a starting point for general methods in which one can improve the illumination efficiency.

It is clear from the previous that it is generally required to shape the illumination beam irradiance to optimize the performance of an SCPA. A uniform irradiance profile is needed to obtain optimum performance from SCPAs in many applications. This is not a trivial thing to do since one aspect of the application of photovoltaic arrays is to conserve space, while some minimum space is required to shape the illumination. The techniques for shaping a laser beam can be divided into three broad classes: apertured beams, field mappers, and multi-aperture beam integrators or beam homogenizers [28]. These techniques are well treated in the literature [29] – [30]. In the case of apertured beams, a uniform irradiance is obtained by expanding the input beam to obtain an approximately uniform irradiance over an area and then using an aperture to eliminate the remaining part of the beam. This is generally not an efficient process. However, it is an important part of some shaping processes. Since the beam usually needs to be expanded before aperturing, some volume is required. One may think of the SCPA as the aperture.

Field mapping is a technique for mapping single mode laser beams into a desired irradiance pattern. In fact, both phase and amplitude can be controlled. In the case that a uniform irradiance is all that is required, the phase is a free parameter. Not needing to control the phase simplifies the problem.

Beam integrators are suited to the problem of shaping multimode beams. Although multimode beams may have a high degree of spatial coherence, their patterns may change from time to time in a somewhat random fashion, thus negating the application of field mapping. Further, since the input pattern is not predictable one can not use the input pattern as part of the design. Beam integration generally consists of a technique for breaking the input beam into multiple "beamlets" and combining the result to obtain an average. This is the origin of the term "beam integrator." Since beam integrators combine multiple beams the shaped pattern will be speckled. The amount of speckle will depend on the spatial coherence of the input beam. For these reasons, beam integrators are the choice for shaping the output of multimode fibers. The SCPA system design should consider the speckle pattern in the beam integrator output.

Another application might be an illumination scheme using laser diode arrays. Considerable attention has been given to the shaping of laser diode arrays [31-34]. Generally, some space is required to map a given beam into a desired shape. The space required can be estimated using a parameter β that can be derived by applying the uncertainty principle to the diffraction theory for the shaping problem [29]. This parameter of the shaping problem can be expressed in the form

$$\beta = C\frac{r_0 y_0}{\lambda z}, \tag{15}$$

where r_0 is the input beam half-width, y_0 is the out put beam half-width, z is the distance from the shaping optics, and C is constant that depends on the problem. We can take C to be approximately 5. β should be greater than 8 for field mappers and 40 for

beam integrators. For fixed λ we want to make r_0 and y_0 large, and z small to make β large. Assuming that the r_0 is determined by the fiber core diameter and $z \geq 2y_0$ one can easily see that shaping can be achieved in a relatively small volume using micro-optics technology for field mappers. Beam integrators would require more volume. This is due to the fact that the lenslet size is the input beam size in (15), and we want to have a relatively large number of lenslets within input beam area. Thus, it may be required to expand the input beam.

Another approach for optical fiber beam delivery would be to image the output fiber face onto the array. The magnification generally would require a large object to image distance ratio, making for a relatively long optical path. Again, one would also have to address the speckle problem for the imaging case.

7 Conclusion

This thesis presented a method for developing PSpice models and developed system design criteria for achieving optimum SCPA performance under Gaussian or multi-mode fiber optic illumination. The topics presented are illustrated by a series of experiments.

PSpice modeling included simulating the SCPA as a lumped element as well as an array of series connected photocells. The lumped element SCPA model is created by using an ABM and is most appropriate when simulating the performance of a circuit that is powered by an SCPA. Using an ABM to model an SCPA also decreases simulation run

times and improves convergence issues. The models presented exhibited a relatively low error of only a few percent.

PSpice simulation of SCPA performance is also possible by individually modeling each of the series connected photocells and is useful for investigating the effects of non-uniform illumination. These models also had an RMS error of only a few percent.

When SCPAs are illuminated with a Gaussian beam it is shown that the best case illumination efficiency is 36.8 %. The efficiency is dependent on the ratio of the Gaussian beam radius and the SCPA radius. A beam radius that is larger than the SCPA means that light is incident outside of the device and results in loss. Also, if the beam radius is too small the photocells along the perimeter are illuminated at a lower level than the rest of the array. This results in a loss of efficiency due to the current limiting caused by the under illuminated photocells. An equation was derived that shows the optimum efficiency is achieved with a ratio of $w_{opt} = \sqrt{2}r$ (Eq. (54)). An experiment was performed to illustrate this theory and the test results closely matched the theory. It is also shown that the responsivity of an SCPA can be calculated by using Gaussian illumination.

For the case of illumination with a multi-mode optical fiber, the illumination efficiency is determined by the mean speckle correlation area. The mean speckle correlation area was shown to be dependent on the fiber diameter, wavelength and propagation distance. Dependence on these parameters was quantified by applying the generalized van Cittert-

Zernike theory to the case of a multi-mode optical fiber. An equation for the upper bound on the illumination efficiency for the SCPA was derived by applying the theory of unpolarized integrated speckle and defined the performance in terms of the ratio of the mean speckle correlation area and area of the individual photocells within the array. A set of experiments was performed to illustrate the theory and were in good agreement with the theory.

In conclusion, this thesis provides for an excellent guide outlining methods for modeling SCPAs and designing an optical power transfer system using Gaussian or multi-mode optical fiber illumination.

References

1. J. W. Shelton and F. M. Dickey, "The effects of optical fiber illumination on the performance of series connected photovoltaic arrays for power conversion," in *Optical Technologies for Arming, Safing, Fuzing, and Firing II*, edited by William J. Thomes, Jr., Fred M. Dickey, Proceedings of SPIE Vol. 6287 (SPIE, Bellingham, WA, 2006) 62870E.

2. J. W. Shelton, F. Dickey, W. Thomes "Optically powered firing set using miniature photovoltaic arrays," *in Optical Technologies for Arming, Safing, Fuzing, and Firing III*, edited by William J. Thomes, Jr., Fred M. Dickey, Proceedings of SPIE Vol. 6662 (SPIE, Bellingham, WA, 2006) 6662-5.

3. R. K Patel, R. D. Nasby, D. J. Stein, A. H. Hsia, and R. S. Bennet, "High voltage series connected Si photovoltaic cells," in *Optical Technologies for Arming, Safing, Fuzing and Firing*, edited by William J. Thomes, Jr., Fred M. Dickey, Proc. SPIE Vol. 5871, 58710F (2005).

4. J-G. Werthen, S. Widjaja, T.-C. Wu, and J. Liu, "Power over fiber: a review of replacing copper by fiber in critical applications," in *Optical Technologies for Arming, Safing, Fuzing and Firing*, edited by William J. Thomes, Jr., Fred M. Dickey, Proc. SPIE Vol. 5871, 58710C (2005).

5. B. H. Rose, “Monolithic series connected GaAs photovoltaic converters for optoelectronic component applications,” Sandia Report: SAND92-1534, Sandia National Laboratories, Albuquerque, NM, 1992.

6. J. Ohsawa, K. Shono, and Y. Hiei “High-voltage micro solar cell arrays of GaAs with output voltage up to 100 V,” 2002 IEEE/LEOS International Conference on Optical MEMS, Lugana, Switzerland, pp. 103-4, 2002.

7. D. J. Stein, R. Nasby, R. K. Patel, A. Hsia, and R. Bennett, “High voltage with Si series photovoltaics,” in *Optical Technologies for Arming, Safing, Fuzing, and Firing II*, edited by William J. Thomes, Jr., Fred M. Dickey, Proceedings of SPIE Vol. 6287(SPIE, Bellingham, WA,2006) 62870D.

8. H. Rauschenbach, *Solar Cell Array Design Handbook*, Van Nostrand Reinhold Company, New York, 1980.

9. D. A. Neamen, *Semiconductor Physics and Devices*; 3rd edition, McGraw Hill, New York, NY, 2003.

10. C. Hu and R. White, *Solar Cells: From Basics to Advanced Systems,* McGraw Hill, New York, NY 1983.

11. E. Dereniak, D. Crowe, *Optical Radiation Detectors,* Ch. 3, Photovoltaic Detection Theory, John Wiley and Sons, New York, 1984.

12. Newport Corporation, Gaussian Beam Optics Tutorial, http://www.newport.com/servicesupport/Tutorials/default.aspx?id=112.

13. J. Goodman, *Speckle Phenomena in Optics: Theory and Applications*, Roberts & Company, Englewood, Colorado, 2006.

14. J. Goodman, *Statistical Properties of Laser Patterns*, Ch. 2. Laser speckle and related phenomena, Editor J. Dainty, Springer-Verlag, 1984.

15. J. Goodman, *Statistical Optics*, John Wiley & Sons, Inc., New York, New York, 1985.

16. G. Agrawal, *Fiber-Optic Communication Systems*, John Wiley & Sons, Inc., New York, New York, 2002.

17. http://www.tpub.com/neets/tm/106-10.htm.

18. B. Daino, S. Piazzola, and A. Sagnotti, "Spatial coherence and index-profiling in optical fibers," Optica Acta, vol. 26, no. 7, pp. 923-928, 1979.

19. C. Pask, A. Snyder, “The van Cittert-Zernike theorem for optical fibres,” Optics Communications, vol. 9, no. 1, 1973.

20. B. Daino, G. De Marchis, and S. Piazzolla, “Speckle and modal noise in optical fibers: Theory and experiment,” Optica Acta, vol. 27, no. 8 pp. 1151-1159 1980.

21. B. Daino, G. De Marchis, and S Piazzolla, “Analysis and measurement of modal noise in an optical fibre,” Electronics Letters, vol. 15, no. 23 pp. 775-756, 1979.

22. E. G. Rawson, J. W. Goodman, and R. E. Norton, “Analysis and measurement of the modal-noise probability distribution for a step-index optical fiber,” Optics Letters, vol. 5, no. 8, pp. 357-358, 1980.

23. J. W. Goodman, and E. G. Rawson, “Statistics of modal noise in fibers: a case of constrained speckle,” Optics Letters, vol. 8, no. 7, pp. 325-326, 1981.

24. B. Daino, G. De Marchis, and S Piazzolla, “Modal noise in optical fibers in the presence of model correlation,” Optics Communications, vol. 38, no. 5-6, pp. 340-344, 1981.

25. R. J. Bartula, and S. T. Sanders, “Estimation of signal noise induced by multimode fibers,” Optical Engineering, vol. 47, no. 3, 035002, 2008.

26. J. Saleh and M. Teich, *Fundamentals of Photonics*, John Wiley & Sons, Inc., New York, New York, 1991.

27. S. Solimeno, B. Crosignani, and P. DiPorto, *Guiding, Diffraction, and Confinement of Optical Radiation*, Academic Press, Inc., New York, New York, 1986.

28. F. M. Dickey, "Laser Beam Shaping," OPN Optics and Photonics News, 14(4), 2003.

29. F. M. Dickey and S. C. Holswade, *Laser Beam Shaping: Theory and Techniques*, CRC Press, Taylor and Francis Group, Boca Raton, New York, 2000.

30. F. M. Dickey, S. C. Holswade, and D. L. Shealy, *Laser Beam Shaping Applications*, CRC Press, Taylor and Francis Group, Boca Raton, 2005.

31. F. M. Dickey and D. L. Shealy, Editors, Laser Beam Shaping V, Proc. SPIE 5525, 2004.

32. F. M. Dickey and D. L. Shealy, Editors, Laser Beam Shaping VI, Proc. SPIE 5876, 2005.

33. D.M. Brown, “High-power laser diode beam combiner,” Optical Engineering, 42(11), 3086-3087, 2003.

34. D.M. Brown, “Beam integrators for high-power stripe laser diodes,” Proc. SPIE 5175, 121-129, 2003.